Teleseismic Body Wave Attenuation and Diffraction

by

Yong Keun Hwang

A dissertation submitted in partial fulfillment
of the requirements for the degree of
Doctor of Philosophy
(Geology)
in The University of Michigan
2011

Doctoral Committee:

Associate Professor Jeroen Ritsema, Chair
Professor Roman D. Hryciw, Cognate
Professor Larry J. Ruff
Professor Peter E. van Keken
Professor Charles J. Ammon, Pennsylvania State University

To My Mother and Father

ACKNOWLEDGEMENTS

There are many people and associations without whose support this thesis would not have been accomplished.

I would like to express my appreciation to my supervisor Dr. Jeroen Ritsema for providing me with an opportunity to work on excellent projects and for his through concern and support throughout my Ph.D. study.

I would like to thank Dr. Peter E. van Keken, Dr. Larry J. Ruff, Dr. Roman D. Hryciw, and Dr. Charles J. Ammon for their critical reviews on this thesis and for providing their expertises.

I thank Dr. Saskia Goes for her considerable contribution for my published and submitted treatises, Dr. Colleen Dalton for providing her Q model and for giving advice on model interpretation, Dr. Jonathan Lees for providing the MTM (Multi-Taper Spectral Analysis Methods) software, Dr. Michael Thorne for providing the code SHaxi for wave simulation, and Dr. James O'Connolly for making the code PerPleX for velocity conversions available. I thank the Data Management Centers of IRIS for providing data and NSF (National Science Foundation) for funding grants. Figures are produced by GMT (Generic Mapping Tools) software. Also, I would like to thank all members of the University of Michigan Geophysics Laboratory and all of the students, postdocs, staffs, and faculty members in the Department of Geological Sciences, University of Michigan who inspired and helped me.

Finally, I express my special thanks to my mother and siblings who have always been supportive throughout my Ph.D. study.

TABLE OF CONTENTS

LIST OF FIGURES

Figure

LIST OF TABLES

Table

LIST OF APPENDICES

Appendix

GLOSSARY

$PhysicalMeasure$ Description [Dimension]

Q quality factor [-]

Q_P quality factor for P-wave [-]

Q_μ quality factor for shear [-]

Q_κ quality factor for bulk [-]

Q^{-1} absorption [-]

Q_P^{-1} absorption in P-wave [-]

Q_μ^{-1} absorption in shear [-]

Q_κ^{-1} absorption in bulk [-]

t^* attenuation parameter [Time]

t_P^* P-wave attenuation parameter [Time]

t_S^* S-wave attenuation parameter [Time]

Δt^* differential attenuation [Time]

V_P P-wave velocity [Distance/Time]

V_S S-wave velocity [Distance/Time]

ABSTRACT

Teleseismic Body Wave Attenuation and Diffraction

by

Yong Keun Hwang

Chair: Jeroen Ritsema

Using available digital seismic stations deployed since the 1980's, the largest data set based on broadband waveforms among studies on body-wave attenuation (t^*) and quality factor (Q) are used in this thesis. The use of nearly 300,000 measurements of body-wave spectral ratio from globally distributed stations renders better constraints of t^* and Q variations with higher spatial and depth resolutions in the mantle than have been previously available. The maps of body-wave t^* correlate well with the variations of t^* computed from the most recent surface-wave Q model QRFSI12 indicating that body-wave and surface-wave t^* reflect the same intrinsic attenuation even though these waves sample the upper mantle entirely differently. The high correlation between body-wave t^* maps and the t^* inferred from a thermal interpretation of shear-wave velocity tomography S20RTS suggests that temperature controls both variations in attenuation and velocity in the upper mantle.

The distance variations of P- and S-wave t^* (t^*_P and t^*_S) are inverted for a radial profile of the quality factor Q_μ in the lower mantle. On average, t^*_P and t^*_S increase by about 0.2 s and 0.7 s, respectively, between epicentral distances of 30° and 97°. The

body-wave spectra are explained best if Q_μ increases in the lower mantle with the rate of 0.1/km. The relatively strong increase of t_S^* compare to t_P^* ($t_S^* \approx 4\,t_P^*$) suggests that intrinsic attenuation is the cause of the overall trend in our data. The ratio of P- and S-wave quality factor determined in this thesis ($Q_P/Q_\mu = 2.27$) confirms that intrinsic attenuation occurs mostly in shear and that bulk attenuation is negligible in the mantle.

Finally, the delay of seismic waves which traversed numerical mantle plumes are calculated in this thesis for the first time. High-resolution numerical simulations of mantle plume are used to investigate the effects of numerical plumes on waveforms. The measurements of wave front delay demonstrate that the delay of shear-waves by plume tails at depths larger than 1000 km are immeasurably small (< 0.2 s) at seismic periods commonly used in waveform analysis.

CHAPTER I

Introduction

The seismic energy released from earthquakes are redistributed within the Earth by geometric spreading and wave reflection, refraction, diffraction, and scattering. In these elastic processes, the total amount of seismic energy is conserved. However, seismic waves are attenuated by losing energy in the form of heat and permanent strain. The efficiency of seismic energy propagation through a medium is commonly expressed by the quality factor Q. Its inverse, the absorption (Q^{-1}), is defined as

$$Q^{-1} = \Delta E / 2\pi E_{max}, \tag{1.1}$$

where ΔE is the energy lost per cycle and E_{max} is the maximum elastic energy contained in a cycle.

Models of the elastic velocity structure of the mantle have advanced our knowledge of mantle dynamics as small as a few hundred kilometers in scale (e.g., *Romanowicz*, 2008). However, velocity models by themselves are not sufficient to obtain complete descriptions of the physical state of Earth's interior. When combined with elastic velocity structures, anelastic attenuation models can provide important complementary information on the physical state of Earth's interior because the dependencies of anelastic attenuation on temperature, water content, chemical composition, and partial melting are different from those of elastic velocity. Anelasticity has a much

stronger sensitivity to temperature and water content than elastic velocities, a lower sensitivity to composition, and a different sensitivity to melt (e.g., *Anderson*, 1967; *Sato et al.*, 1989; *Karato and Jung*, 1998; *Hammond and Humphreys*, 2000a,b; *Jackson et al.*, 2002; *Faul et al.*, 2004; *Faul and Jackson*, 2005; *Shito et al.*, 2006). Studies have demonstrated that velocity variations in seismic tomography for the uppermost mantle (<200–300 km) are primarily due to temperature variations (*Sobolev et al.*, 1996; *Goes et al.*, 2000; *Goes and van der Lee*, 2002; *Lee*, 2003; *Godey et al.*, 2004; *Shapiro and Ritzwoller*, 2004; *Faul and Jackson*, 2005; *Deen et al.*, 2006; *Schutt and Lesher*, 2006) because of the high temperature sensitivity to anelastic effects in this depth range (*Sato et al.*, 1989; *Karato*, 1993; *Goes et al.*, 2000; *Jackson et al.*, 2002; *Faul and Jackson*, 2005). Variations in major element chemistry have a non-negligible contribution on velocity anomalies only in the coldest regions of the uppermost mantle, which can be resolved in combination with density-sensitive data (*Perry et al.*, 2003; *Godey et al.*, 2004; *Deen et al.*, 2006). However, the interpretation of tomographic models is meaningful only when constraints on attenuation with comparable spatial resolution are available. Using the largest data among attenuation studies using body-wave spectra, this thesis aims to obtain attenuation structures with higher resolutions than have previously been obtained.

Attenuation structures have not been investigated as vigorously as velocity structures and global attenuation models are still designed to constrain long wavelength variations because the effects of intrinsic attenuation on wave amplitudes cannot be easily distinguished from the effects of wave scattering, focusing, and crustal amplification even in a perfectly elastic but heterogeneous Earth. Early studies have examined the amplitude variations of seismic body-waves in the United States from teleseismic earthquakes (*Cleary*, 1967; *Evernden and Clark*, 1970; *Booth et al.*, 1974) and nuclear explosions (*Butler and Ruff*, 1980). However, the number of sources and stations are limited to a few or a few tens and the frequency band is limited

to long period (> 0.25 s). More recent studies have mapped the global and the regional variations of seismic wave attenuation in the upper mantle using surface-waves (e.g., *Romanowicz*, 1995; *Billien et al.*, 2000; *Romanowicz and Gung*, 2002; *Selby and Woodhouse*, 2002; *Gung and Romanowicz*, 2004; *Dalton and Ekström*, 2006; *Dalton et al.*, 2008), and body-waves (e.g., *Sheehan and Solomon*, 1992; *Bhattacharyya et al.*, 1996; *Roth et al.*, 1999, 2000; *Reid et al.*, 2001; *Warren and Shearer*, 2002; *Lawrence et al.*, 2006; *Lawrence and Wysession*, 2006a,b), and *Lg* coda (*Baqer and Mitchell*, 1998; *Mitchell and Cong*, 1998). These studies indicate that the upper 200–300 km of the mantle beneath oceans and tectonically active regions is generally more attenuating than the mantle beneath stable, continental shields. Although these studies share similar large-scale features that correlate with the seismic velocity structures, it is well appreciated that global attenuation models are strongly damped and that they may underestimate the peak-to-peak variations in attenuation within various regions. It is therefore difficult to determine whether the elastic and anelastic seismic structures in the shallow mantle have a common physical origin.

Depth-dependent whole mantle shear-wave Q (Q_μ) profiles also have been constrained using normal-modes (*Dziewonski and Anderson*, 1981; *Widmer et al.*, 1991; *Durek and Ekström*, 1996; *Roult and Clévédé*, 2000; *Resovsky et al.*, 2005) and ScS/S waveforms (*Lawrence and Wysession*, 2006a). These profiles have a common low Q_μ layer in the uppermost mantle (80–200 km depth), intermediate Q_μ values in the transition zone (200–650 km), and the highest Q_μ values in the lower mantle. However, absolute values of Q_μ and the depth dependence of Q_μ in the lower mantle differ in these profiles. Some studies have suggested Q structures in the lower mantle are constant (*Dziewonski and Anderson*, 1981; *Durek and Ekström*, 1996; *Oki and Shearer*, 2008) with little depth resolution. Other studies have suggested slightly increasing (*Lawrence and Wysession*, 2006a) or slightly decreasing (*Okal and Jo*, 1990; *Widmer et al.*, 1991) Q structures in the lower mantle. *Resovsky et al.* (2005) constrain Q_μ to

decrease in the lowermost 1000 km of the mantle while Q_μ increases in model QLM9 (*Lawrence and Wysession*, 2006a) in the same depth range. Variable approaches, data sets, and measurement uncertainties are responsible for these differences and underscore that the basic radial structure of Q is still poorly constrained.

The attenuation of a seismic body-wave is the accumulative effect of Q^{-1} on the wave since the seismic energy is released from a source until it is recorded in a station. This seismic attenuation is defined by the attenuation parameter t^* that represents the total body-wave traveltime divided by Q along the travel path L (e.g., *Stein and Wysession*, 2003):

$$t^* = \int_L \frac{\mathrm{d}t}{Q}. \tag{1.2}$$

Typical values of t^* for teleseismic (epicentral distance between 30° and 90°) P- and S-waves (t_P^* and t_S^*) are 1 s and 4 s, respectively (*Cormier*, 1982). Although a seismic wave travels through the deeper part of the Earth and t^* is more affected by the Q structure of the lower mantle with increasing epicentral distance, the wave stays in the upper mantle for a shorter period of time because it travels this part of the mantle with a steeper angle. However, it has been suggested that the distance effect on attenuation is little at teleseismic distances (*Carpenter et al.*, 1967; *Booth et al.*, 1974) which suggests that body waves are attenuated primarily in the upper mantle.

In this thesis, t^* values for densely distributed stations are estimated (Chapters II and III) and the depth variation in Q is determined (Chapter IV) using ratios of broadband teleseismic body-wave spectra of deep earthquakes. As the t^* measurements encompass multiple effects such as intrinsic attenuation, crustal amplification, focusing and defocusing, and local scattering in the upper mantle under stations, the t^* inversion relies on a large and redundant set of measurements over a wide range of azimuths, thus as many as 300,000 body-wave spectral ratios are used in this thesis. By means of this large data set, t^* maps with higher spatial resolutions in the upper-

most mantle and Q profiles with higher depth resolutions in the lower mantle can be obtained.

The availability of the spectral ratio method and the use of large global data set to constrain the spatial t^* variations in the upper mantle and the depth-dependent Q variations in the lower mantle is confirmed to be valid in various ways. The global tectonic setting is the surface expression of the thermal structure which is highly sensitive to intrinsic attenuation in the uppermost mantle. Thus, the compatibility between t^* maps derived from body-wave spectra with global tectonics and heat flow will illustrate that the variations in body-wave t^* are due to the intrinsic attenuation in the upper mantle.

The review by *Cormier* (1982) and the prediction from 1D Q profiles (e.g., *Dziewonski and Anderson*, 1981; *Durek and Ekström*, 1996) suggest that the t_S^*/t_P^* ratio is between 3.5 and 4.0. If the information on attenuation in the upper mantle is properly retrieved from the body-wave spectra, it is expected that the spatial variation and the increase with epicentral distance in t_S^* is stronger than those in t_P^* by the factor between 3.5 and 4.0.

The t_S^* map derived from joint inversion of P- and S-wave spectra is compared with an attenuation map inferred from a surface-wave Q tomography (t_Q^*) in order to determine the compatibility of body wave and surface wave attenuation constraints. As the wavelengths and propagation directions of body-waves and surface-waves are entirely different, the consistency between t_S^* and t_Q^* will suggest that patterns in these maps are robust features of the attenuation structure in the upper mantle. t_S^* map is also compared with an attenuation map inferred from a thermal interpretation of shear-velocity tomography in the upper mantle (t_T^*). This comparison will test whether the thermal structure is the same major control for both t_S^* and velocity variations in the uppermost mantle, which has been suggested in previous studies (*Sobolev et al.*, 1996; *Goes et al.*, 2000; *Goes and van der Lee*, 2002; *Lee*, 2003;

Artemieva et al., 2004; *Godey et al.*, 2004; *Shapiro and Ritzwoller*, 2004; *Faul and Jackson*, 2005; *Deen et al.*, 2006; *Schutt and Lesher*, 2006; *Dalton et al.*, 2009; *Dalton and Faul*, 2010).

In this thesis, a global mantle Q profile is also determined from the epicentral distance variation of t_P^* and t_S^*. The ratio between Q for P-wave (Q_P^{-1}) and for S-wave (Q_μ^{-1}) provides important information on Q for bulk attenuation (Q_κ^{-1}). The relation among Q_P^{-1}, Q_μ^{-1}, and Q_κ^{-1} is

$$Q_P^{-1} = LQ_\mu^{-1} + (1 - L)Q_\kappa^{-1}, \tag{1.3}$$

where $L = \frac{4}{3}(V_S/V_P)^2$ and V_S and V_P are the S- and P-wave velocities (e.g., *Anderson and Given*, 1982). Theoretically, if it is assumed that $V_P/V_S = \sqrt{3}$, then a Q_P/Q_S ratio of 1.75 is expected when bulk attenuation is about 20 % of shear attenuation (*Roth et al.*, 1999), and a ratio of 2.25 is expected when bulk attenuation is negligible (*Anderson and Given*, 1982). The investigation of the Q_P/Q_S ratio derived from a large data set of body-wave spectra can determine the relative importance of Q_κ^{-1} in the lower mantle.

The original study of distance variation in attenuation and Q by *Teng* (1968) and subsequent studies of spectral ratios (e.g., *Solomon and Toksöz*, 1970; *Der and McElfresh*, 1977; *Der et al.*, 1982) and amplitude decay (e.g., *Booth et al.*, 1974; *Butler and Ruff*, 1980) were mostly applied to band-limited, analog waveform data from the United States. In this thesis, a nearly two-decade long collection of digital waveforms from broadband seismic stations in regional and global networks is used to determine the depth variation in Q. This thesis will present a frequency-independent Q_μ structure in the lower mantle using body-wave spectra up to 0.8 Hz. It was suggested in previous studies that Q is nearly independent of frequency (ω) (*Kanamori and Anderson*, 1977) or slightly frequency-dependent by $Q(\omega) = Q_0\ \omega^\alpha$, where the

frequency-dependent parameter α is between 0.1 and 0.3 (e.g. *Minster and Anderson*, 1981; *Smith and Dahlen*, 1981; *Anderson and Given*, 1982; *Shito et al.*, 2004; *Lekić et al.*, 2009). In this thesis, the difference in absolute Q_μ values in the lower mantle between the model derived from body-wave spectra (up to 0.8 Hz) and PREM model (*Dziewonski and Anderson*, 1981) from normal-mode (at about 1 Hz) will be investigated and the frequency-dependence (α) of $Q(\omega)$ will be determined for body-waves at the frequency band up to 0.8 Hz.

Chapters II – V are peer-reviewed articles reproduced without modifications and have been included in this thesis in their original published (Chapters II – IV) or submitted (ChapterV) forms.

CHAPTER II

Spatial variations of P wave attenuation in the mantle beneath North America

2.1 Abstract

We estimate the spatial variation of the seismic parameter t^* using teleseismic (epicentral distance = 30°–85°) P wave spectra of about 200 deep (focal depths > 200 km) earthquakes recorded by 378 broadband seismometers in the United States and Canada. Relative P wave spectral ratios up to 1 Hz for about 63,000 station pairs with high signal-to-noise ratio and impulsive P waveforms are inverted for t_P^* by least squares inversion. The continental-scale t_P^* pattern correlates to the age of geological terrains and the seismic, heat flow, gravity, and magnetic variations across North America. Predominantly low values of t_P^* are obtained in stable central North America (SNA), and high t_P^* values are obtained for stations in the tectonically active western part of the continent (TNA). This variation is similar to that observed previously in short-period amplitude anomalies, spectral ratio variations, and ScS reverberations. On average, we resolve a contrast in t_P^* between SNA and TNA of about 0.2 s. We resolve regional variations in t_P^*, which correlate with tectonics. Relatively low t_P^* is

This chapter has originally been published in Hwang, Y. K., J. Ritsema, and S. Goes (2009), Spatial variations of P wave attenuation in the mantle beneath North America, *J. Geophys. Res., 114* (B06312), doi:10.1029/2008JB006091.

associated with currently active subduction below Alaska. Relatively high t_P^* is found in SNA below the Appalachians and the Gulf Coast. The consistency between t_P^* and tectonics suggests that the observed variations in t_P^* are, on the scale of around 200–500 km, predominantly due to intrinsic attenuation. The similar patterns in t_P^* and predicted values for a recent global attenuation model confirm this further. The compatibility with the t_P^* computed for attenuation estimated via a thermal interpretation of shear wave velocity anomalies illustrates that variations in seismic velocity are predominantly due to physical effects with a strong attenuation signature, most likely temperature or a combination of temperature and water content.

2.2 Introduction

Models of seismic attenuation provide important constraints on the physical state of Earth's interior. Seismic wave attenuation and velocity dispersion (*Kanamori and Anderson*, 1977) are affected by temperature, by volatiles, and, depending on the dominant relaxation mechanism, by the presence of melt (*Sato et al.*, 1989; *Hammond and Humphreys*, 2000b; *Faul and Jackson*, 2005). Moreover, anelasticity provides one of the few available measures of rheology at lithosphere and mantle conditions, albeit on seismic timescales (*Karato and Spetzler*, 1990; *Hammond and Humphreys*, 2000b; *Faul and Jackson*, 2005).

Attenuation constraints are key in the interpretation of models of seismic velocity (i.e., seismic tomography) (*Sobolev et al.*, 1996; *Goes et al.*, 2000; *Goes and van der Lee*, 2002; *Lee*, 2003; *Godey et al.*, 2004; *Shapiro and Ritzwoller*, 2004; *Faul and Jackson*, 2005; *Deen et al.*, 2006; *Schutt and Lesher*, 2006). These studies demonstrate that velocity variations in the uppermost mantle (<200–300 km) are primarily due to temperature variations because of the high temperature sensitivity to anelastic effects in this depth range (*Sato et al.*, 1989; *Karato*, 1993; *Goes et al.*, 2000; *Jackson et al.*, 2002; *Faul and Jackson*, 2005). Variations in major element chemistry have a

non-negligible contribution on velocity anomalies only in the coldest regions of the uppermost mantle, which can be resolved in combination with density-sensitive data (*Perry et al.*, 2003; *Godey et al.*, 2004; *Deen et al.*, 2006). However, the interpretation of tomographic models is meaningful only when constraints on attenuation with comparable spatial resolution are available.

On a global scale, tomographic images reveal seismic velocity structures that are only a few hundred kilometers in size (*Romanowicz*, 2008). Global attenuation models are still designed to constrain long wavelength variations because the effects of intrinsic attenuation on wave amplitudes cannot be easily distinguished from the effects of wave scattering, focusing, and crustal amplification in a perfectly elastic but heterogeneous Earth. Global attenuation models based on surface waves (*Romanowicz*, 1995; *Billien et al.*, 2000; *Romanowicz and Gung*, 2002; *Selby and Woodhouse*, 2002; *Dalton and Ekström*, 2006), body waves (*Bhattacharyya et al.*, 1996; *Reid et al.*, 2001; *Warren and Shearer*, 2002; *Lawrence and Wysession*, 2006a), and *Lg* coda (*Mitchell and Cong*, 1998) share similar large-scale features that correlate with the seismic velocity structures. However, it is well appreciated that, because of the strong influence of focusing effects, global attenuation models are strongly damped and that they may underestimate the peak-to-peak variation in attenuation within various regions. It is therefore difficult to determine whether the elastic and anelastic seismic structures in the shallow mantle have a common physical origin.

In this study we analyze attenuation in the upper mantle using broadband teleseismic (epicentral distance = 30°–85° P wave spectra of deep earthquakes. We focus on the North American continent. Here resolution is relatively high because of the dense station coverage offered by the various regional seismic networks. Moreover, we expect large variations in attenuation in North America due to its diverse tectonic terrains, facilitating a comparison of models obtained from a variety of data types.

We compare our results to the most recent global surface wave attenuation model

(*Dalton et al.*, 2008) and an attenuation model inferred from a thermal conversion of a regional shear velocity model (*Goes and van der Lee*, 2002). This allows us to place our results in a global context, to determine the compatibility of the body wave and surface wave attenuation constraints, and to evaluate whether a thermal interpretation of shear velocity variation and attenuation is justified.

2.3 Seismic Wave Attenuation in North America

The Rocky Mountain Front divides North America into tectonic western North America (TNA) and stable eastern North America (SNA). TNA is associated with current extension in the Basin and Range, subduction under Oregon and Washington continued to transform motion in California, and volcanism in Yellowstone and western Rocky Mountain front (*Burchfiel et al.*, 1992; *Humphreys and Coblentz*, 2007). In contrast, the most recent tectonic event in SNA is related to the Appalachian orogeny (330–265 Ma) (*Dallmeyer et al.*, 1986; *Secor Jr. et al.*, 1986).

Geophysical studies of the upper mantle and the lithosphere indicate that a structural divide between TNA and SNA persists in the mantle. High surface heat flow, low-amplitude magnetic anomalies, and a negative long wavelength Bouguer gravity in TNA indicate that the mantle below TNA is hot while low surface heat flow and short wavelength magnetic and gravity anomalies indicate a cool lithosphere mantle below SNA (*Morgan and Gosnold*, 1989). Studies of body wave traveltime (*Grand and Helmberger*, 1984; *Melbourne and Helmberger*, 1998) and surface wave dispersion (*van der Lee and Nolet*, 1997; *Marone and Romanowicz*, 2007) show that the shear velocity in the upper mantle beneath SNA and TNA differs by as much as 15–20%.

A large number of studies have provided constraints on the attenuation structure in North America, including analyses of short-period amplitude anomalies (*Cleary*, 1967; *Booth et al.*, 1974; *Butler and Ruff*, 1980; *Der et al.*, 1982; *Butler*, 1984), spectral ratio variations (*Solomon and Toksöz*, 1970; *Der and McElfresh*, 1976, 1977; *Der*

et al., 1982), *Lg* coda waves (*Baqer and Mitchell*, 1998), and *ScS* multiples (*Lay and Wallace*, 1988). The studies show a common first-order pattern of a highly attenuating TNA and low-attenuation SNA. In addition, the regional studies indicate that smaller-scale (<1000 km) variations of attenuation can be as large as the continental-scale contrast between TNA and SNA. *Lay and Wallace* (1988), for example, suggest that shear wave attenuation in the upper mantle beneath the Basin and Range, a region with extremely high heat flow, is as strong as attenuation beneath active mid-ocean ridge spreading centers and that attenuation beneath the Pacific Northwest is comparable to attenuation within western Pacific subduction zones.

2.4 P Wave Spectral Analysis

In addition to the geometric spreading of wave fronts, seismic waves are attenuated by anelastic energy dissipation and scattering. The efficiency of wave propagation is commonly expressed by the quality factor Q. Its inverse, Q^{-1}, quantifies wave attenuation. Q^{-1} is defined as

$$Q^{-1} = \Delta E / 2\pi E_{max}, \tag{2.1}$$

where ΔE is the energy lost per cycle and E_{max} is the maximum elastic energy contained in a cycle.

The attenuation of teleseismic body waves is defined by the attenuation parameter t^*. The t^* parameter is a station-specific observable that represents the total body wave traveltime divided by Q along the ray path (*Stein and Wysession*, 2003):

$$t^* = \int_{ray} \frac{1}{V(r)Q(r)} \mathrm{d}s. \tag{2.2}$$

Typically, $t^*_P = 1$ s for teleseismic P waves and $t^*_P = 4$ s for teleseismic S waves

(*Cormier*, 1982). These values vary little with epicentral distance (*Booth et al.*, 1974) suggesting that body waves are attenuated primarily in the upper mantle. This observation is consistent with one-dimensional profiles derived from long-period surface waves and normal modes (*Dziewonski and Anderson*, 1981; *Durek and Ekström*, 1996) which show that Q values in the upper mantle are an order of magnitude lower than in the lower mantle.

In this study, we measure t_P^* from teleseismic P wave spectra. t_P^* encompasses multiple effects: intrinsic attenuation, crustal amplification, focusing and defocusing, and local scattering in the upper mantle under the receiver. Probably, each of these factors is equally important given the large scatter seen in measurements of t_P^*. To isolate the contribution of intrinsic attenuation to t_P^*, we rely on a large and redundant set of P wave spectra for earthquake/receiver combinations over a wide range of azimuths.

2.4.1 Teleseismic P Wave Spectra

We follow the classical approach developed by *Teng* (1968) and *Solomon and Toksöz* (1970). We write the spectrum $O(f)$ of a teleseismic seismogram as

$$O(f) = S(f)\exp(-\pi f t_P^*), \tag{2.3}$$

where $S(f)$ is the earthquake source spectrum and $\exp(-\pi f t_P^*)$ is the attenuation function. The logarithm of the ratio R_{ij} between the spectrum O_i and O_j at stations i and j is expected to change linearly with frequency f for the same earthquake:

$$\ln R_{ij}(f) = -\pi f \Delta t_{P_{ij}}^*, \tag{2.4}$$

Δt_P^* reflect differences in P wave attenuation in the upper mantle beneath regional network stations. We expect the influence of the lower mantle on Δt_P^* to be small

because attenuation in the lower mantle is relatively weak and P waves have similar lower mantle propagation paths for nearby stations (Figure 2.1). One of the benefits of using the spectral ratio over using the amplitude ratio to infer the variation in t_P^* is that the shapes of spectra are not as sensitive to other elastic effects such as crustal amplification, azimuthal variation, focusing, and local scattering near the source as they are to t_P^* while the amplitudes of body waves are severely affected by local focusing (*Der et al.*, 1982).

We restrict our analysis to teleseismic P wave recordings of deep (focal depth $>$ 200 km) earthquakes. P signals for deep earthquakes have relatively short durations without significant directivity (*Houston and Vidale*, 1994). Moreover, they are not complicated by surface reflections (i.e., pP and sP) nor attenuated by the uppermost mantle in the source region. For epicentral distances larger than 30° and smaller than 85°, P waves turn below the 660 km discontinuity and above the heterogeneous D'' region, where vertical velocity gradients are well understood. However, since teleseismic P waves propagate steeply through the upper mantle, Δt_P^* does not constrain depth variation of attenuation.

We select our recordings from 378 stations (Figure 2.2). These include Global Seismic Network and GEOSCOPE stations in the U.S. and Canada and regional network stations from the Canadian National Seismic Network (CNSN), the United States National Seismic Network (USNSN), TriNet (*Kanamori et al.*, 1997), the Berkeley Digital Seismic Network (BDSN) (*Romanowicz et al.*, 1993), NARS-Baja (*Trampert et al.*, 2003), and broadband PASSCAL arrays that have been archived at the IRIS Data Management Center. P waves on broadband (10 samples per second) vertical component velocity seismograms are corrected for the instrument response and high-pass filtered with a corner frequency of 120 s to reduce long-period noise. By visual inspection, we select the highest-quality recordings of P waves with signal-to-noise ratios of at least 20, low-amplitude coda, and impulsive onsets and we determine

time windows to ensure that the same features of P waveforms are analyzed. P wave spectra are estimated by multiple-taper spectral analysis (*Lees and Park*, 1995) and spectral ratios $\ln R$ are measured up to 1 Hz. The use of multiple-tapers produces smoother spectra and, hence, more robust estimates of $\ln R$. However, after experimentation with single and multiple tapers we observe that the spatial distribution of t_P^* depends little on the choice of the taper.

Figure 2.3 shows representative examples of spectral ratios and the measurement variability in Δt_P^* for ten deep earthquakes in South America recorded at stations CCM (Cathedral Cave, Missouri) and ANMO (Albuquerque, New Mexico). It demonstrates that, for nearly all earthquakes, the P wave signals at ANMO (which is located in TNA) are depleted in high frequencies compared to the P wave signals recorded at CCM (which is located in SNA). For each waveform pair, the spectral ratio lnR increases with increasing frequency and, hence, values for Δt_P^* ($t_{P_{CCM}}^* - t_{P_{ANMO}}^*$) are negative. This suggests that P waves propagating to ANMO are more attenuated. However, inferred values for Δt_P^* vary between –0.24 s and –1.09 s, more than measurement errors in Δt_P^* ($\pm$0.05 – 0.37 s). The variable Δt_P^* reflects the complex (nonlinear) character of $\ln R$, especially at frequencies larger than 0.8 Hz, which we attribute to receiver effects. In general, we obtain the most accurate measurements of Δt_P^* (i.e., measurements with uncertainties lower than 2σ) for P waves with simple waveforms composed of a single upswing and downswing and shortest durations. Presumably, these measurements better quantify the integrated effects of intrinsic attenuation on P wave spectra.

We observe significant variability of Δt_P^* for most station pairs (Figure 2.4). While absolute Δt_P^* values are larger than 0.1 s for about 75% of the measurements, the measurement uncertainty peaks at around 0.1 s. Thus, to constrain Δt_P^* we must rely on data redundancy and multiple measurements for earthquakes at different azimuths. Therefore we collect a data set of more than 63,000 spectral ratios using stations for

which we have at least two events.

2.4.2 Least Squares Inversion

To estimate t_P^* for each station, we solve a set of linear equations. First, the measurements of the slopes of the best fitting lines to $\ln R_{ij}$ provide estimates of the t_P^* difference ($\Delta t_{P_k}^*$) between stations i and j:

$$w_k^1 \left(t_{P_i}^* - t_{P_j}^* \right) = w_k^1 \Delta t_{P_k}^*. \tag{2.5}$$

Here, w_k^1 is a weight factor

$$w_k^1 = \exp\left[-(\epsilon_k/\epsilon_0)^2\right] \exp\left[-(\Delta_k/\Delta_0)^2\right], \tag{2.6}$$

which includes factors determined by the 2σ uncertainty in the $\Delta t_{P_k}^*$ measurement (ϵ_k) and the interstation distance (Δ_k). The first factor in (2.6) reduces the weight of measurements Δt_P^* with the highest 2σ uncertainty. The second factor reduces the weight of measurements of Δt_P^* for stations that are separated most and for which the effects of variable attenuation in the lower mantle may be greatest. We choose reference values $\epsilon_0 = 0.3$ s (Figure 2.4b) and $\Delta_0 = 10^\circ$ (Figure 2.4c) so that measurements with uncertainties larger than 0.3 s and measurements for which the station separations are more than 10° have weights that are reduced by at lease $1/e$. The inversion results change little when ϵ_0 is larger than 0.3 s and when Δ_0 is larger than 10° because $\Delta t_{P_k}^*$ for the same pair of stations have, in general, the same signs.

Second, we impose that the average value of t_P^* is zero:

$$\sum_{n=1}^{378} t_{P_n}^* = 0, \tag{2.7}$$

since the differential t_P^* measurements do not constrain the absolute value of t_P^*. Thus,

in our maps, only the variation in t_P^* is estimated.

Third, we impose smoothness constraints by penalizing t_P^* differences for closely located stations:

$$w_k^2 \left(t_{P_i}^* - t_{P_j}^* \right) = 0. \tag{2.8}$$

The factor

$$w_k^2 = \exp \left[-(\Delta_k / \Delta_R)^2 \right] \tag{2.9}$$

is largest when the angular distance Δ_k between stations i and j is smallest. In section 2.5.1, we experiment with values for the reference distance Δ_R by examining data misfit reduction and model norm.

Equations (2.5), (2.7), and (2.8) can be written in matrix form as

$$\mathbf{Gm} = \mathbf{d}, \tag{2.10}$$

where $\mathbf{m}$ is the model vector composed of t_P^* for 378 stations:

$$\mathbf{m} = \left(t_{P_1}^*, t_{P_2}^*, t_{P_3}^*, ..., t_{P_{378}}^* \right). \tag{2.11}$$

We solve (2.10) by least squares inversion.

2.5 t_P^* Structure

2.5.1 Effect of Smoothing

In order to determine the effects of the smoothing parameter Δ_R, we determine model norm $(\mathbf{m}/\mathbf{m}_0)^2$, misfit reduction $1 - ((\mathbf{Gm} - \mathbf{d})/\mathbf{d})^2$ (Figure 2.5), and t_P^* as a function of Δ_R (Figure 2.6). Figure 2.5 illustrates the trade-off between model norm and misfit reduction. For low values of Δ_R, the model norm is high ($|t_P^*|$ values are relatively large) and misfit reduction is highest (i.e., data fit is best). For increasing

Δ_R, both model norm and misfit reduction decrease and the t_P^* contrast between TNA and SNA emerges as the predominant signal. We choose $\Delta_R = 3^\circ$ as the preferred smoothness value as we suppress the strong variations in t_P^* for nearby stations within the western U.S. while maintaining coherent variations in t_P^* within TNA and SNA (e.g., relatively high t_P^* around the Appalachian) for which we may seek geophysical explanations. However, an acceptable misfit reduction is obtained for Δ_R as high as 7°.

2.5.2 Variation in t_P^*

Our preferred map of t_P^* variation (Figure 2.6b) shows both a simple regional trend and small-scale variations. The characteristic dichotomy of SNA and TNA is reflected in predominantly low t_P^* values for stations in SNA, including the Canadian Shield, Midcontinent, Grenville Province, and most of the Great Plains, while high values of t_P^* are observed in TNA. We illustrate the regional variation in t_P^* further by dividing the stations into four groups for distinct terrains in North America (Figure 2.7). The main variations can be associated with regional tectonic settings. Low t_P^* values for stations in SNA and high t_P^* values for stations in TNA are shown clearly in Figures 2.7a and 2.7b, respectively. On average, the difference in t_P^* between SNA and TNA is 0.23 s when no smoothing is applied and is 0.16 s if Δ_R is increased to 7°.

Smaller-scale (< 1000 km) variations of t_P^* are embedded within this large-scale trend and they are as strong as the bimodal TNA/SNA variation. We can readily recognize these variations in individual spectral ratio measurements. Compared to the predominant low t_P^* values at stations in SNA (Figure 2.7a), relatively high values for t_P^* are resolved for stations around the Appalachians and Gulf coast off the stable platform (Figure 2.7c), where mantle shear and P velocities are also relatively low. Low t_P^* are found under southern Alaska and around Baja California (Figure 2.7d),

probably associated with ongoing subduction in Alaska, while t_P^* are relatively high in the rest of western North America (Figure 2.7b).

2.6 Comparison With Other Studies

The first-order pattern of high t_P^* in TNA and low t_P^* in SNA is consistent with previous studies of short-period amplitude anomalies (*Cleary*, 1967; *Booth et al.*, 1974; *Der et al.*, 1982; *Butler*, 1984), spectral ratio variations (*Solomon and Toksöz*, 1970; *Der and McElfresh*, 1976, 1977; *Der et al.*, 1982), *Lg* coda waves (*Baqer and Mitchell*, 1998), and regional Rayleigh waves (*Mitchell*, 1975). The contrast in t_P^* of 0.2 s between SNA and TNA is consistent with that inferred by *Der et al.* (1982) who studied P wave spectra at frequencies up to 4 Hz. From P wave amplitudes, values of Δt_P^* larger than 0.4 s have been reported by *Solomon and Toksöz* (1970) and *Lay and Helmberger* (1981). In contrast, the recent study by *Lawrence et al.* (2006) suggests that there is no significant large-scale variation in t_P^* across North America. This observation is clearly inconsistent with our study. We speculate that the discrepancy is due to the fact that t_P^* variation may be difficult to detect in spectral ratios within the low frequency band (f $<$ 0.1 Hz) that *Lawrence et al.* (2006) use.

Lay and Wallace (1988) resolve strong Q_S variations within western North America using ScS multiples. Averaged over the upper 400 km of the mantle, they suggest that $Q_S = 25$ beneath the Basin and Range and $Q_S \geq 1000$ beneath the Pacific Northwest. This contrast would imply t_P^* variations of about 0.4 s, a factor of 2 higher than what we observe. This discrepancy that may partially be due to a strong D'' influence on ScS attenuation measurements. Strong (frequency-dependent) wave attenuation beneath the Basin and Range is also inferred from regional *Lg* wave (*Chavez and Priestley*, 1986; *Benz et al.*, 1997) and Rayleigh wave studies (*Hwang and Mitchell*, 1987).

The main patterns in our t_P^* maps, including those at regional scale, are similar

to those found in surface heat flow (Figure 2.8d). The low heat flow in southeastern U.S. does not correlate with the high t_P^* anomaly in this region. However, *Artemieva et al.* (2000) did infer higher lithospheric temperatures for the southeastern U.S. than in the SNA interior by reevaluation of heat flow data that takes into account the thermal properties of the region's crust. The similarity of surface heat flow and t_P^* implies that thermal structure affects intrinsic attenuation to a significant extent at shallow mantle depth.

Next, we make a more detailed comparison with two recent attenuation models based on surface wave analyses. We refer to these models as models Q and T. Model Q is the global model QRFSI12 by *Dalton et al.* (2008). Model T is derived from the regional S velocity model for NA00 (*van der Lee*, 2002) for North America by converting shear velocity to temperature *Goes and van der Lee* (2002). The conversion accounts for both elastic and anelastic sensitivity of the seismic waves to temperature and as a result yields an accompanying anelasticity model.

We denote predicted values of t_P^* for model Q as t_Q^*, using the subscript "Q" to emphasize that t_P^* values are computed using a Q_S model for the mantle. The predicted t_P^* for model T are denoted ad t_T^*, using a subscript "T" to indicate that we employ a temperature conversion to infer t_P^* from a tomographically derived shear velocity model.

The comparison with model Q (and t_Q^*) will help us gain insight into the compatibility of attenuation inferred from P wave spectra and long-period surface wave amplitudes. The comparison with model T (and t_T^*) will enable us to evaluate the similarity of regional-scale variations in t_P^* and shear velocity, and whether interpreting North American shear wave structure as being dominantly thermally controlled is compatible with independent constraints on attenuation. Figure 2.8 compares the t_P^* map from Figure 2.6b to predicted values of t_P^* across North America for models Q (t_Q^*) and T (t_T^*). The distribution of t_P^*, t_Q^*, and t_T^* is shown in Figure 2.7.

2.6.1 Model Q: Global Surface Wave Q Tomography

2.6.1.1 Model Q Background

Model QRFSI12 (*Dalton et al.*, 2008) is the most recent global Q_S model based on surface wave amplitudes. QRFSI12 has been derived using more than 30,000 Rayleigh wave amplitudes measurements. These amplitudes have been corrected for the effects of surface wave focusing and inverted simultaneously for three-dimensional attenuation (Q_S) and correction factors for the source and receiver. Lateral variations of Q_S in QRFSI12 are parameterized using spherical harmonics up to degree 12. The shortest wavelength variations are therefore about 3000 km which limits a comparison to continental-scale variations. We convert Q_S from QRFSI12 to Q_P using $Q_P = {}^3/_4(V_P/V_S)^2 Q_S$, assuming that attenuation in bulk is negligible, and we adopt V_P and V_S velocities from the PREM model (*Dziewonski and Anderson*, 1981).

We calculate t^*_Q by integrating along a P wave ray path for an epicentral distance of 70° through the upper 370 km of the mantle using (2.2). We assume that Q_P varies only with depth, because lateral variations in Q_P are smooth and teleseismic P wave propagate steeply through the uppermost mantle.

2.6.1.2 Comparison Between t^*_Q and t^*_P

The t^*_Q variation (Figure 2.8b) is, as expected, smooth given the relatively coarse lateral parameterization of QRFSI12. The contrast between SNA and TNA, a regional variation that is at the limit of global resolution in QRFSI12, is well reproduced in t^*_Q and correlates well with t^*_P, with a correlation coefficient of 0.30, on a point by point basis. The correlation coefficient increases to 0.38 and to 0.40 for $\Delta_R = 3°$ and $\Delta_R = 7°$, respectively.

The peak-to-peak variation in t^*_Q is a factor of 6 smaller than in the preferred t^*_P ($\Delta_R = 3°$). Even for stronger damped distributions of t^*_P ($\Delta_R = 12°$) for which

the lateral resolutions of t_Q^* and t_P^* are roughly equal, the amplitude in t_Q^* is still a factor of 2.2 smaller. We attribute the amplitude mismatch to the relatively long wavelength parameterization and strong damping used in constructing QRFSI12.

2.6.2 Model T: Regional Q_S From Temperature Estimates

2.6.2.1 Model T Background

Model T is a regional Q_S model derived from a purely thermal interpretation (*Goes and van der Lee*, 2002) of shear velocity model NA00 (*van der Lee*, 2002), assuming a constant pyrolitic composition. Taking into account that temperature variations affect both elastic and anelastic seismic structure, the conversion yields all elastic constants, density, and Q_S and Q_P for the temperature structure inferred from V_S. Because of the exponential dependence of anelasticity on temperature, even strong low-velocity anomalies generally translate into subsolidus temperatures that are compatible with temperatures derived from an independent V_P model and surface heat flow (*Goes and van der Lee*, 2002).

The temperature-velocity calculations were slightly updated from those used by *Goes and van der Lee* (2002) to make them more suitable for depths between 200 km and 400 km. We employ a finite, rather than infinite, strain equation of state that includes the effect of phase transformations within the pyrolitic mantle, as in the study by *Goes et al.* (2005). We use a temperature and depth-dependent anelasticity formulation: $Q_S(T,\ P) = Q_0\ \exp[gT_m(P)/T]$, where Q_0 is set to $0.1\omega^{0.15}$, ω is frequency, g is a constant scaling factor set to 40, T_m is the peridotite solidus, and T is absolute temperature. This is an empirical approximation of the common Arrhenius-type expression $Q_S(T,\ P) = Q_0\ \exp[(E^* + PV^*)/T]$, where E^* and V^* are activation energy and volume, respectively (*Karato and Spetzler*, 1990). Using the scaled homologous temperature, T/T_m, is a way of parameterizing the plausible decrease of V^* with depth (e.g., *Yamazaki and Karato*, 2001). A constant V^* yields

negative upper mantle Q_S depth gradients below the asthenosphere. At depths down to about 200 km, the model is similar to the average Q model Q_1 (with $E^* = 500$ kJ/mole and $V^* = 20$ m^3/mole) used by *Goes and van der Lee* (2002). Bulk Q is kept constant at a value of 1000. The updated procedure gives temperatures that are, within a few tens of degrees, i.e., within the uncertainties due to uncertainties in the mineral parameters, identical to those from *Goes and van der Lee* (2002).

2.6.2.2 Comparison Between t_T^* and t_P^*

Because of the relatively high lateral resolution of NA00, t_T^* (Figure 2.8c) shows more variability than t_Q^*. In addition to the bimodal SNA-TNA variation, t_T^* includes high values below the Appalachians and Gulf Coast, and lower values under the Colorado Plateau that are also observed in t_P^*. This indicates that not only the continental-scale pattern but some of the t_P^* features that are coherent on a 2° scale may be the result of intrinsic attenuation. However, the point-by-point correlation coefficient between t_P^* and t_T^* of 0.23 is relatively low and thus shows that many of the high and low shear velocity anomalies do not correspond to high and low Q anomalies.

The amplitude variation in t_T^* is in good agreement with the variation of t_P^*. The similar amplitudes of t_P^* and t_T^* indicate that the assumptions underlying the conversion of shear velocity variation to Q_P are reasonable. Q_P in model T varies over at least 6 orders of magnitude from essentially infinite under the North American shield, to minimum values of 40 (Q_S of 17) around 70 km depth below the western U.S. Higher Q_P (and hence higher Q_S) values within the western U.S. would reduce t_T^* values which already somewhat underestimate t_P^*.

Thus Q values below the western U.S. appear to be very low. Similarly low Q values have been invoked below mid-ocean ridges in models that reconcile oceanic lithospheric cooling models and sub-oceanic surface wave velocities (*Faul and Jackson*, 2005; *Priestley and McKenzie*, 2006). These models self-consistently generate a low-

velocity zone without requiring significant amounts of partial melt. However, surface wave analyses from data of the East Pacific Rise RIDGE experiment find minimum Q_S values no lower than 80 below the ridge (*Yang et al.*, 2007). To reconcile very low seismic velocities and moderately low Q_S values, the authors propose the presence of melt which does not attenuate substantially in the seismic frequency band but lowers seismic velocities due to elastic effects.

We find that for the western U.S., where mantle seismic velocities are, over 1000 km scales, as low as at mid-ocean ridges, measured t_P^* are matched well with very low Q values. Such low Q values can be purely thermal (as was assumed in their derivation), but may also be partially controlled by water content. *Dixon et al.* (2004) has proposed that the western U.S. subcrustal mantle is both hot and wet. As the seismic effect of water at shallow mantle depths is most likely predominantly anelastic, water affects seismic velocities and Q simultaneously, and cannot be distinguished from purely thermal effects without independent temperature data (*Karato*, 1993). The relatively large scatter in surface heat flow data and uncertainties in their extrapolation to temperature at depth does not preclude that part of the seismic structure is controlled by variations in water content (*Dixon et al.*, 2004). In any case, the variable seismic velocities in the North American upper mantle seismic structure are linked to strong attenuation variations. This strongly suggests that these seismic signatures are caused by variations in temperature and water content, and probably not by composition and melt.

2.7 Conclusions

We have inverted about 63,000 measurements of the spectral ratio of broadband (from one over signal length to 1 Hz) P waves generated by deep (focal depths > 200 km) earthquakes and recorded at 378 stations in North America. This large data set provides better constrained and more densely distributed information on uppermost

mantle P wave attenuation below the continent than has been previously available.

The pattern of t_P^* shows a systematic contrast between tectonic North America (TNA) and stable North America (SNA). t_P^* is relatively high in TNA and low in SNA consistent with high and low P wave attenuation in the upper mantle beneath TNA and SNA, respectively. This general pattern has been observed before in the U.S.; improved data coverage in Canada confirms that the continental-scale t_P^* pattern matches very well with the age of geological terrains and the seismic, heat flow, gravity, and magnetic variations across North America. The variation of t_P^* of 0.2 s between TNA and SNA is compatible with previous estimates.

We resolve regional variations in t_P^* which correlate with tectonics: relatively low t_P^* is associated with currently active subduction below Alaska. Relatively high t_P^* is found in SNA below the Appalachians and the Gulf Coast.

The consistency between patterns on the scale of around 200–500 km and tectonics suggests that the observed variations in t_P^* are predominantly due to intrinsic attenuation. The similar patterns in our t_P^* and predicted values for global attenuation model QRFSI12 (*Dalton et al.*, 2008) based on Rayleigh waves, which samples the upper mantle in a fundamentally different manner than teleseismic P waves, confirm this further. Compatibility with the t_P^* computed for attenuation estimated via a thermal interpretation of shear wave velocity anomalies in regional V_S model NA00, illustrates that variations in seismic velocity are predominantly due to physical effects with a strong attenuation signature, most likely temperature or a combination of temperature and water content.

2.8 Acknowledgments

Data have been provided by the IRIS/DMC, the GEOSCOPE Data Center, the Geological Survey of Canada, the Southern California Seismic Network (SCSN) Data Center operated by Caltech and USGS, and the Northern California Earthquake Data

Center (NCEDC), a joint project of the University of California Berkeley Seismological Laboratory (BSL) and the USGS. Figures are produced by GMT (Generic Mapping Tools) software. We thank Colleen Dalton for providing us with her Q model and for giving advice on model interpretation. We thank Jonathan Lees for providing us with the MTM (Multi-Taper Spectral Analysis Methods) software. Constructive comments by two anonymous reviewers and the Associate Editor helped us improve the article. This research has been supported by NSF grant EAR-0609763.

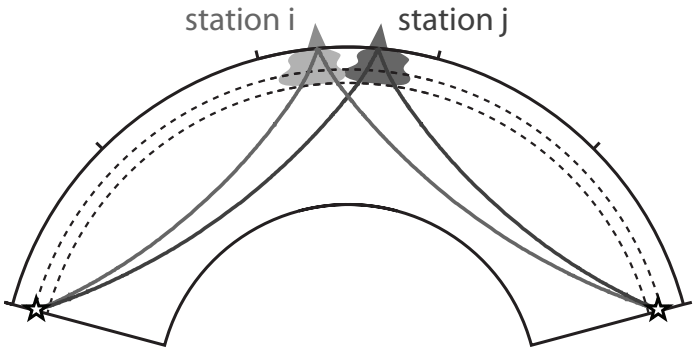

Figure 2.1: Geometrical ray paths of P waves propagating from deep earthquake sources (stars) to stations at teleseismic distances (triangles).

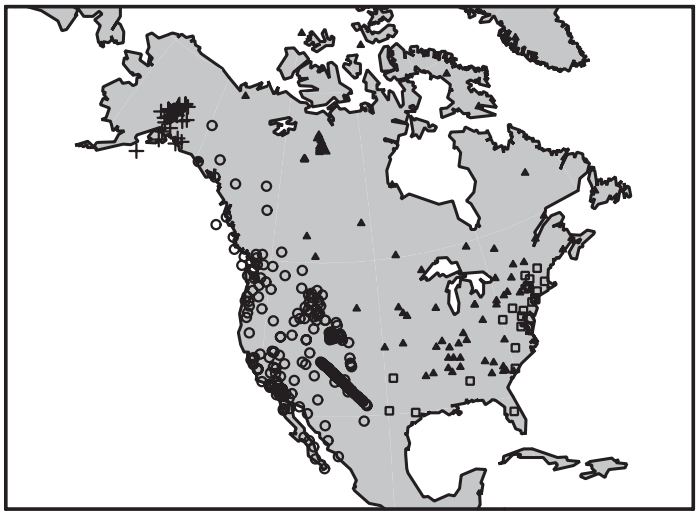

Figure 2.2: Open circles, closed triangles, open squares, and crosses indicate the locations of the 378 seismic stations used in this study. These stations are located in, respectively, SNA, TNA, the off-platform region, and subduction zone in southern Alaska.

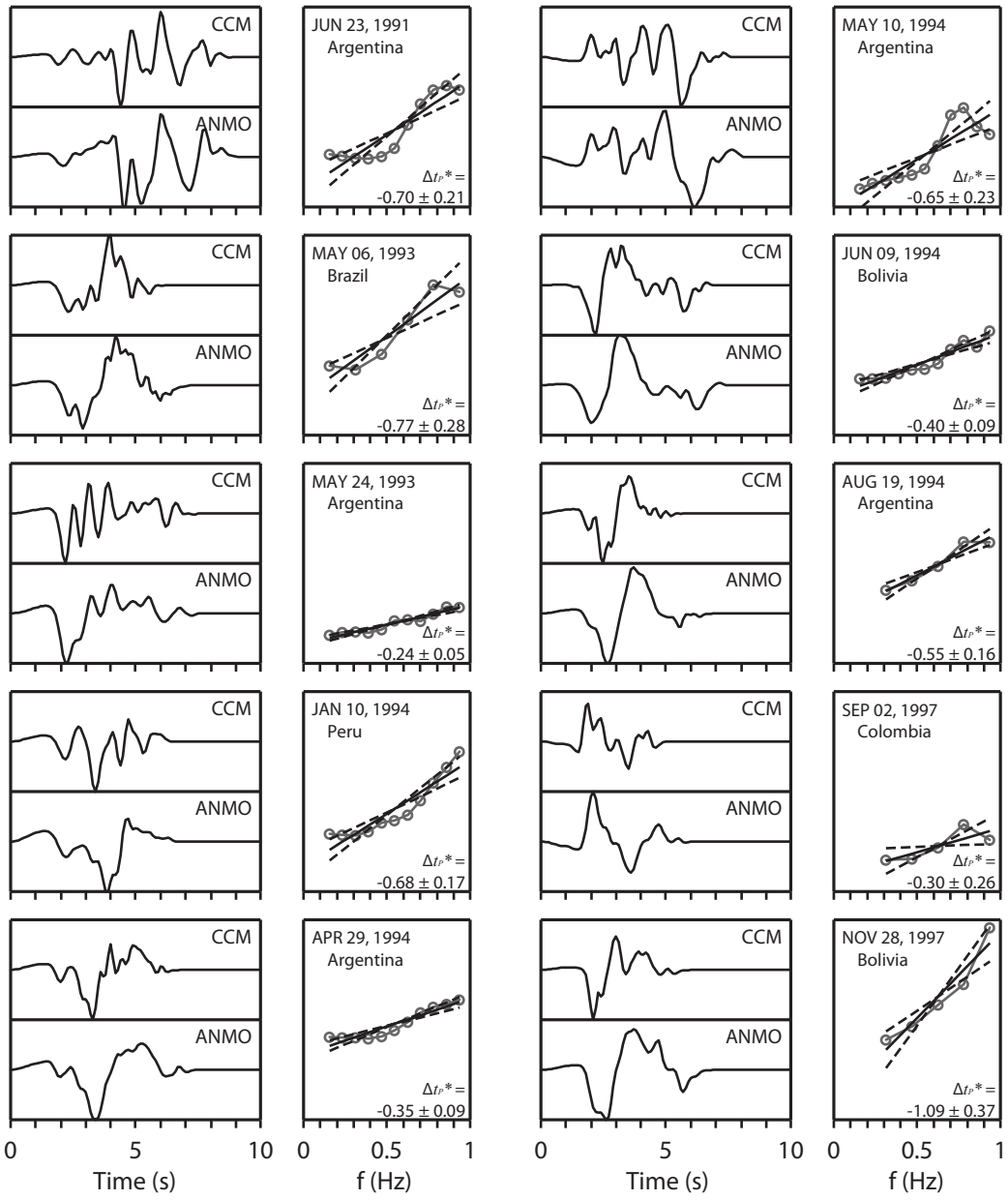

Figure 2.3: Selected measurements of Δt_P^* between stations CCM (Cathedral Caves, MO) and ANMO (Albuquerque, NM) for ten deep earthquakes in South America. (left) Vertical component velocity waveforms. Trace windows are manually determined such that seismograms for the same event contain the same features of P wave arrivals. (right) Natural logarithm of spectral ratios $\ln R(f)$ (gray lines with circles), best fitting lines to $\ln R$ (black solid lines), and lines with slopes that bracket the 95% certainty of the slope (black dashed lines). Δt_P^* measurements and their uncertainties are in seconds.

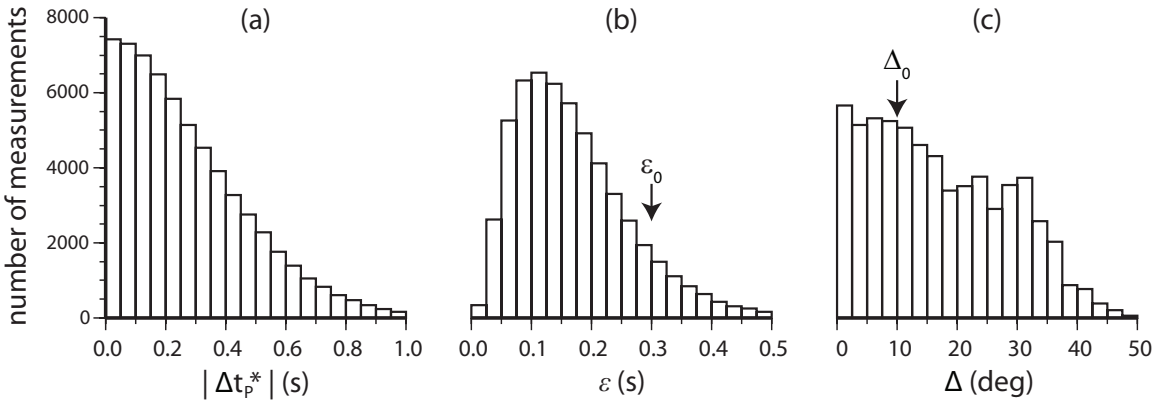

Figure 2.4: (a) Distribution of $|\Delta t_P^*|$. (b) Distribution of 95% confidence ranges of Δt_P^*. Reference value $\varepsilon_0 = 0.3$ s is chosen. (c) Interstation distance distribution of station pairs used in this study. Reference value $\Delta_0 = 10^\circ$ is chosen.

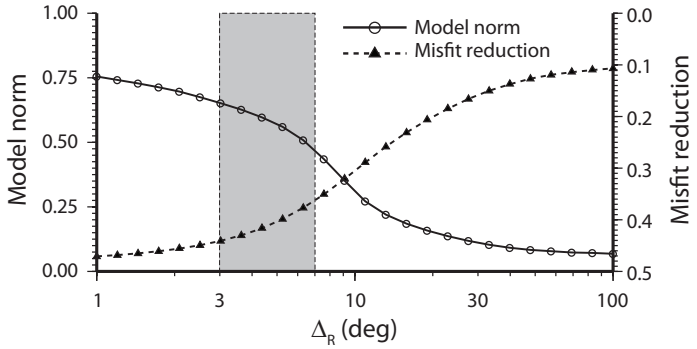

Figure 2.5: Trace-off curves for the model norm (solid line with circles) and the misfit reduction (dashed line with triangles) as a function of Δ_R. Circles and triangles are calculated data points of the model norm and the misfit reduction, respectively. Values of Δ_R in the shaded region ($\Delta_R = 3 - 7^\circ$) are preferred values.

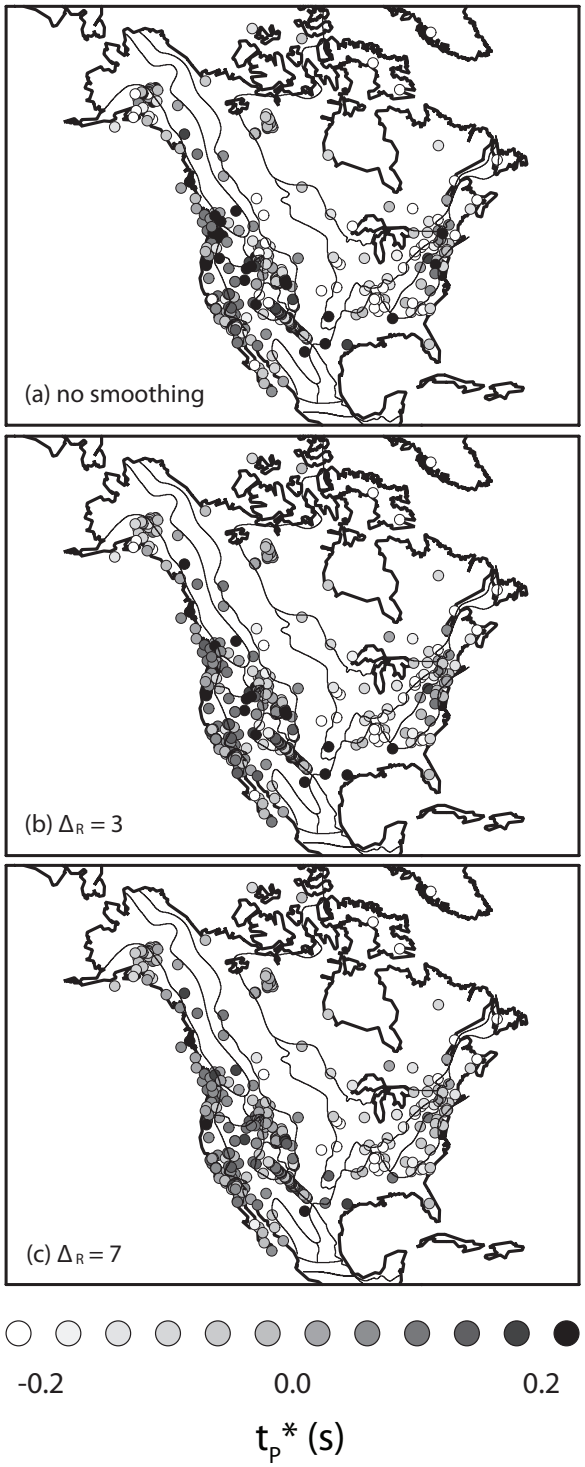

Figure 2.6: Maps of t_P^* resolved with varying smoothing parameters Δ_R. (a) No smoothing is imposed. (b) $\Delta_R = 3°$. (c) $\Delta_R = 7°$.

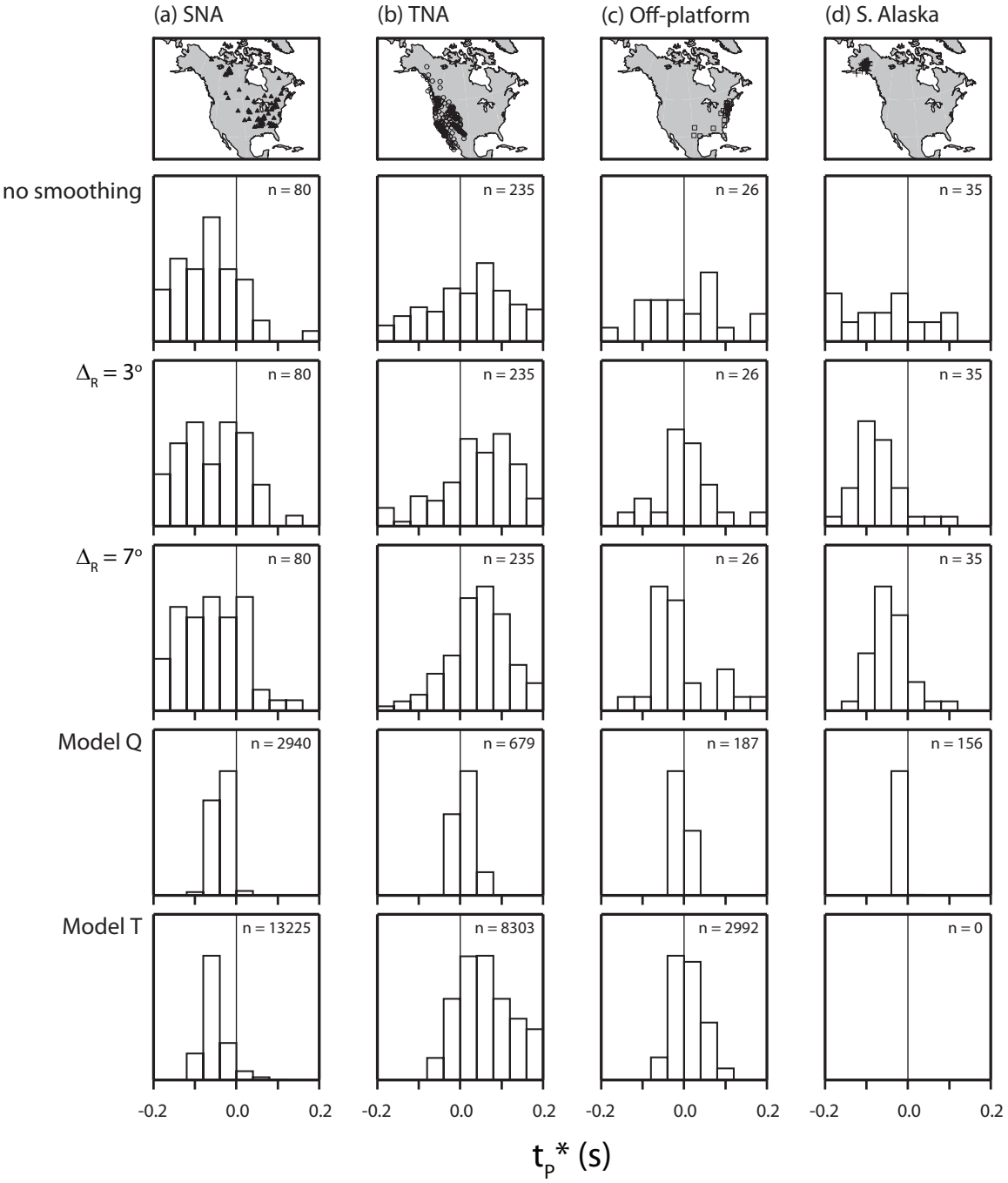

Figure 2.7: Distributions of t_P^* (this article), t_Q^* (from model Q: global surface Q tomography (*Dalton et al.*, 2008)), and t_T^* (from model T: regional Q_S from temperature estimates (*Goes and van der Lee*, 2002)) for stations in (a) SNA, (b) TNA, (c) off-platform region, and (d) subduction zone in southern Alaska. n represents the total number of data points used to produce each distribution diagrams.

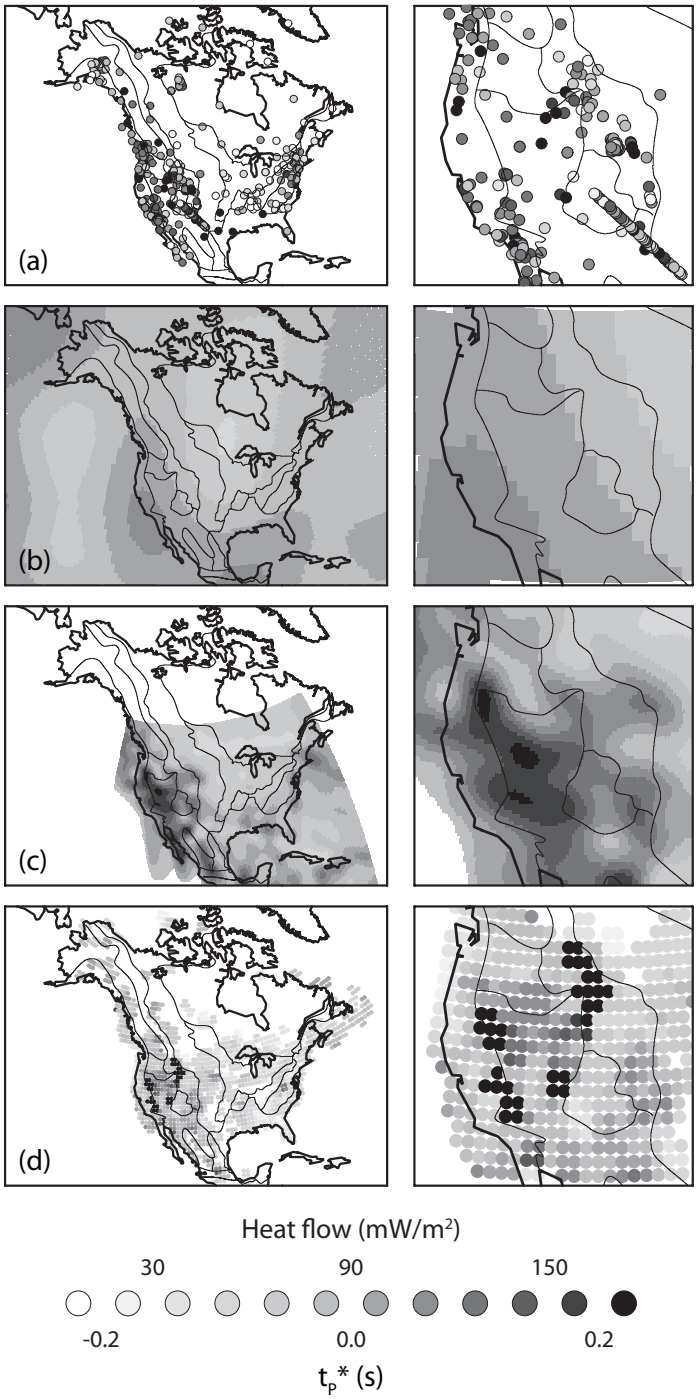

Figure 2.8: (a) Variation of t_P^* for $\Delta_R = 3°$. (b) Variation of t_Q^* (from model Q: global surface Q tomography (*Dalton et al.*, 2008)). (c) Variation of t_T^* (from model T: regional Q_S from temperature estimates (*Goes and van der Lee*, 2002)). (d) Variation of cap-averaged heat flow data from *Pollack et al.* (1993). (left) Variations in North America. (right) Variations within TNA.

CHAPTER III

Global variation of body-wave attenuation in the upper mantle from teleseismic P wave and S wave spectra

3.1 Abstract

We constrain the spatial variation of P-wave (t_P^*) and S-wave (t_S^*) attenuation by inverting 190,000 teleseismic P- and S-wave spectra up to 0.8 Hz. These spectra are derived from 250 deep earthquakes recorded at 880 broadband global and regional network stations. The variance and ratios of t_P^* and t_S^* values are consistent with PREM's upper mantle velocity and Q structures and conventional t_P^* and t_S^* values. High attenuation is resolved beneath stations in tectonically active regions characterized by high heat flow. Low attenuation marks stable continental regions. The maps of t_P^* and t_S^* correlate well with the variations of t_S^* computed and inferred from (1) the most recent surface-wave Q model and (2) a thermal interpretation of shear-wave velocity tomography. This indicates that maps of body- and surface-wave attenuation reflect intrinsic attenuation and variable temperature in the mantle.

This chapter has originally been published in Hwang, Y. K., J. Ritsema, and S. Goes (2011), Global variation of body-wave attenuation in the upper mantle from teleseismic P wave and S wave spectra, *Geophys. Res. Lett., 38* (L08311) doi:10.1029/2011GL046812.

3.2 Introduction

Models of the elastic velocity structure of the mantle have advanced our knowledge of mantle dynamics (e.g., *Romanowicz*, 2008), but are by themselves insufficient to obtain complete descriptions of the physical state of Earth's interior. Anelasticity models can provide important complementary information. Anelasticity has a much stronger sensitivity to temperature and water content than elastic velocities, a lower sensitivity to composition and a different sensitivity to melt (e.g., *Anderson*, 1967; *Karato and Jung*, 1998; *Hammond and Humphreys*, 2000a; *Jackson et al.*, 2002; *Faul et al.*, 2004; *Shito et al.*, 2006).

A number of studies have mapped the global variation of seismic wave attenuation in the upper mantle using surface waves (e.g., *Romanowicz*, 1995; *Billien et al.*, 2000; *Gung and Romanowicz*, 2004; *Selby and Woodhouse*, 2002; *Dalton and Ekström*, 2006; *Dalton et al.*, 2008) and body waves (e.g., *Bhattacharyya et al.*, 1996; *Reid et al.*, 2001; *Warren and Shearer*, 2002; *Lawrence and Wysession*, 2006b). Here we add a new estimate of attenuation in the upper mantle from teleseismic P-wave and S-wave spectra. Using globally distributed stations, we invert ratios of body-wave spectra for the P-wave and S-wave attenuation parameters t_P^* and t_S^*. We compare our maps of t_P^* and t_S^* to surface-wave Q tomography and attenuation maps inferred from a thermal interpretation of shear-velocity tomography.

3.3 Spectral analysis of P and S waves

The attenuation parameter t^* is defined as the ratio between the body-wave traveltime t and the quality factor Q along the (ray) path L (e.g., *Stein and Wysession*, 2003):

$$t^* = \int_L \frac{\mathrm{d}t}{Q}. \tag{3.1}$$

If we write the spectrum $O(\omega)$ as the product of the source spectrum $S(\omega)$ and the attenuation function $e^{-\omega t^*/2}$,

$$O(\omega) = S(\omega)e^{-\omega t^*/2}, \tag{3.2}$$

the logarithm of the spectral ratio R_{ij} between $O_i(\omega)$ and $O_j(\omega)$,

$$\ln R_{ij}(\omega) = -\frac{\omega}{2}\Delta t^*_{ij}, \tag{3.3}$$

is linearly related to the difference between the attenuation parameters at stations i and j. Here, $\Delta t^*_{ij} = t^*_i - t^*_j$.

To isolate the influence of intrinsic attenuation on t^* from other sources such as crustal amplification, scattering, focusing and defocusing, we use large number of spectral ratio measurements. Our data set comprises 190,000 P- and S-wave spectral ratios from broadband recordings of 250 earthquakes with magnitudes larger than 6. The earthquake focal depths are larger than 200 km to ensure short source-time functions and to avoid interference of the direct P- and S-waves with the surface reflections pP, sP, and sS. We analyze the spectra at teleseismic distances (30°–85°) to avoid waveform complexities from triplication in the transition zone and diffraction along the core-mantle boundary. We select 10–30 s long segments of P-wave and S-wave signals with impulsive onsets, low-amplitude coda, high signal-to-noise ratios, and similar waveforms for the same earthquakes. To minimize the variations of spectra due to varying source azimuths, we measure Δt^*_P for station pairs that have similar azimuths.

We determine $\ln R(\omega)$ up to a frequency of 0.8 Hz using the multiple-taper spectral analysis method of *Lees and Park* (1995). Δt^*_P (for P-waves) and Δt^*_S (for S-waves) and 2σ uncertainties are estimated by linear regression of $\ln R(\omega)$. We apply a correction using the results of *Hwang and Ritsema* (2011) to account for the systematic

increase of t_P^* and t_S^* in the teleseismic distance range by about 0.2 s and 0.7 s, respectively.

Station-specific t_P^* and t_S^* values are determined by least-squares inversion of the Δt_P^* and Δt_S^* measurements. Since we cannot infer absolute values from spectral ratios, we constrain the mean values of t_P^* and t_S^* to be zero. We regularize the inversion by reducing the weight of Δt_P^* and Δt_S^* measurements with large 2σ uncertainties and measurements for large inter-station distances. Details of the Δt^* measurements and uncertainties can be found in *Hwang et al.* (2009) and *Hwang and Ritsema* (2011).

3.4 Results

3.4.1 Lateral t_P^* and t_S^* variations

Since t_P^* and t_S^* are affected by wave scattering and near-surface 'site-responses', we investigate the average values of t_P^* and t_S^* within overlapping circles with radii of 3° (Figures 3.1a and 3.1b). The averaging of the data brings out the large-scale patterns of t_P^* and t_S^* that reflect global tectonics and that are similar to the global heat flow variations (Figure 3.1c).

The spatial variations of t_P^* and t_S^* are similar and the ratio of t_P^* and t_S^* variances ($\sim$4 s) is consistent with the expected ratio of 4.5 for the upper mantle Q structure of PREM (*Dziewonski and Anderson*, 1981) and the conventional value of 3.5 for the t_S^*/t_P^* ratio (e.g., *Cormier*, 1982) (Figure 3.2). This indicates that variations in t_P^* and t_S^* do indeed reflect the lateral variation of intrinsic attenuation in the upper mantle.

3.4.2 Joint inversion for t_S^*

In Figure 3.3a, we show the map of t_S^* by a joint inversion of Δt_P^* and Δt_S^*. To relate the Δt_P^* data to Δt_S^* in the upper mantle, we have used

$$\Delta t_S^* = \frac{3}{4} \frac{\int (V_P^2/V_S^3) \mathrm{d}s}{\int (1/V_P) \mathrm{d}s} \Delta t_P^* \tag{3.4}$$

using velocity structures (V_P and V_S) of PREM and assuming that Δt^* is due to laterally varying Q in the upper mantle only and that bulk attenuation is negligible (e.g., *Anderson and Given*, 1982).

Figure 3.3a shows the global distribution of t_S^* in a map that has been smoothed by cap-averaging. High attenuation characterizes tectonically active collision zones, rift zones and back-arc regions, while low attenuation is found below stable continental cores. For example, t_S^* is relatively high in the tectonically-active western North America and low in the platforms of central and eastern North America. A similar contrast is also apparent in Europe: t_S^* is higher in western Europe than in the Baltic shield region. Station density is lower in other regions but a pattern consistent with tectonics persists. For example, t_S^* is low in the East African Rift region and high at stations within the western and southern cratons of Africa. In addition, t_S^* is low in the back-arc regions of the western Pacific subduction zones.

3.4.3 Comparison with seismic tomography

We compare the map of t_S^* based on the spectral ratios of P- and S-waves with the t_S^* variation computed by integrating through two Q models for the upper 400 km of the mantle using equation (3.1). In Figure 3.3b, we show the distribution of t_S^*, and denote it as t_Q^*, predicted by the model QRFSI12 (*Dalton et al.*, 2008) for the upper mantle. QRFSI12 is a spherical harmonic degree-12 model of shear attenuation derived using fundamental-mode Rayleigh-wave amplitudes in the long-

period range (50–250 s). The data set of Rayleigh-wave amplitudes are corrected for source, instrument, and focusing effects.

In Figure 3.3c, we show t^*_S, and denote it as t^*_T, for the Q structure based on a thermal interpretation of S20RTS (*Ritsema et al.*, 1999) shear-velocity anomalies with respect to the Ocean Reference Model of *Ritsema and Allen* (2003). For the conversion from dV_S to temperature anomalies we assume that the mantle has a homogeneous pyrolitic composition and that below a PREM lithospheric structure, the average velocity profile corresponds to a mantle adiabat with a potential temperature of 1300°C. Elastic velocities are calculated using a finite-strain approach (*Cammarano et al.*, 2003; *Goes et al.*, 2005) with a correction for anelastic effects using an Arrhenius-type pressure and temperature-dependent Q formulation (*Karato*, 1993; *Goes et al.*, 2005): $Q_S(T,P) = Q_0 \exp\{gT_m(P)/T\}$, where T and P are absolute temperature and pressure, respectively, $Q_0 = 0.1\,\omega^{0.15}$, g (= 40) is a scaling factor, and T_m is the peridotite solidus. The conversion yields temperature, and corresponding V_P, density, Q_S and Q_P. Regional models under North America, Europe and Australia converted in a similar manner yielded temperatures that could reconcile observed V_P, V_S and surface heat flow (*Goes et al.*, 2000, 2005; *Goes and van der Lee*, 2002). The long-wavelength thermal structure inferred from S20RTS has reasonable temperatures varying between 500°C and 1300°C at 50 km depth and 1450–1650°C at 400 km depth (Figure 3.4).

3.5 Discussion

There is a remarkable similarity between t^*_S, t^*_Q, and t^*_T. This indicates that surface-wave amplitudes and body-wave spectra are affected by the same long-wavelength variation in attenuation even though the wavelengths and propagation directions of surface-waves and body-waves are entirely different.

The variations in t^*_S values are larger than the variations in t^*_Q and t^*_T. For example,

the contrast between western North America and stable North America and between western Europe and the Baltic region is about 0.7 s in t_S^* but about 0.3 s and 0.5 s for t_Q^* and t_T^*, respectively. However, these differences are to be expected given the uncertainties originating from averaging (t_S^*), the regularization of the inverse problem (t_Q^*), and uncertainties of the velocity-temperature conversion (t_T^*).

The correlation between patterns in t_S^*, surface heat flow, tectonics and shear-velocity anomalies suggest attenuation is largely the result of thermally activated creep. The conclusion that temperature exerts the main control on global Q_S and V_S structures is consistent with other studies (*Artemieva et al.*, 2004; *Dalton et al.*, 2009; *Dalton and Faul*, 2010). Our analyses illustrate that the maps of t_S^* and t_Q^* can be explained by variations of intrinsic attenuation consistent with a temperature variation as that depicted in Figure 3.4.

Other factors such as the presence of melt below mid-ocean ridges and a melt-depleted composition of cratonic roots likely have additional influence (*Artemieva et al.*, 2004; *Dalton et al.*, 2009; *Dalton and Faul*, 2010). The back-arc high t_S^* and t_Q^* anomalies that coincide with low shear velocities, which we have interpreted as high temperatures, may partially reflect high water content compatible with an interpretation of regional V_P, V_S, and Q_P below the Izu-Bonin arc (*Shito et al.*, 2006). To better distinguish between different mechanisms requires an imaging of t_S^*, t_P^*, and seismic velocities at more similar resolution and scale than the models we compared here.

3.6 Conclusions

New maps of t_P^* and t_S^*, derived from 190,000 teleseismic, global P-wave and S-wave spectra, exhibit a coherent large-scale spatial variation that is consistent with heat flow and tectonic variations. The ratio of t_S^* to t_P^* is consistent with the PREM ratio of 4.5 and the conventional t_S^* to t_P^* ratio of 3.5. Moreover, a joint inversion

of the P-wave and S-wave spectral ratios yields lateral variation of t_S^* that is similar to the predicted t_S^* variation for a recent surface-wave Q model (t_Q^*) of the upper mantle and a thermal interpretation of shear-velocity anomalies in the upper mantle (t_T^*). Combined these observations indicate that the large-scale pattern in t_P^* and t_S^* reflects variations in intrinsic shear attenuation.

The high correlation between t_S^* and t_Q^* indicates that coherent patterns of attenuation can be constrained from large data sets of horizontally and vertically propagating waves. The similarity between t_S^*, t_Q^*, and t_T^* suggests that the patterns of Figure 3.3 predominantly reflects variable attenuation in the upper few hundred kilometers of the mantle. The patterns are consistent with a thermal structure of the mantle as inferred from shear velocity anomalies.

3.7 Acknowledgments

We thank the two anonymous reviewers for their constructive comments. This research was funded by NSF grant EAR–0944167. Data were provided by the IRIS/DMC.

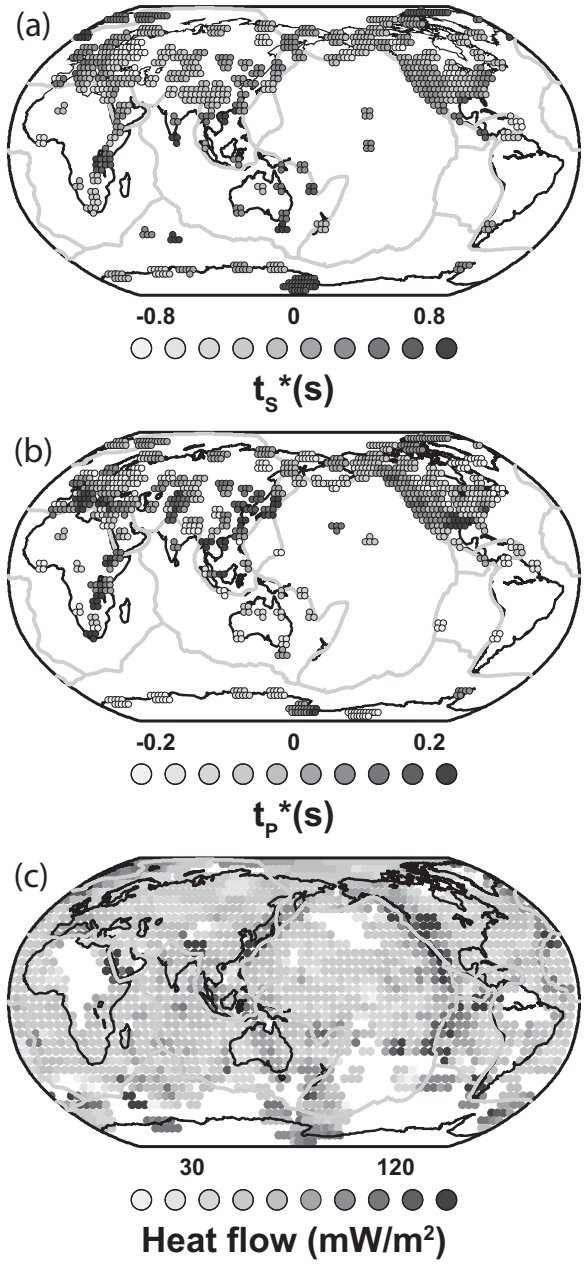

Figure 3.1: Spatial variations of (a) t_S^* and (b) t_P^* in the upper mantle. The t_S^* and t_P^* values have been averaged using overlapping caps with radii of 3°. Note that variations in t_S^* and t_P^* are similar. (c) Global heat flow distribution according to *Pollack et al.* (1993).

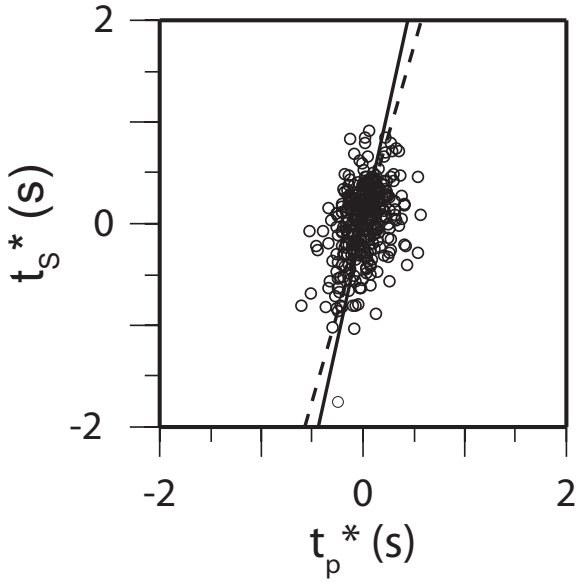

Figure 3.2: The correlation of t_S^* versus t_P^* after correction for epicentral distance. The solid line represents $t_S^* = 4.5\, t_P^*$ as predicted by the PREM velocity and Q structures and the dashed line represents $t_S^* = 3.5\, t_P^*$, the ratio for conventional t_S^* to t_P^* ratio values reviewed by *Cormier* (1982).

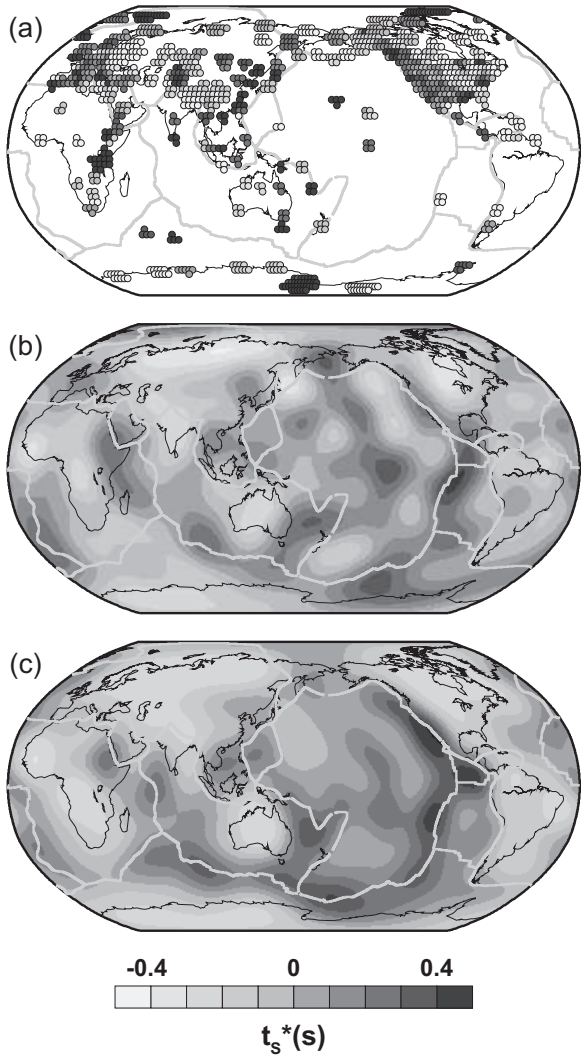

Figure 3.3: Spatial variation of t_S^* in the upper mantle estimated (a) by joint inversion of Δt_P^* and Δt_S^*, (b) from the surface-wave Q model of *Dalton et al.* (2008) (t_Q^*), and (c) from the thermal interpretation of S20RTS (t_T^*). The correlation coefficient between t_S^* (a) and t_Q^* (b) and between t_S^* (a) and t_T^* (c) are about 0.3.

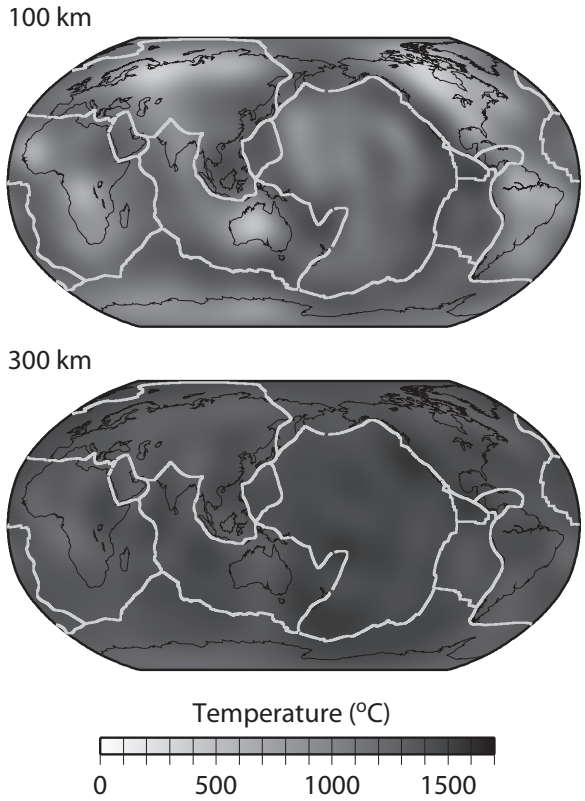

Figure 3.4: Temperatures at depths of (top) 100 km and (bottom) 300 km inferred from S20RTS (*Ritsema et al.*, 1999) using the conversion of *Goes et al.* (2005). The temperatures at 100 km reflect surface tectonics. The temperature is relatively low beneath old, stable cratons and relatively high below mid-ocean ridges. The high temperatures behind circum-Pacific subduction zones are likely biased high by high water content in the mantle wedge. At 300 km depth, a weak thermal imprint persists below the base of the cratonic roots, while relatively hot regions have largely lost their correlation with ridge geometry. Narrow subducting slabs are not resolved in this long-wavelength model.

CHAPTER IV

Radial Q_μ structure of the lower mantle from teleseismic body-wave spectra

4.1 Abstract

We have measured 150,000 P- and 130,000 S-wave spectral ratios up to 0.8 Hz using recordings of 250 deep (focal depth > 200 km) earthquakes from 890 global and regional network stations. We have inverted these data to estimate the attenuation parameters t_P^* and t_S^* for P- and S-waves and a radial profile of the quality factor Q_μ for the lower mantle. On average, t_P^* increases by about 0.2 s and t_S^* increases by about 0.7 s between epicentral distances of 30° and 97°. The relatively strong increase of t_S^* ($t_S^* \approx 4\,t_P^*$) suggests that intrinsic shear attenuation is the cause of the overall trend in our data. The increase of t_P^* and t_S^* with distance is smaller than predicted by models PREM (*Dziewonski and Anderson*, 1981), QL6 (*Durek and Ekström*, 1996), and QLM9 (*Lawrence and Wysession*, 2006a). Assuming PREM values for Q_μ in the upper mantle, where the data lack resolving power, the P- and S-wave spectra are explained best if Q_μ increases from about 360 at PREM's 670-km discontinuity to 670 in the lowermost mantle. The high values for Q_μ can be reconciled with previously

This chapter has originally been published in Hwang, Y. K., and J. Ritsema (2011), Radial Q_μ structure of the lower mantle from teleseismic body-wave spectra *Earth Planet. Sci. Lett., 303*, 369–375.

determined values by invoking a frequency-dependence of $Q_\mu(\omega)$ that is proportional to $\omega^{0.1}$. Data that are separated in 'Pacific' and 'circum-Pacific' subsets have slightly different trends. Estimates of t_P^* and t_S^* for the Pacific data, which sample the large low shear-velocity province of the Pacific, are higher than the circum-Pacific estimates. Thus, it appears that the Pacific large low shear velocity province has accompanying low Q_μ. The difference in Q_μ in the lowermost 1000 km of the mantle beneath the Pacific and beneath the circum-Pacific is at most 17%. Lateral variations of this magnitude are marginally resolvable given the uncertainties of our measurements.

4.2 Introduction

Although seismic constraints of the mantle have come primarily from studies on elastic velocities, it is well recognized that joint interpretations of seismic velocities and attenuation are critical for understanding the structure and dynamical state of the Earth's interior.

Global variations of attenuation in the upper mantle have been estimated using both surface-waves (e.g., *Romanowicz*, 1995; *Billien et al.*, 2000; *Selby and Woodhouse*, 2002; *Gung and Romanowicz*, 2004; *Dalton et al.*, 2008) and body-waves (e.g., *Bhattacharyya et al.*, 1996; *Reid et al.*, 2001; *Warren and Shearer*, 2002). These global-scale studies are consistent with regional-scale studies (e.g., *Sheehan and Solomon*, 1992; *Baqer and Mitchell*, 1998; *Roth et al.*, 2000; *Lawrence et al.*, 2006; *Hwang et al.*, 2009) and indicate that the upper 200–300 km of the mantle beneath oceans and tectonically active regions is generally more attenuating than the mantle beneath stable, continental shields.

Except for the study by *Lawrence and Wysession* (2006b), wave attenuation in the lower mantle has been modeled using 1D profiles (Figure 4.1). Whole-mantle profiles, constrained by normal-modes (*Dziewonski and Anderson*, 1981; *Widmer et al.*, 1991; *Durek and Ekström*, 1996; *Roult and Clévédé*, 2000; *Resovsky et al.*, 2005) and ScS/S

waveforms (*Lawrence and Wysession*, 2006a), have a common low Q_μ layer in the uppermost mantle (80–200 km depth), intermediate Q_μ values in the transition zone (200–650 km), and the highest Q_μ values in the lower mantle. However, absolute values of Q_μ and the depth dependence of Q_μ in the lower mantle differ in these profiles. PREM (*Dziewonski and Anderson*, 1981) and QL6 (*Durek and Ekström*, 1996) indicate constant values of 312 and 355 in the lower mantle, respectively. *Oki and Shearer* (2008) resolve lower mantle Q_μ value of about 620 using S-P ratio method at short-period band (3 – 10 s). *Resovsky et al.* (2005) constrain Q_μ to decrease in the lowermost 1000 km of the mantle. Q_μ in PAR3P (*Okal and Jo*, 1990) and QM1 (*Widmer et al.*, 1991) decrease throughout the lower mantle while it increases in the lower 1000 km of the lower mantle in model QLM9 (*Lawrence and Wysession*, 2006a). The study of *Warren and Shearer* (2000) provide a high-frequency (0.16 – 0.86 Hz) estimate of Q_P from global P and PP spectra. Their frequency-independent Q_P is about 2600 in the lower mantle which is more than three times larger than the Q_P value of 780 in PREM. Variable approaches, data sets and measurement uncertainties are responsible for these differences and underscore that the basic radial structure of Q is still poorly constrained.

In this study, we follow a classical approach in which Q is determined from the epicentral distance variation of the body-wave attenuation parameters t_P^* and t_S^*. The original study by *Teng* (1968) and subsequent studies of spectral ratios (e.g., *Solomon and Toksöz*, 1970; *Der and McElfresh*, 1977; *Der et al.*, 1982) and amplitude decay (e.g., *Booth et al.*, 1974; *Butler and Ruff*, 1980) were mostly applied to band-limited, analog waveform data from the United States. Here, we measure t_P^* and t_S^* from a nearly two-decade long collection of digital waveforms from broadband seismic stations in regional and global networks. We describe our data in section 4.3. We review methods and describe the epicentral variation of t_P^* and t_S^* and the inferred radial variation of Q_μ in sections 4.4 and 4.5, respectively. Final conclusions are

drawn in section 4.6.

4.3 Data

4.3.1 Teleseismic body-wave spectra

The attenuation parameter t^* is defined as the ratio of the body-wave traveltime t and the quality factor Q integrated along the ray path (e.g., *Stein and Wysession*, 2003):

$$t^* = \int_{\text{ray}} \frac{\mathrm{d}t}{Q}. \tag{4.1}$$

We use t^*_P and t^*_S and Q_P and Q_μ to denote the attenuation parameters and quality factors of P- and S-waves, respectively. Since the amplitude spectrum of a body-wave is proportional to the attenuation function $\exp\left(-\frac{1}{2}\omega t^*\right)$, the ratio $R_{ij}(\omega)$ of spectra $O_i(\omega)$ and $O_j(\omega)$ for the same earthquake is related linearly to the t^* difference recorded at stations i and j (*Teng*, 1968):

$$\ln R_{ij}(\omega) = -\frac{\omega}{2}\Delta t^*_{ij}. \tag{4.2}$$

While we have previously investigated spectral ratios of P-waves to map lateral variation of t^*_P (*Hwang et al.*, 2009), we study here the variation of t^*_P and new measurements of t^*_S as a function of epicentral distance. If Δ_i and Δ_j are the epicentral distances of stations i and j, we associate

$$\Delta t^*_{ij} = t^*_{\Delta_i} - t^*_{\Delta_j} \tag{4.3}$$

to depth-dependent attenuation in the lower mantle, using the fact that P- and S-wave turning depths increase monotonously with epicentral distance (Figure 4.2).

Q_μ is related to Q_P by

$$Q_P^{-1} = LQ_\mu^{-1} + (1 - L)Q_\kappa^{-1}, \tag{4.4}$$

where $L = \frac{4}{3}(V_S/V_P)^2$ and V_S and V_P are the S- and P-wave velocities (e.g., *Anderson and Given*, 1982). If shear attenuation is much larger than bulk attenuation (i.e., $Q_\mu \ll Q_\kappa$), then

$$Q_P^{-1} = LQ_\mu^{-1}. \tag{4.5}$$

Equation (4.5) predicts that t_P^* and t_S^* differ by about a factor of 4.5 and that the Q_P/Q_μ ratio is 2.25 (depending on the velocity structure of the mantle) which is almost the same as the Q_P/Q_μ ratio of 2.27 estimated in this study.

4.3.2 Measurements

We measure Δt^* using more than 150,000 P-wave and 130,000 S-wave spectral ratios from about 250 events with magnitudes larger than 6. The events occurred between 1987 and 2005 and have been recorded by broadband seismometers from global (GSN and Geoscope) and numerous regional networks. The focal depths of the earthquakes are larger than 200 km so that the P and S signals are not complicated by surface reflections (i.e., pP, sP, and sS) and not attenuated strongly by the uppermost mantle in the source region. We limit the analysis to epicentral distances larger than 30° to avoid waveform complexity due to strong velocity gradients in the upper mantle and to distances smaller than 97° to avoid the effects of diffraction along the core. A high-pass filter with a corner frequency of 120 s is applied to the vertical-component P-wave and the transverse-component S-wave.

We inspect all waveforms to ensure that the signals are well above noise level, and have low-amplitude coda and impulse onsets. Typically, P-wave and S-wave time windows are about 8 s and 27 s long, respectively. However, we adjust these to

isolate waveforms with similar characteristics. We measure Δt^* for pairs of stations that have similar source azimuths to minimize the effects of rupture directivity on the spectra. Examples of waveforms and spectral ratios have been shown by *Hwang et al.* (2009). The amplitude spectra are estimated up to 0.8 Hz using the multiple-taper spectral analysis of *Lees and Park* (1995). Δt^* and its uncertainty are estimated by linear regression.

Δt^* incorporates the effect of lateral variation in t^*, the influence of heterogeneity in the crust and mantle, scattering, and station 'site effects'. In addition, measurement errors in Δt^* arise due to the unstable nature of spectral ratios. Nevertheless, a signal of intrinsic attenuation is evident in our data when we plot Δt^* as a function of inter-station distance $d\Delta_{ij} = |\Delta_i - \Delta_j|$ (Figure 4.3). Two aspects characterize intrinsic attenuation. First, the weighted average values of Δt^*_{ij} increase smoothly with increasing $d\Delta$ up to at least 45°. Second, the increase of Δt^*_S is about four times stronger than the increase of Δt^*_P. This is consistent with equation (4.5) and the ratio between t^*_P (∼1 s) and t^*_S (∼4 s) estimated from spectral and time-domain body-wave studies (e.g., *Cormier*, 1982).

4.4 Distance variation of attenuation parameters

We estimate t^*_P and t^*_S at evenly spaced (1°) epicentral distances between $\Delta = 30°$ and $\Delta = 97°$ by solving three sets of equations. First, we relate a measurement of Δt^*_{ij} to the difference of t^* for a pair of stations i and j at epicentral distances Δ_i and Δ_j:

$$w^1_{ij}\left(t^*_{\Delta_i} - t^*_{\Delta_j}\right) = w^1_{ij}\Delta t^*_{ij}. \tag{4.6}$$

Equation (4.6) is multiplied by a factor w_{ij}^1, which is determined by the 2σ uncertainty (ε_{ij}) of the measurement of Δt_{ij}^*:

$$w_{ij}^1 = \exp\left\{-\left(\frac{\varepsilon_{ij}}{0.3}\right)^2\right\}. \tag{4.7}$$

Thus, Δt^* measurements with ε_{ij} larger than 0.3 s are weighed less than $1/e$. Second, we impose the epicentral distance variation of t^* to be smooth:

$$w_{ij}^2\left(t_{\Delta_i}^* - t_{\Delta_j}^*\right) = 0, \tag{4.8}$$

where the weight is

$$w_{ij}^2 = \exp\left\{-\left(\frac{d\Delta_{ij}}{5^\circ}\right)^2\right\}. \tag{4.9}$$

Third, we set the average value of t^* to be zero,

$$t_{30^\circ}^* + t_{31^\circ}^* + \ldots + t_{97^\circ}^* = 0, \tag{4.10}$$

since absolute values of t^* cannot be constrained from Δt^* measurements. The linear equations (4.6), (4.8), and (4.10) can be written in matrix-vector form as $\mathbf{Gm} = \mathbf{d}$, where the elements of $\mathbf{m}$ are the t^* values at the 68 epicentral distances:

$$\mathbf{m} = (t_{30^\circ}^*, t_{31^\circ}^*, \cdots, t_{97^\circ}^*). \tag{4.11}$$

We estimate $\mathbf{m}$ by least-squares inversion.

4.4.1 Global variations of t_P^* and t_S^*

Since Δt^* are measurements derived from spectral ratios, we cannot constrain the absolute values of t_P^* and t_S^*. We plot our estimates of t_P^* and t_S^* in Figure 4.4 setting $t_P^* = 0.7$ s and $t_S^* = 3.0$ s at $\Delta = 30^\circ$, as predicted by PREM, to facilitate a

comparison with predicted t^* values for the Q_μ profiles of PREM, QL6, and QLM9.

The large uncertainties and scatter in Δt^* results in wide error bars of t_P^* and t_S^*. Since the peaks and troughs are smaller than the error bounds, we emphasize only the general trend of t_P^* and t_S^*. We resolve an increase of about 0.2 s in t_P^* and about 0.7 s in t_S^* between 30°–97°. Over this distance range, the increase in t_S^* is about 4 times stronger than in t_P^*.

The PREM, QL6, and QLM9 values are calculated using equation (4.1). For QL6 and QLM9, which provide only Q_μ, we relate Q_μ to Q_P using equation (4.5) and the P- and S-wave velocities of PREM. t_P^* and t_S^* inferred from our body-wave spectra increase more slowly with epicentral distance than t_P^* and t_S^* calculated for the published profiles. For PREM, QL6, and QLM9, t_P^* increases by about 0.4 s between 30° and 97° while our data indicate an increase of about 0.2 s (Figure 4.4a). PREM and QL6, which have constant Q_μ values in the lower mantle (312 and 355, respectively) predict an increase of t_S^* of about 2.3 s and 2.0 s, respectively, between 30° and 97° (Figure 4.4b). For the same distance range, t_S^* inferred from our body-wave spectra increases by only about 0.7 s. These differences indicate that the teleseismic body-waves experience less attenuation and that body-wave spectra are explained better by Q_μ values in the lower mantle that increase with depth.

The t_P^* and t_S^* curves for model QLM9 have kinks near $\Delta = 75°$. The reduction of the slopes for distances larger than 75° is due to the increase in Q_μ at depths larger than about 2050 km (Figure 4.6). Since t_P^* and t_S^* predicted from QLM9 between about 75° and 95° are parallel to our t_P^* and t_S^* curves, the Q_μ structure of QLM9 below 2050 km depth is compatible with our body-wave spectra.

4.4.2 Pacific and circum-Pacific t_P^* and t_S^* variations

To determine whether lateral variations of attenuation in the lower mantle can be detected in our data, we analyze t_P^* and t_S^* for 'Pacific' and 'circum-Pacific' subsets of

body-wave spectra (Figure 4.5). These subsets are chosen using tomographic maps of shear velocity in the lower mantle (*Ritsema et al.*, 1999). For the Pacific subset, P- and S-wave turning points are located in the lower mantle beneath the Pacific Ocean, where shear velocities are relatively low. The circum-Pacific P- and S-waves turn in the lower mantle where the shear velocity is relatively high. Thus, we estimate whether lateral variations in t_P^* and t_S^*, as determined by P- and S-wave turning points, correlate with the large-scale shear velocity variation of the lower mantle.

We can only constrain the difference between the Pacific and circum-Pacific subsets for epicentral distances between about 70° and 85° where both the Pacific and circum Pacific subsets are sufficiently large. This distance range corresponds to P and S turning depths of 1870–2470 km (layer 2 in Figure 4.5). At distances smaller than 70°, corresponding to turning depths smaller than 1870 km (layer 1 in Figure 4.5), fewer than 5% of the P- and S-waves turn below the Pacific Ocean. Therefore, the Pacific and circum-Pacific subsets include all spectral ratios for epicentral distances smaller than 70°. For epicentral distances larger than 85°, corresponding to turning depths larger than 2470 km (layer 3 in Figure 4.5), P- and S-waves may interfere with CMB reflection phases (PcP and ScS) and render the measurements of spectral ratios inaccurate.

In Figure 4.4, variations in t_P^* and t_S^* for the complete ('global') data set are compared with variations for the Pacific and the circum-Pacific subsets. t_P^* and t_S^* values for both subsets are smaller than PREM predicted t^* values at almost all epicentral distances. Global t_P^* and t_S^* values are most similar to the circum-Pacific values because the total number of measurements for the circum-Pacific group is about four times larger than the number of measurements for the Pacific group. For $\Delta > 70°$, Pacific t_P^* (0.86 s on average) and t_S^* (3.73 s on average) are larger than the circum-Pacific t_P^* (0.85 s on average) and t_S^* (3.67 on average) values. Although averages of t_P^* (0.84 s) and t_S^* (3.65) for the global data set are similar to circum-

Pacific group t^* averages, the variation with distance is similar to the variation of the Pacific t^* within this distance range. Thus it appears that the relatively high Pacific t^* values are associated with the large low velocity anomaly beneath the Pacific Ocean. However, for Δ between 85°–92°, the Pacific t_P^* values (0.80 s on average) are smaller than the circum-Pacific group t_P^* (0.85 s on average). This may indicate that P-waves are not affected by a large low velocity province beneath the Pacific Ocean or that the P spectral ratios are contaminated by the PcP core reflection.

4.5 Radial variation of Q_μ

Given that t_P^* is lower than t_S^* by roughly a factor of four, we jointly invert the t_P^* and t_S^* for a profile of Q_μ. Q_μ in the lower mantle is parametrized using 22 layers with a uniform thickness of 100 km in which Q_μ is constant. Thus, equation (4.1) is written as

$$\sum_{n=4}^{N=25} \frac{t_n}{Q_\mu^n} = t^*, \tag{4.12}$$

where t_n and Q_μ^n are the traveltime and quality factor in the n^{th} layer of the lower mantle, respectively. Since the absolute values of t_P^* and t_S^* are unconstrained by our spectral ratios and since teleseismic body-waves propagate vertically through the upper mantle, we assume that Q_μ in the upper mantle (depth $<$ 770 km) is described by PREM:

$$\frac{Q_n^{\mathrm{PREM}}}{Q_\mu^n} = 1, \tag{4.13}$$

where Q_n^{PREM} is the Q_μ value of PREM in the n^{th} (n = 1, 2, and 3) layer of the upper mantle. Q_μ in the best-fitting profile decreases by less than 10% and only in the upper part of the lower mantle ($<$ 1270 km depth) if model QLM9, which differs most from PREM in the upper mantle, is used to constrain the upper mantle Q_μ structure.

For S-waves, we use t_S^* and compute S-wave traveltimes and ray paths using

PREM. For P-waves, we use t_P^*, compute PREM traveltimes and ray paths for P-waves, and relate Q_P to Q_μ via equation (4.5).

We impose smoothness to the Q_μ structure by penalizing differences in Q_μ for nearby layers:

$$W_{ij}\left(\frac{1}{Q_\mu^i}-\frac{1}{Q_\mu^j}\right)=0, \tag{4.14}$$

where

$$W_{ij}=\exp\left\{-\left(\frac{i-j}{5}\right)^2\right\}, \tag{4.15}$$

and i and j are layer indices. This constraint suppresses small-scale (< 150 km) depth variations of Q_μ.

We combine equations (4.12), (4.13), and (4.14) to get a matrix-vector relationship $\mathbf{Gm}=\mathbf{d}$, akin to section 4.4, where

$$\mathbf{m}=\left(\frac{1}{Q_\mu^1},\frac{1}{Q_\mu^2},\cdots,\frac{1}{Q_\mu^N}\right). \tag{4.16}$$

and estimate $\mathbf{m}$ by least squares inversion.

4.5.1 Global variation of Q_μ

The best-fitting Q_μ profile is shown in Figure 4.6 and Table 4.1. The Q_μ profiles from PREM, QL6, and QLM9 are shown for comparison. The structure of Q_μ has minima and maxima that track the maxima and minima t_P^* and t_S^*. Given the large scatter of the body-wave spectra and, consequently, the large uncertainties in t_P^* and t_S^*, we emphasize only the increasing values of Q_μ with depth as the robust model feature. Q_μ increases from 360 at the 670-km discontinuity to a maximum value of 670 just above the CMB. It increases, on average, by about 0.12 km^{-1} between 1000 and 2500 km depth in contrast to the 0.09 km^{-1} rate of increase of Q_μ in QLM9. The relatively strong increase of Q_μ is linked to the relatively modest increase of t_P^* and t_S^* compared to PREM, QL6, and QLM9 (Figure 4.4). The mean value of Q_μ model

in the lower mantle is about 520 which is 45% and 65% larger than Q_μ in QL6 and PREM, respectively.

4.5.2 Pacific and circum-Pacific Q_μ structure

Figure 4.6 shows profiles of Q_μ inferred from the complete (i.e., global) data set and the Pacific and circum-Pacific subsets as defined in section 4.4.2. The contrast between the Pacific and circum-Pacific Q_μ structure is best resolved in layer 2 (1870–2470 km depth). Here, Q_μ beneath the Pacific is 520 on average in contrast to the circum-Pacific average Q_μ value of 560. Therefore, it appears that Q_μ in the lower mantle beneath the Pacific, which is characterized by a large-scale shear-velocity reduction of 1–3%, is smaller roughly by 10% (17% at most at a depth of about 2100 km) than in the circum-Pacific region.

4.6 Discussion and Conclusions

In this paper we have applied a multi-taper analysis to examine nearly 300,000 ratios of broadband P- and S-wave spectra. We determine the P-wave and S-wave body-wave attenuation parameters t^*_P and t^*_S and a radial profile of Q_μ for the lower mantle. Despite significant measurement scatter we observe that t^*_P and t^*_S increase by about 0.2 s and 0.7 s, respectively, between epicentral distances of 30° and 97°. The t^*_P increase of 0.2 s is comparable to the difference in spatial t^*_P of 0.2 s between tectonically active western North America and stable eastern North America (*Hwang et al.*, 2009). Thus, the dependence on distance cannot be neglected when estimating spatial variations of t^*_P and t^*_S.

The t^*_S/t^*_P ratio is about 4, which is consistent with the common observation that attenuation in the bulk modulus is negligible compared to attenuation in the shear modulus since attenuation occurs mostly in shear (e.g. *Anderson and Given*, 1982). It is also consistent with the ratio between t^*_P (∼1 s) and t^*_S (∼4 s) estimated from

spectral and time-domain body-wave studies (see the review by *Cormier* (1982)).

The increase of t_P^* and t_S^* with distance is smaller than predicted by profiles of Q_μ derived from normal-mode data. This implies that the quality factor Q_μ in the lower mantle is not constant (as in PREM and QL6) or decreasing (as in PAR3P, QM1, or in *Resovsky et al.* (2005)) for body-waves at a period of about 1 s. Rather, it can only be explained if Q_μ increases with depth with a rate of about 0.12 km^{-1}. The increase is 40% larger than in model QLM9, which is derived from long-period S and ScS waveforms, although the gradient of Q_μ in QLM9 in the lowermost 1000 km of the mantle is consistent with our data.

Since Q_μ in the upper mantle cannot be constrained from our Δt^* measurements, we assume PREM's Q_μ structure for the upper mantle. Under this assumption, Q_μ is, on average, 516 in the lower mantle. which is larger than Q_μ in PREM and QL6 by about a factor of 1.5. Frequency-dependence of Q_μ in the form of $Q = Q_0\ \omega^\alpha$ can explain the difference between the PREM Q_μ value (312 in the lower mantle) and the average Q_μ value (516) constrained here if $\alpha \approx 0.1$, which is within the range of values obtained theoretically (e.g. *Minster and Anderson*, 1981) and from seismological observations (e.g. *Smith and Dahlen*, 1981; *Anderson and Given*, 1982; *Shito et al.*, 2004; *Lekić et al.*, 2009).

We estimate Q_P and Q_μ models separately by using, respectively, P-wave and S-wave data to determine the Q_P/Q_μ ratio for our data and investigate the effect of finite Q_κ. The Q_P/Q_μ ratio for our Q_P and Q_μ models in the lower mantle is about 2.27 on average. This ratio is almost the same as the Q_P/Q_μ of 2.25 when $Q_\kappa^{-1} = 0$ is assumed. This shows that our individual Q_P and Q_μ estimates are reasonable because intrinsic seismic attenuation occurs mostly in shear and the bulk attenuation in negligible, i.e., $Q_\mu \ll Q_\kappa$ (*Anderson and Given*, 1982).

Roth et al. (1999) suggested that the loss in bulk can be as high as one third of the loss in shear which is equivalent to Q_P/Q_μ ratio as low as 1.75. In order to investigate

the effect of a finite Q_κ value, we invert for Q_μ using equation (4.4) and a Q_P/Q_μ ratio of 1.75. This results in a Q_μ decrease of about 15% between 670–1500 km depth but Q_μ decreases by less than 5% in the lower half of the mantle (> 1500 km depth). In addition, the increase of Q_μ with depth remains evident. When only P-waves are used to invert for radial Q_P model, our Q_P increases from about 820 at 670 km depth to its maximum value of about 1450 at 2700 km depth. The mean value of our Q_P in the lower mantle is about 1110. This is about 40% larger than the average Q_P in the lower mantle in PREM (about 780) but about 60% smaller than the Q_P value in the lower mantle (about 2600) according to *Warren and Shearer* (2000) which is measured at relatively high frequencies between 0.16 – 0.86 Hz.

We have explored whether lateral variations in t_P^*, t_S^* and Q_μ are resolvable by dividing the data set in two subsets that are defined by tomographic maps of shear velocity. The Pacific subset includes body-wave spectra associated with P- and S-wave turning points in the lower mantle beneath the Pacific Ocean, where shear velocities are relatively low. The circum-Pacific subset includes body-wave spectra with P- and S-waves that turn in higher-than-average shear velocity regions of the lower mantle. Between epicentral distance of 70° and 85°, when the measurements are most abundant, t_P^* and t_S^* for the Pacific subset is larger than for the circum-Pacific subset.

Q_μ beneath the Pacific is, on average, 520 between 1870 and 2470 km depth. In contrast, Q_μ determined for the circum-Pacific data is, on average, 560 between 1870 and 2470 km depth, similar to what is resolved for the complete data set. Therefore, we find that Q_μ is reduced within the large-scale low-velocity province of the lower mantle beneath the Pacific. If this difference is representative of the large-scale variations of Q_μ in the lower mantle, we place an upper limit to Q_μ variations of about 17%. Due to the interference of P and S and the core-reflections PcP and ScS, t_P^* and t_S^* for distances larger than 85° may be inaccurate. Consequently, Q_μ

cannot be constrained for depths larger than about 2500 km, including the D'' layer.

4.7 Acknowledgments

This research has been funded by NSF grant EAR–0944167. Data have been provided by the IRIS/DMD and the Geoscope Data Center. Figures have been produced using the GMT software of (*Wessel and Smith*, 1995). We thank the reviewers for constructive reviews.

Depth (km)	Q_μ	Depth (km)	Q_μ
770	356	1820	486
820	386	1920	504
920	449	2020	526
1020	471	2120	561
1120	437	2220	585
1220	451	2320	616
1320	464	2420	631
1420	495	2520	655
1520	507	2620	653
1620	495	2720	671
1720	476	2820	610

Table 4.1: The profile of the best-fitting Q_μ model as a function of depth (km).

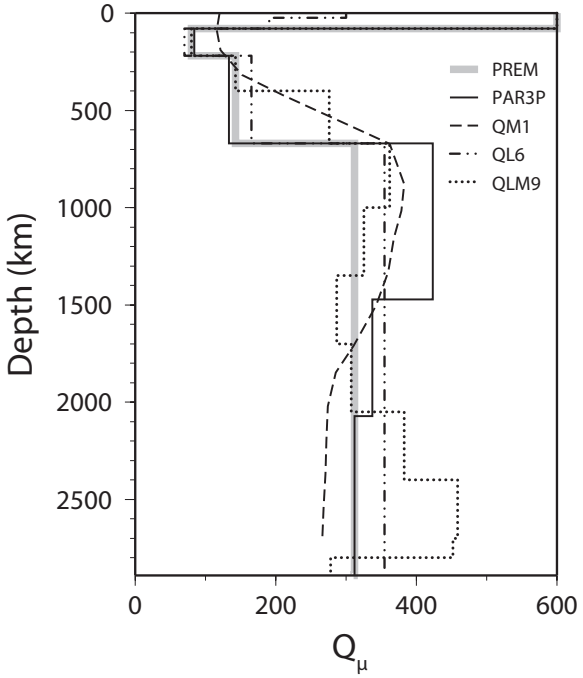

Figure 4.1: Radial Q_μ structures of (thick grey line) PREM (*Dziewonski and Anderson*, 1981), (solid black line) PAR3P (*Okal and Jo*, 1990), (dashed line) QM1 (*Widmer et al.*, 1991), (two-dot chain line) QL6 (*Durek and Ekström*, 1996), and (dashed dotted) QLM9 (*Lawrence and Wysession*, 2006a).

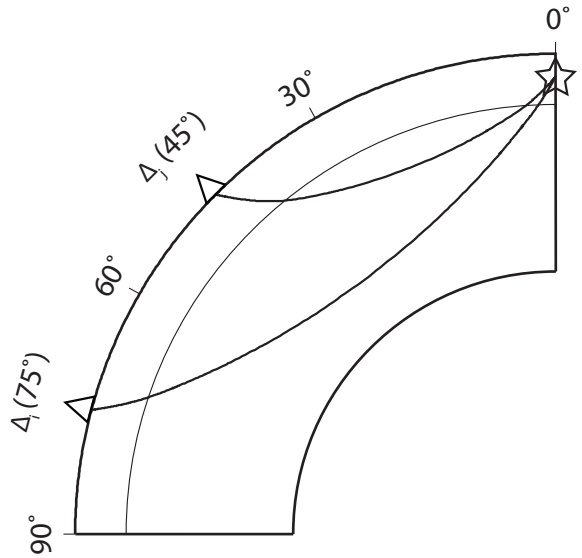

Figure 4.2: Geometrical ray paths of P-waves from a (star) 300-km deep earthquake source to (triangles) stations at epicentral distances of $\Delta = 45°$ and $\Delta = 75°$.

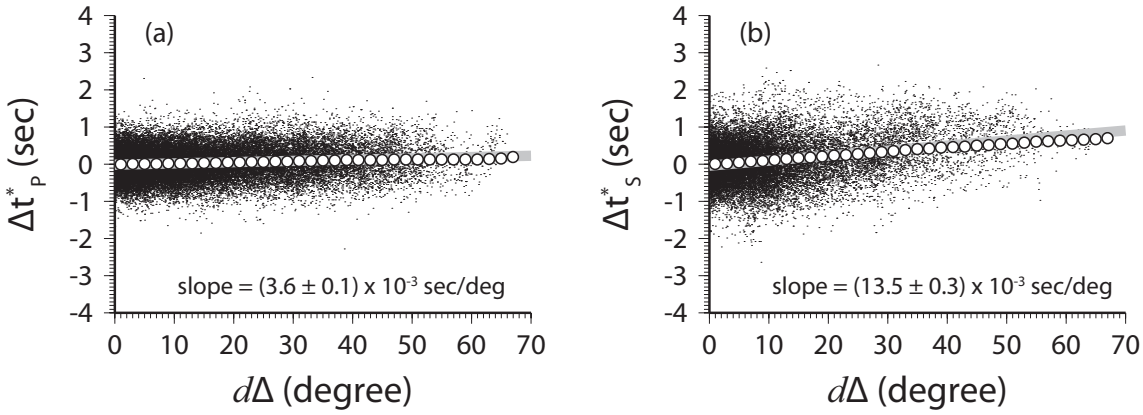

Figure 4.3: (a) Δt^*_P and (b) Δt^*_S as a function of inter-station distance $d\Delta_{ij}$ ($= |\Delta_i - \Delta_j|$). Thick grey lines are best-fitting lines to the entire Δt^*_P and Δt^*_S data sets. Their slopes and 95% confidence ranges are indicated at the bottom. Circles are mean (a) Δt^*_P and (b) Δt^*_S values predicted from the epicentral variations of t^*_P and t^*_S for the global data, respectively in Figures 4.4a and 4.4b.

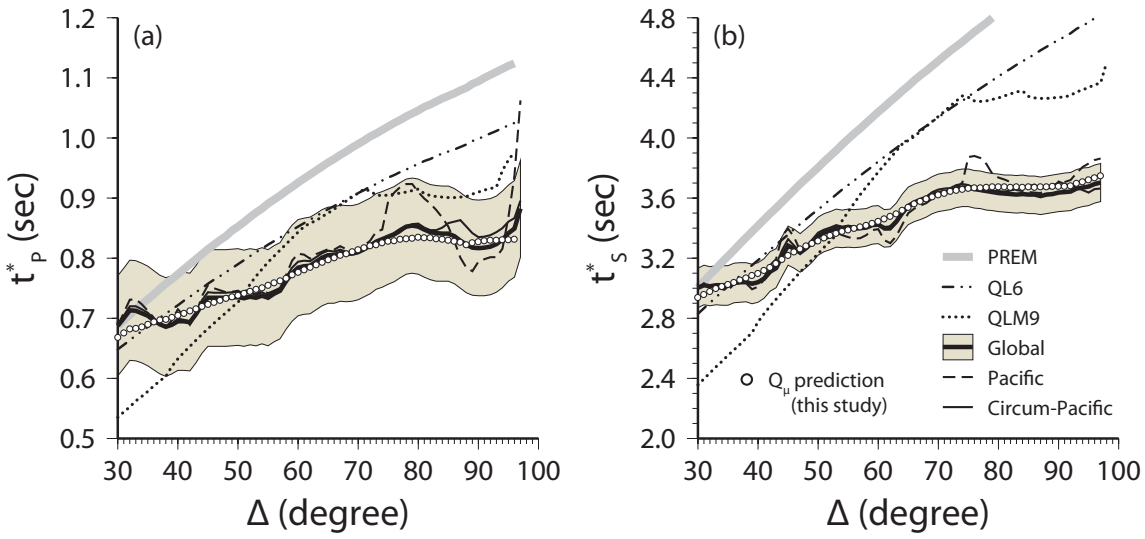

Figure 4.4: Epicentral distance variations of (a) t^*_P and (b) t^*_S for the complete (global) data set (thick black lines) with their errors (shaded area), for the Pacific subset (dashed lines), and the circum-Pacific subset (thin black lines) at distances between 30° and 97°. Errors are determined from the uncertainties in the Δt^* measurements. t^* variations calculated from PREM (thick grey lines), QL6 (two-dot chain lines), and QLM9 (dashed dotted lines) at distances between 30° and 97° are plotted for comparison. t^*_P of PREM, QL6, and QLM9 are computed using Q_P structures converted from Q_μ profiles of PREM, QL6, and QLM9 using equation (4.5). Also shown are (a) t^*_P and (b) t^*_S variations predicted from our global Q_P and Q_μ models (white circles).

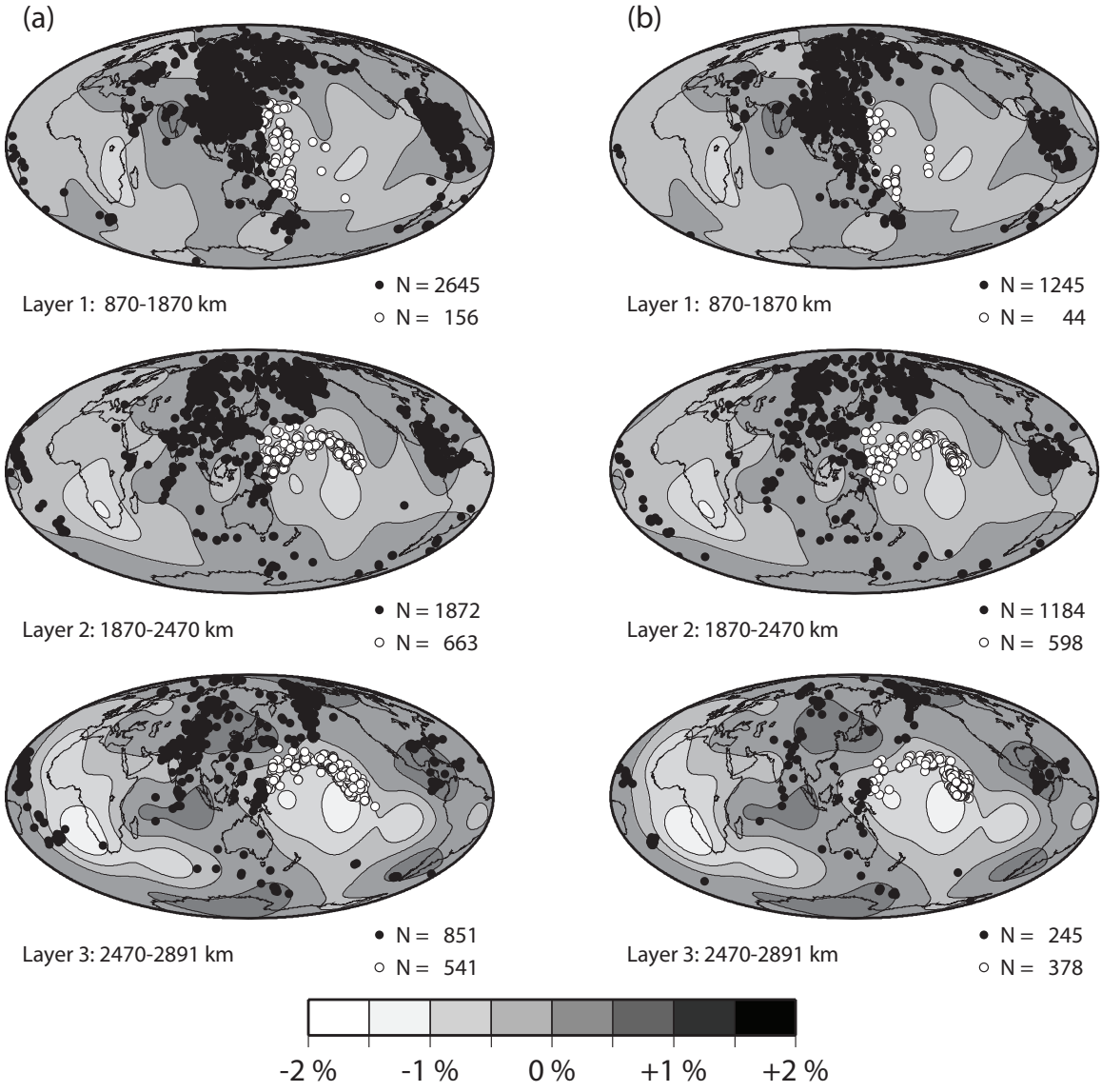

Figure 4.5: Turning points of (a) P- and (b) S-waves used in this study within (top) Layer 1 (870–1870 km), (middle) Layer 2 (1870–2470 km), and (bottom) Layer 3 (2470–2891 km). The number of turning points for the Pacific group (white circles) and the circum-Pacific group (black circles) groups are indicated below the maps. The background represents the shear velocity variation (plotted up to degree 8) at depths of 1500 km, 2100 km, and 2700 km according to S20RTS (*Ritsema et al.*, 1999).

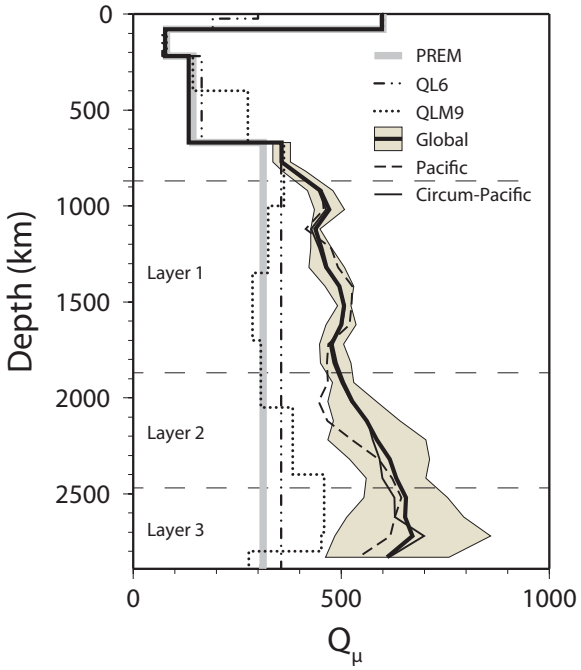

Figure 4.6: Radial variation of Q_μ for complete (Global) data (thick black lines) with its error (shaded area), the Pacific group (dashed lines), and the circum-Pacific group (thin black lines), which are compared with Q_μ profiles from PREM (thick gray lines), QL6 (two-dot chain lines), and QLM9 (dashed dotted lines). Horizontal dashed lines represent the boundaries between Layer 1, Layer 2, and Layer 3.

CHAPTER V

Wave front healing renders deep plumes seismically invisible

5.1 Abstract

Since W. J. *Morgan* (1971) proposed that intra-plate volcanism at hotspots is caused by hot plumes rising from the lower mantle, geophysicists have been actively pursuing physical evidence for mantle plumes. Several seismic studies have mapped low-velocity anomalies below a number of hotspots. However, the association of low-velocity structures with plume tails has remained controversial given the debate on whether lower-mantle plumes impart observable travel-time or amplitude perturbations on seismic waves. Using high-resolution numerical simulations of plume ascent through the mantle and their effects on waveforms, we demonstrate that the delay of shear waves by plume tails at depths larger than 1000 km are immeasurably small (< 0.2 s) at seismic periods commonly used in waveform analysis.

This chapter has been accepted for publication in Hwang, Y. K., J. Ritsema, P. E. van Keken, S. Goes, and E. Styles (2011), Wave front healing renders deep plumes seismically invisible, *Geophys. J. Int.*

5.2 Introduction

A hotspot is a long-term source of volcanism unexplained by plate boundary processes. Many hotspots are characterized by topographic swells, a relatively fixed mantle-source position leading to volcanic lines with a systematic age progression and distinct radiogenic isotope characteristics. Although mid-plate volcanism in some regions may have a shallow mantle origin (*King and Ritsema*, 2000; *Foulger et al.*, 2005), geochemical and geophysical observations link a large number of hotspots to narrow upwellings from the deep mantle (*Farley and Neroda*, 1998; *Ito and van Keken*, 2007). Plumes may have a profound effect on the geologic landscape. They have been implicated in the initiation of continental break-up and massive flood basalt eruptions that trigger climate changes and mass extinctions (*Richards et al.*, 1989; *Hawkesworth et al.*, 1999).

Numerical and experimental simulations of mantle convection demonstrate that thermal plumes develop from instabilities that naturally arise in thermal boundary layers such as the core-mantle boundary. Plume morphology in a convecting mantle with chemical and phase changes and non-linear rheology may be complex (*van Keken*, 1997; *Steinberger and O'Connell*, 1998; *Farnetani and Samuel*, 2003). However, most simulations show that a plume is characterized by a large 'head' that rises rapidly in the mantle while connected to the boundary layer via a relatively narrow 'tail' (*Ribe et al.*, 2007).

Wide-spread acceptance of plumes in Earth's mantle is contingent on an undisputed seismic detection. A number of regional-scale seismic studies suggest the presence of sharp cylindrical velocity anomalies below the lithosphere that cause travel-time delays (*Nataf and VanDecar*, 1993) and wave diffraction (*Ji and Nataf*, 1998). In addition, several hotspots are directly above lower-than-average seismic velocities in the upper mantle (*Wolfe et al.*, 1997; *Ritsema and Allen*, 2003) and mid mantle (*Montelli et al.*, 2004; *Wolfe et al.*, 2009), topographic variations of the 410-km and

660-km discontinuities (*Shen et al.*, 1998) and ultra-low-velocity-zones (*Helmberger et al.*, 1998) and broad low-shear-velocity regions (*Dziewonski et al.*, 2010) at the base of the mantle.

It remains questionable whether these seismic observations can be uniquely linked to plumes. Dynamic plume models that are consistent with the surface observations predict tails that are narrower than 100–200 km in the upper mantle. Under the influence of increasing viscosity and thermal conductivity and decreasing expansivity with depth (*van Keken and Gable*, 1995; *Goes et al.*, 2004), plumes may have widths of up to 1000 km in the lower mantle. However, associated wave speed reductions are expected to be less than a percent. Hence, their impact on traversing waves may be minimal. In this study, we investigate whether dynamically predicted plume structures can be detected seismically by simulating 3D wave propagation through a set of high-resolution numerical plume models.

5.3 Plume simulations

We simulate plumes by solving the coupled Stokes and energy equations for thermally-driven convection with modifications for the effects of compressibility and phase changes. The governing equations are based on the conservation of mass, momentum, and energy under the anelastic liquid approximation (*King et al.*, 2010). These models are similar in design to those described in *Leng and Zhong* (2010). The numerical simulations employ a high-resolution axisymmetric spherical shell geometry (*Lin and van Keken*, 2006), This geometry preserves the 3D nature of vertically rising plumes in a spherical Earth and enables us to reproduce Earth-like convective vigour and to simulate plumes with a spatial resolution of a few kilometers near the plume axis.

The chosen models comprise a wide range of possible plume structures (Figure 5.1). They include depth-dependent thermal expansivity and diffusivity, where ex-

pansivity decreases from top to bottom by a factor of 8 and diffusivity increases by a factor of 4 following *van Keken* (2001). The viscosity increases by a factor of 30 below the 670-km phase transition. The temperature contrast in the plume is 375 K and we assume that this causes a 200 times reduction in viscosity. The Rayleigh number (based on the background viscosity of the lower mantle and surface values of diffusivity and expansivity) is 1.52×10^6. The initial condition is based on a thermal boundary layer with 100 km initial thickness and a small perturbation at the plume axis.

Under these conditions, the plume rises through the lower mantle in approximately 30 Myr. The plume flow through the 670-km boundary is somewhat episodic even without the effects of phase transitions, but it reaches a nearly steady-state structure after approximately 80 Myr. In an early phase (P0h), the head is transiting and thinning in the upper-mantle. In a later quasi-steady-state phase (P0s), the plume has narrow upper and lower mantle tails and its head has spread laterally in the uppermost mantle.

Plumes P2s and P4s are quasi steady-state stages of plumes where penetration into the upper mantle is partially (P2s) or completely (P4s) impeded. P2s and P4s have the same parameters as P0h and P0s, except for included phase boundaries at 410 and 670 km depth. For the 410-km boundary, we assume an exothermic phase boundary with a constant Clapeyron slope of +3 MPa/K. For the 670-km boundary, we use an endothermic phase boundary with a Clapeyron slopes of -2 MPa/K and -4 MPa/K for P2s and P4s, respectively. Plume P2s penetrates into the upper mantle but a portion of the original plume head remains in the uppermost lower mantle surrounding the plume conduit. For P4s, the phase boundary is sufficiently strong to force the plume to remain in the lower mantle, without an attendant surface expression.

Although the model dynamics assume strictly thermal plumes, we investigate the effects of entrainment of compositionally and seismically distinct material (*Cobden*

et al., 2009) from the lowermost mantle in model P0s^{M} and P0s^{P}. We assume that the anomalous components are confined to the plume cores, where temperatures are at least half of the maximum value at the plume axis. Two dense end members are tested. The core of model P0s^{M} has a basaltic composition representative of recycled oceanic crust (*Perrillat et al.*, 2006). Model P0s^{P} has a core with an iron and silica-rich primitive mantle composition (*Anderson*, 1989). These dense chemical components will enhance the time-dependence of plume dynamics, including repeated head-like pulses and variable tail widths (*Lin and van Keken*, 2006; *Farnetani and Samuel*, 2005).

To map the thermal perturbations into seismic velocity anomalies, we calculate phase equilibria, density, and elastic parameters as a function of temperature, pressure, and composition using the thermodynamic method of *Connolly* (2005). We assume an isochemical pyrolitic composition (*Sun*, 1982) and make a correction for the effects of anelasticity using a model with an Arrhenius temperature-pressure dependence (*Goes et al.*, 2004; *Cammarano et al.*, 2003). The procedure and uncertainties have been described in detail by *Cobden et al.* (2008, 2009). The mineral parameters and equation of state are from the 'sfo05' compilation for the CFMAS system (*Stixrude and Lithgow-Bertelloni*, 2005; *Khan et al.*, 2008).

5.4 Waveform simulations

We use the SHaxi method (*Jahnke et al.*, 2008) to simulate the full 3D shear-wave (SH) motions in an axisymmetric shear-velocity model. The waveform computation is performed on a 2D grid of shear-velocity variation and virtually expanded to 3D spherical geometry by rotating the grid around the radial axis passing through the plume axis and the earthquake hypocenter (Figure 5.2). The shear-velocity anomalies associated with the plumes are assumed to be anomalies relative to the velocity structure in PREM.

Since the earthquake is at the antipode, we analyze the major-arc SSS phase (denoted as SSS_M) at angular distances D from the plume axis between 0° and 40° (i.e. epicentral distances between 180° and 220°). These waves have similar slownesses and cross the plume axis at the same depths Z as direct S waves at epicentral distances between 60° and 75°. By placing the earthquake at a depth of 1000 km, we minimize interference with other teleseismic phases. To determine the effects of plumes on shear-waves, we compare the 3D waveforms with the waveforms for PREM. The delay time of SSS_M, due to the presence of a plume in the mantle, is defined by the cross-correlation of plume and PREM synthetics.

Figure 5.3 compares a selection of SHaxi seismograms for angular distances D between 1.5° and 9.5° computed for PREM and a model that includes the shear-velocity perturbations of P0h. In this case (and for all other plumes), it is evident that SSS_M is delayed with respect to PREM when it propagates through the plume. This delay decreases with increasing D. When D is less than 3°, delay times are larger than 5 s but they diminish rapidly to 0.2 s when D is approximately 10°.

5.5 Results and conclusions

Figure 5.4 illustrates that the SSS_M travel-time delays depend on the morphology and shear-velocity structure of the plumes. All plumes, except P4s, have heads in the upper mantle that are wider than 1000 km. For those models with upper mantle plume heads, SSS_M propagates through the head when $D < 5°$ and is delayed by 6–12 s. Plumes P0s, $P0s^M$ and $P0s^P$ have similar shapes but the strength of their velocity anomalies differ near the plume axes and within the plume heads (compare Figure 5.1b, 5.1e, and 5.1f). The differences in internal velocity structures of plumes result in delay differences of several seconds when $D < 5°$ (compare Figure 5.4b, 5.4e, and 5.4f). As soon as SSS_M propagates only through the plume tail, its delay decreases with increasing D and increasing Z'. Plume P4s has a head below the 670-km phase

transition. When SSS_M does not propagate through this head for D larger than 10°, its delay diminishes also. Thus, for all plumes, we find that SSS_M delay times are smaller than 0.2 s at distances larger than 10° when SSS_M traverses the plume tail at a depth larger than about 1000 km.

The decay of the delay time with increasing D is well understood theoretically by an effect commonly referred to as 'wavefront healing' (*Wielandt*, 1987). Just after traversing the plume tail in the lower mantle, SSS_M may be delayed by about 4 s. After the deceleration of the wavefront during its propagation through the plume, the indentation of the wavefront disappears due to diffraction. Consequently, the wave travel-time delay decreases exponentially with increasing propagation length L between the SSS_M crossing point on the plume axis and the seismic station on the surface. L is about 1500 km when D is 10°, or, equivalently, when SSS_M crosses the plume axis at a depth Z of about 1000 km. A propagation distance L of 1500 km is sufficiently long for complete wavefront healing and, thus, for shear-wave delay times of 4 s just behind the lower mantle plume axis to diminish to immeasurably small values at the surface.

Delay times of teleseismic body-waves are the primary data for (tomographic) mapping of wave speed heterogeneity in the mantle. The signals of most seismic phases have emergent onsets or onsets hidden in the waveform coda of previously recorded phases. Hence, it is common practice to measure the delay times by waveform correlation akin to the procedure used in this paper. Typical measurement uncertainties exceed 0.5 s due to noise, waveform variability, uncertainties in earthquake location and origin time, and the poorly constrained effects of anisotropy and the heterogeneous crust on waveforms. Therefore, maximum delay times of 0.2 s due to plume tails in the lower mantle cannot be detected. While broad shear-velocity anomalies in the lowermost mantle are robust structures, lower mantle plumes cannot be resolved with seismic data.

5.6 Acknowledgments

We thank Michael Thorne for providing us with the code SHaxi for wave simulation and James O'Connolly for making the code PerPleX for velocity conversions available. This research has been funded by NSF grant EAR-0855487 and a STFC postgraduate studentship (ES).

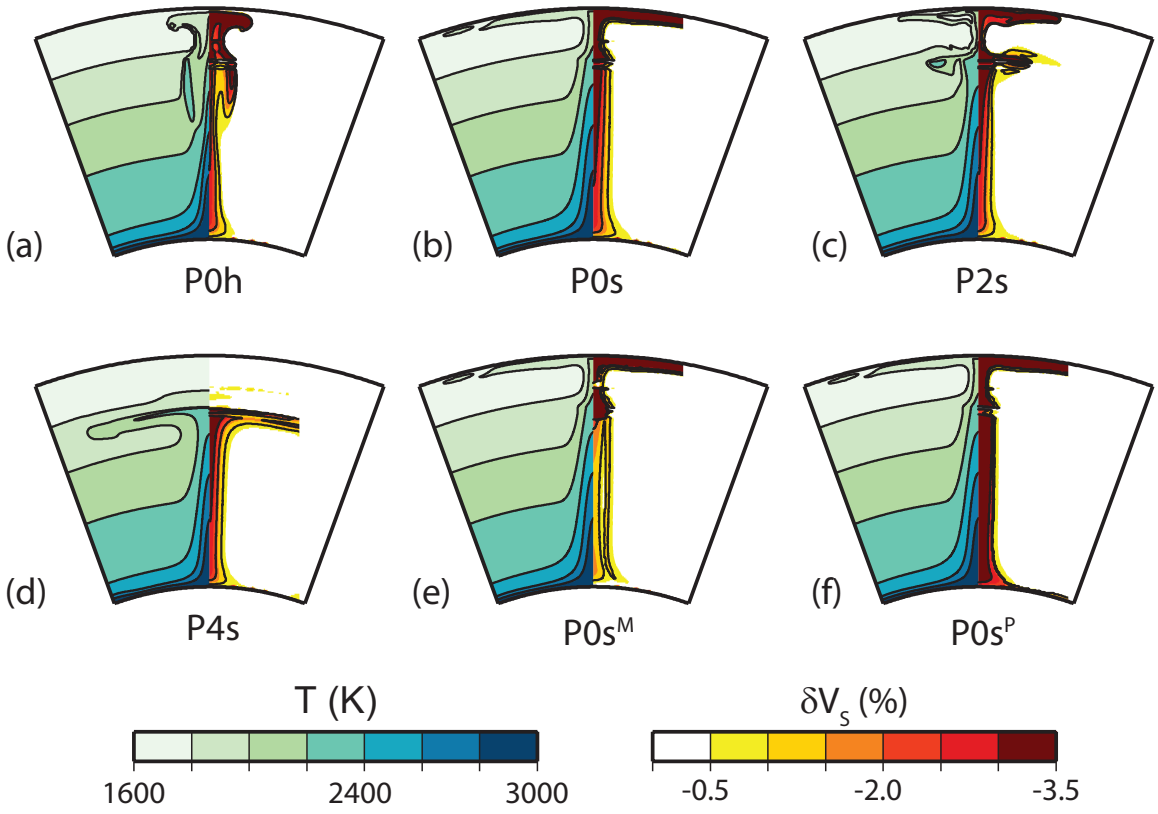

Figure 5.1: Absolute temperature structures (left half) and shear-velocity perturbations (right half) of plume models (a) P0h, (b) P0s, (c) P2s, (d) P4s, (e) $P0s^{M}$, and (f) $P0s^{P}$. Temperature (T) structures are in Kelvin (K) and shear-velocity anomalies (δV_S) are relative to PREM. The cross-sections are 40 degrees wide and encompass the entire mantle.

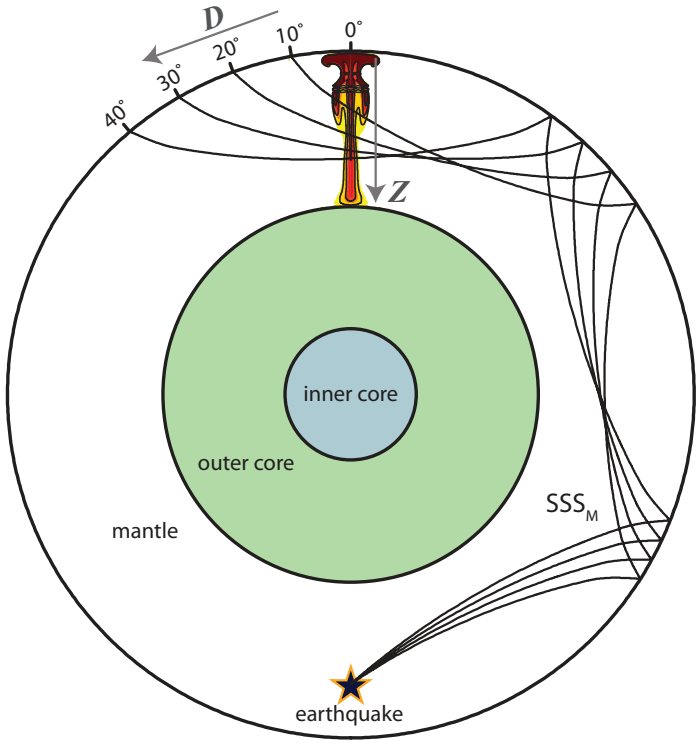

Figure 5.2: Plume P0s is shown as shear-velocity perturbations with respect to PREM. The earthquake (star) is at 1000 km depth and located at the antipode of the plume. The solid curved lines are four geometric ray paths of SSS_M for epicentral distances of 190°, 200°, 210°, and 220°, which correspond to angular distances D from the plume axis of 10°, 20°, 30°, and 40°, respectively. The ray geometric crossing depths Z at the plume axis for these distances are 1077 km, 1563 km, 1857 km, and 1989 km, respectively.

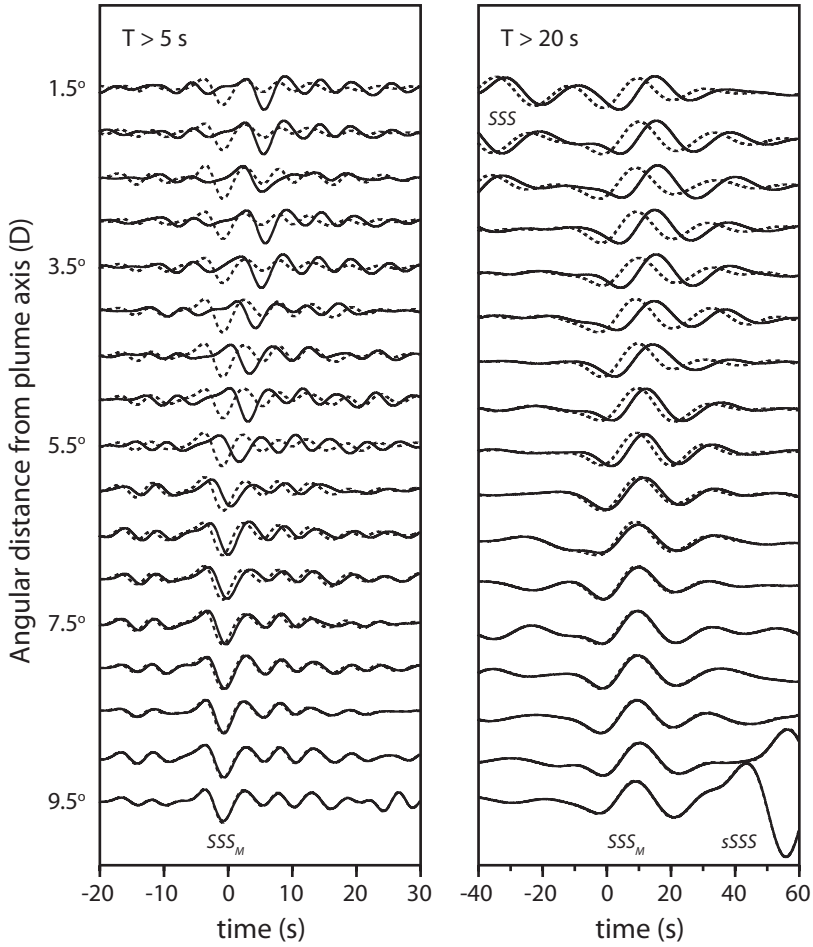

Figure 5.3: Waveforms (left) for periods longer than 5 s and (right) for periods longer than 20 s of SSS_M (aligned at time 0) between distances $D = 1.5°$ and 9.5° for models PREM (dashed line) and model P0s (solid line). The labels SSS and sSSS indicate the arrival of the minor-arc SSS and its surface reflection within the time window around SSS_M.

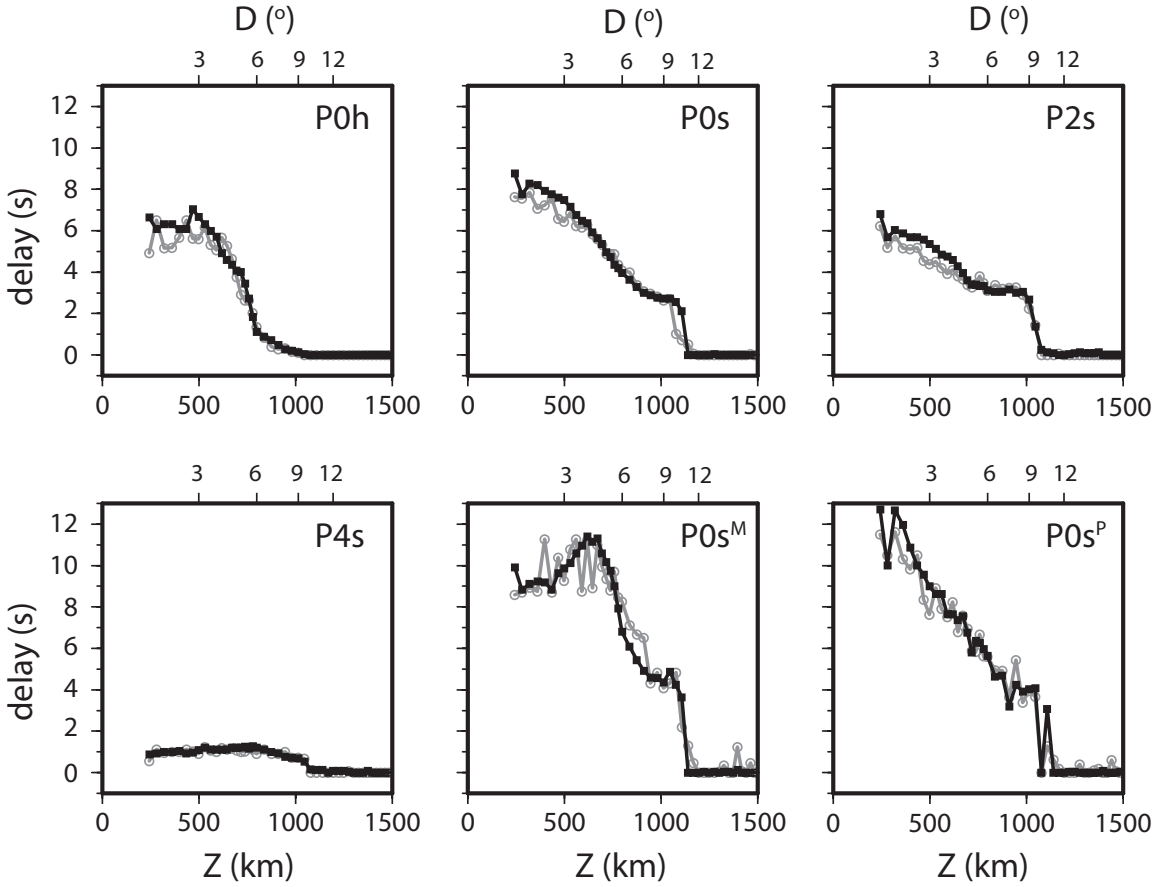

Figure 5.4: Travel-time delays as a function of the angular distance D from the plume axis (upper x-axis) and as a function of plume tail crossing depth Z (lower x-axis) for plumes (a) P0h, (b) P0s, (c) P2s, (d) P4s, (e) $\mathrm{P0s^M}$, and (f) $\mathrm{P0s^P}$. The travel-time delays measured at periods longer than 5 s and longer than 20 s are indicated by black squares and grey circles, respectively.

CHAPTER VI

Conclusions

In this thesis, spatial maps of body-wave attenuation parameters t_P^* and t_S^* are derived from teleseismic P-wave and S-wave spectra of deep earthquakes. The ratios of these body-wave spectra are also inverted for the epicentral distance variations of t_P^* and t_S^* in teleseismic distance. Finally, the distance variations of t_P^* and t_S^* are jointly inverted for a radial profile of Q_μ that is globally averaged for the lower mantle.

Nearly 300,000 measurements from about two-decade long collection of digital waveforms recorded at about 900 broadband seismic stations in regional and global networks are used to measure body-wave t^* and Q. This large data set provides more densely distributed and better constrained information on uppermost mantle t^* below the continent and the global Q profile with higher resolution in the lower mantle than has been previously available.

The variations in t_P^* and t_S^* maps, constrained respectively from P-wave and S-wave spectra, exhibit highly similar patterns. Moreover, the ratio of t_P^* and t_S^* variances ($\sim$4 s) is consistent with the t_S^*/t_P^* ratio of 4.5 predicted by the Q structure of PREM (*Dziewonski and Anderson*, 1981) and the conventional t_S^*/t_P^* ratio of 3.5 (e.g., *Cormier*, 1982). This indicates that the primary cause of t_P^* and t_S^* variations constrained in this thesis is the intrinsic attenuation in the upper mantle.

The global distribution of t_S^* derived by joint inversion of P-wave and S-wave

spectra exhibits the patterns that reflect global tectonics on the scale of around 200–500 km. t_S^* values are relatively higher in the uppermost mantle beneath tectonically active collision zones, rift zones, and back-arc regions while it is characterized by lower t_S^* values beneath stable continental cores. For example, t_S^* is relatively high in the tectonically-active western North America and low in the platforms of central and eastern North America. t_S^* is higher in western Europe than in the Baltic shield region. t_S^* is higher at stations within the western and southern cratons of Africa and lower in the East African Rift region. The back-arc regions of the western Pacific subduction zones are characterized by low t_S^* in general. These features are not only coherent with variations of body-wave t^* that are previously obtained (e.g., *Sheehan and Solomon*, 1992; *Bhattacharyya et al.*, 1996; *Roth et al.*, 1999, 2000; *Reid et al.*, 2001; *Warren and Shearer*, 2002; *Lawrence et al.*, 2006; *Lawrence and Wysession*, 2006a,b) but also presented with higher resolution than other studies. The consistency between patterns in t^* maps and tectonics suggests that the observed variations in t^* reflect the intrinsic attenuation in the upper mantle.

The t_S^* map derived from body-wave spectra in this thesis is compared to the maps of (1) t_Q^*, the attenuation map computed from the most recent surface-wave Q tomography model QRFSI12 (*Dalton et al.*, 2008), and (2) t_T^*, the attenuation map inferred from the thermal interpretation (*Goes et al.*, 2005) of shear-velocity tomography S20RTS (*Ritsema et al.*, 1999). First, the global attenuation model QRFSI12 is based on Rayleigh waves which samples the upper mantle in a fundamentally different manner than body-waves. Thus, the correlation between t_S^* and t_Q^* maps indicates that both the body-wave spectra and surface-wave amplitudes are affected by the same attenuation variation in the upper few hundred kilometers of the mantle even though the wavelengths and propagation directions of surface-waves and body-waves are entirely different. This highly similar patterns shown in t_S^* and t_Q^* maps also illustrate that consistent variations in attenuation can be constrained from large data sets

of horizontally and vertically propagating waves. The coherence between t^* variations obtained in this thesis and in previous studies using surface-wave (e.g., *Romanowicz*, 1995; *Billien et al.*, 2000; *Romanowicz and Gung*, 2002; *Selby and Woodhouse*, 2002; *Gung and Romanowicz*, 2004; *Dalton and Ekström*, 2006; *Dalton et al.*, 2008) confirms this further. Second, the spatial variation in t_S^* is also similar to variations in the predicted t_T^* and thermal structure of the upper mantle that are inferred from shear-velocity anomalies. This confirms that the variations in seismic velocity in the upper mantle are largely affected by temperature effect with a strong attenuation signature. This thesis clearly illustrates the coherence between variations in body-wave t^*, tectonics, surface heat flow, surface-wave t_Q^*, and thermally interpreted t_T^* from shear-velocity anomalies. This suggests that temperature is the predominant control of attenuation and velocity structures in the uppermost mantle. This conclusion is also consistent with other previous studies (*Artemieva et al.*, 2004; *Dalton et al.*, 2009; *Dalton and Faul*, 2010).

While temperature is the main cause of the patterns in t^*, other factors such as the presence of melt below mid-ocean ridges and a melt-depleted composition of cratonic roots likely have additional influence (*Artemieva et al.*, 2004; *Dalton et al.*, 2009; *Dalton and Faul*, 2010). The high t_S^* and t_Q^* anomalies in back-arc regions that coincide with low shear-velocities may partially reflect high water content. It is required to image t^* variations in the uppermost mantle with higher resolutions compatible with models of surface-wave Q and shear-wave velocity in order to better distinguish between different mechanisms that control variations in attenuation and velocity.

Between epicentral distances of 30° and 97°, the increases of 0.2 s in t_P^* and 0.7 s in t_S^* are observed in this thesis although significant scatter exhibits in measurement data. The relatively strong increase of t_S^* ($t_S^* \approx 4\,t_P^*$) suggests that intrinsic shear attenuation is the cause of the overall trend in our data. The amplitudes of the

increases in t_P^* and t_S^* are comparable to the spatial t^* contrasts between regional maxima and minima of t^* in North America and Europe. Thus, the dependence on distance should not be neglected when one estimates spatial variations of t_P^* and t_S^*.

Depth-dependent Q_P and Q_μ models are separately estimated from the epicentral distance variations in t_P^* and t_S^*, respectively, and the ratios of Q_P/Q_μ are determined to investigate the effect of the absorption in bulk (Q_κ^{-1}). The Q_P/Q_μ ratio of 2.27 (on average) determined by body-wave spectra is almost the same as the theoretical Q_P/Q_μ ratio of $\sim$2.25 when $Q_\kappa^{-1} = 0$ is assumed. This confirms that intrinsic attenuation occurs mostly in shear and the bulk attenuation in negligible in the mantle, i.e., $Q_\mu^{-1} \gg Q_\kappa^{-1}$ (*Anderson and Given*, 1982).

Epicentral distance variations in t_P^* and t_S^* are inverted for Q_μ in the lower mantle. The increases in body-wave t^* observed in this thesis are explained best if Q_μ increases with depth with a rate of about 0.12 km^{-1} in the lower mantle with an average Q_μ value of 516. However, this rate of Q_μ increase with depth is much faster than previously determined Q_μ profiles that are constant (*Dziewonski and Anderson*, 1981; *Durek and Ekström*, 1996), slightly increasing (*Lawrence and Wysession*, 2006a), or slightly decreasing (*Okal and Jo*, 1990; *Widmer et al.*, 1991) in the lower mantle. The high Q_μ value (516 on average in the lower mantle) estimated from body-wave spectra (up to 0.8 Hz) in this thesis can be reconciled with previously estimated Q_μ values by the frequency-dependence form of $Q = Q_0\ \omega^\alpha$ when $\alpha \approx 0.1$, which is within the range of α values obtained theoretically (e.g. *Minster and Anderson*, 1981) and from seismological observations (e.g. *Smith and Dahlen*, 1981; *Anderson and Given*, 1982; *Shito et al.*, 2004; *Lekić et al.*, 2009).

APPENDICES

APPENDIX A

Spatial t_S^* values for global stations

Table A.1: t_S^* values for globally distributed stations (Figure 3.3a).

Station	LAT °	LON °	t^* (s)	Station	LAT °	LON °	t^* (s)
A05	60.22	-123.37	-1.08	AAK	42.64	74.49	0.03
AAM	42.30	-83.66	-0.05	ABER	56.63	-3.92	0.34
ABKT	37.93	58.12	-0.30	ACCN	43.38	-73.67	0.57
ACKN	64.99	-110.87	-0.02	ACSO	40.23	-82.98	-0.39
ADK	51.88	-176.68	-0.19	AFIF	23.93	43.04	0.05
AGBLF	33.40	-81.76	-0.95	AGIN	38.94	38.71	0.08
AHID	42.77	-111.10	0.05	AHLT	38.75	42.48	0.39
AKSU	41.14	80.11	0.26	AKT	50.43	58.02	-0.24
ALE	82.50	-62.35	0.48	ALLY	41.65	-80.14	-0.59
ALTA	58.29	-4.41	0.05	AML	42.13	73.69	0.04
ANA	42.78	77.66	0.67	AND	64.33	-149.20	0.11
ANMO	34.95	-106.46	0.30	ANPB	25.19	121.52	0.37

Table A.1 – continued from previous page

Station	LAT °	LON °	t^* (s)	Station	LAT °	LON °	t^* (s)
ANTO	39.87	32.79	0.18	APEZ	34.98	24.89	-1.08
AQU	42.35	13.40	-0.30	ARA	41.85	74.33	-0.10
ARU	56.43	58.56	-0.59	ASBS	33.62	-116.47	0.51
ATD	11.53	42.85	0.23	ATKA	52.20	-174.20	-0.18
ATTU	52.88	173.16	-0.67	AZ45	36.46	-109.08	0.04
AZ46	36.55	-109.23	0.08	AZ47	36.64	-109.33	0.55
AZ48	36.76	-109.54	-0.03	AZ49	36.89	-109.69	0.11
AZ50	36.98	-109.86	0.20	BADG	58.03	-4.88	0.20
BAR	32.68	-116.67	0.33	BASO	-4.32	35.14	0.44
BB05	30.38	90.91	-0.68	BB08	30.13	90.55	-0.38
BB10	30.00	90.41	0.50	BB14	29.37	90.18	0.64
BB20	28.73	89.66	-1.16	BB23	28.49	89.66	-1.13
BB34	29.11	89.25	-1.10	BB36	29.82	90.76	-1.04
BBB	52.18	-128.11	0.14	BBLV	33.92	-81.53	-0.56
BC3	33.66	-115.45	0.27	BCHU	39.79	78.78	0.20
BEL	34.00	-116.00	0.01	BENH	57.61	-5.31	0.12
BESE	58.58	-134.85	0.05	BFO	48.33	8.33	0.44
BGCA	5.18	18.42	-0.60	BGIO	31.72	35.09	0.66
BILL	68.07	166.45	-0.10	BINY	42.20	-75.99	-0.24
BJI	40.04	116.18	0.22	BJT	40.02	116.17	0.37
BLA	37.21	-80.42	-0.19	BLACK	33.36	-81.26	-0.33
BLO	39.17	-86.52	-0.17	BLSY	32.91	-116.88	0.28
BMBC	56.04	-122.13	0.22	BMN	40.43	-117.22	0.20
BMR	60.97	-144.60	-0.41	BNGL	38.92	40.60	-0.08
BNI	45.05	6.68	0.28	BOBR	57.91	-4.33	0.30

Table A.1 – continued from previous page

Station	LAT °	LON °	t^* (s)	Station	LAT °	LON °	t^* (s)
BOHN	56.91	-4.80	0.12	BORG	64.75	-21.33	0.98
BOSA	-28.61	25.26	-0.61	BOXN	63.85	-109.72	-0.59
BOZ	45.65	-111.63	0.13	BPAW	64.10	-150.98	0.76
BRK	42.55	-114.96	0.14	BRNJ	40.68	-74.57	0.13
BRVK	53.06	70.28	-0.19	BTDF	1.36	103.77	0.28
BTLS	38.43	42.12	-0.51	BUMT	27.55	90.77	-2.50
BUNG	27.88	85.89	-0.47	BUZZ	36.02	-120.60	0.23
BVDA2	33.33	-116.37	0.14	BW06	42.77	-109.56	0.09
BYBT	40.24	40.27	-0.19	BYKN	38.17	41.78	-0.79
BYR	62.69	-150.23	-0.52	BZN	33.49	-116.67	0.33
CALB	34.14	-118.63	0.09	CALI	40.37	-108.57	0.50
CAMN	63.73	-110.90	-0.03	CAN	-35.32	149.00	0.24
CARR	57.47	-5.57	0.05	CART	37.59	-1.00	0.27
CASS	57.98	-4.61	0.04	CASY	-66.28	110.54	0.09
CBB	50.03	-125.37	0.54	CBKS	38.81	-99.74	-0.56
CBN	38.20	-77.37	1.36	CCM	38.06	-91.24	-0.33
CHAT	40.92	76.52	0.48	CHF	34.33	-118.03	0.27
CHK	53.68	70.62	-0.22	CHM	43.00	74.75	0.13
CHTO	18.81	98.94	-0.24	CIA	33.40	-118.42	0.18
CIC	42.95	-113.21	0.33	CII	41.72	14.31	0.35
CLUN	57.15	-5.21	0.30	CMB	38.03	-120.39	0.30
CMPC	7.65	-64.07	-0.21	COL	64.90	-147.79	0.11
COLA	64.87	-147.86	-0.06	CONY	42.67	-74.47	-0.03
COR	44.59	-123.30	0.30	COWN	65.27	-111.19	-0.98
CPNY	40.79	-73.96	0.44	CRAB	36.01	-120.55	0.04

Table A.1 – continued from previous page

Station	LAT °	LON °	t^* (s)	Station	LAT °	LON °	t^* (s)
CREG	56.94	-4.52	-0.09	CRY	33.57	-116.74	0.31
CRZF	-46.43	51.86	0.33	CSD	40.44	-108.28	0.21
CSS	34.96	33.33	-0.13	CTA	-20.09	146.25	0.24
CWC	36.44	-118.08	0.48	DAC	36.28	-117.59	0.38
DAG	76.77	-18.66	0.30	DALL	56.83	-4.22	0.11
DAN	34.64	-115.38	0.23	DAV	7.07	125.58	0.22
DAWY	64.07	-139.39	-0.15	DBIC	6.67	-4.86	-0.75
DBO	43.12	-123.24	1.24	DGE	40.99	74.47	0.71
DGR	33.65	-117.01	0.36	DGRL	41.06	43.33	0.65
DH1	63.37	-148.38	-0.18	DIHI	-79.85	159.48	0.66
DIV	61.13	-145.77	-0.36	DJJ	34.11	-118.46	0.13
DLBC	58.44	-130.03	0.12	DMRK	10.31	37.73	0.66
DOT	39.78	-106.99	-0.62	DOUG	40.57	-108.69	0.23
DPC	50.36	16.41	0.35	DRLN	49.26	-57.50	-0.42
DRV	-66.67	140.00	-0.21	DRY	40.70	-108.54	-0.98
DSB	53.25	-6.38	0.45	DUND	57.87	-5.26	0.15
DWDAN	34.74	-82.83	-1.18	DWPF	28.11	-81.43	-0.22
DYBR	37.82	40.32	0.73	DZM	-22.07	166.44	0.66
E008	-77.28	160.56	0.55	ECH	48.22	7.16	0.63
EDM	53.22	-113.35	-1.49	EFS	63.56	-149.78	-0.70
EIL	29.67	34.95	-0.12	EKS2	42.66	73.78	0.21
EKTN	64.70	-110.61	-0.36	ELK	40.74	-115.24	0.73
ENH	30.28	109.49	-0.10	ERGN	38.26	39.73	-0.18
ERM	42.01	143.16	0.61	ES01	31.26	92.09	-0.72
ES03	30.75	92.86	-0.48	ES04	30.65	93.25	-0.21

Table A.1 – continued from previous page

Station	LAT °	LON °	t^* (s)	Station	LAT °	LON °	t^* (s)
ES05	31.68	92.40	-0.34	ES07	31.48	93.70	-0.44
ES08	31.28	93.84	-0.41	ES09	31.91	93.06	-0.86
ES10	31.84	93.79	-0.51	ES11	31.91	94.14	-0.43
ES12	31.59	94.71	-0.22	ES13	31.54	95.28	-0.71
ES14	31.25	95.90	-0.54	ES15	31.19	96.50	-0.56
ES18	31.30	97.96	-0.08	ES20	30.73	96.10	-0.45
ES23	30.69	97.26	-0.38	ES25	30.12	97.30	-0.49
ES26	29.96	97.51	-0.58	ES27	29.64	97.90	0.07
ES28	29.72	98.43	-0.30	ES29	30.01	96.69	-0.11
ES30	29.32	97.19	-0.15	ES31	29.51	96.76	-0.11
ES33	29.77	95.70	-0.30	ES35	29.96	94.78	-0.75
ES36	29.81	93.91	-0.20	ES37	29.90	93.51	-0.22
ES39	29.87	92.62	-0.22	ES40	29.71	92.15	-0.42
ES41	29.19	91.76	-0.37	ES42	28.90	91.94	0.03
ES45	29.12	93.78	-0.54	ESK	55.32	-3.20	0.58
EUO	44.03	-123.07	0.14	EYAK	60.55	-145.75	-0.24
EYMN	47.95	-91.50	-0.27	EZRM	40.10	41.36	0.16
FA08	37.32	-89.53	-0.32	FA20	42.97	-95.98	-1.48
FA21	43.74	-96.62	-0.77	FA24	46.53	-101.24	-0.14
FA28	50.76	-111.52	-0.61	FALS	54.86	-163.42	-0.72
FCC	58.76	-94.09	-0.62	FDF	14.73	-61.14	-0.71
FFC	54.72	-101.98	-0.21	FITZ	-18.10	125.64	-0.35
FLV2	32.91	-117.06	0.43	FNBB	58.89	-123.01	0.15
FODE	35.38	24.96	-1.20	FOR	40.86	-73.89	0.33
FRB	63.75	-68.55	-0.48	FRD	33.49	-116.60	0.31

Table A.1 – continued from previous page

Station	LAT °	LON °	t^* (s)	Station	LAT °	LON °	t^* (s)
FURI	8.90	38.68	1.82	FWGP	40.96	-108.77	0.48
GAC	45.70	-75.48	-0.98	GAMB	63.78	-171.70	0.16
GAR	39.00	70.32	-0.56	GARY	57.08	-4.96	0.28
GENY	42.77	-77.82	-0.87	GGN	45.12	-66.82	-0.77
GLA	33.05	-114.83	0.27	GLAC	33.60	-116.48	0.32
GNI	40.15	44.74	0.03	GNR	63.83	-148.98	-0.46
GNW	47.56	-122.83	0.10	GOBA	7.03	39.98	-0.24
GOGA	33.41	-83.47	0.09	GOMA	-4.84	29.69	0.52
GOO	63.23	-149.27	-0.74	GPO	35.65	-117.66	0.25
GPSS1	42.50	-123.37	0.45	GRA1	49.69	11.22	0.05
GRC	47.30	3.07	-0.71	GRFO	49.69	11.22	0.02
GSC	35.30	-116.81	0.14	GUMO	13.59	144.87	-2.19
GVD	34.84	24.09	0.23	H1030	29.48	85.75	-0.03
H1090	29.92	85.73	-0.16	H1110	30.07	85.55	-0.13
H1120	30.14	85.41	-0.33	H1130	30.21	85.33	-0.33
H1150	30.36	85.31	-0.08	H1160	30.43	85.29	-0.05
H1200	30.72	85.14	-0.58	H1210	30.78	85.11	-0.69
H1230	30.93	85.10	-0.51	H1240	31.02	85.13	-0.48
H1250	31.08	85.00	-0.81	H1260	31.15	85.01	-0.50
H1270	31.23	85.07	-0.52	H1300	31.45	85.16	-0.54
H1310	31.52	85.18	-0.63	H1330	31.66	85.17	-0.71
H1340	31.73	85.14	-0.68	H1350	31.80	85.03	-0.56
H1360	31.86	84.95	-0.23	H1370	31.95	84.89	-0.10
H1400	32.12	84.69	-0.23	H1410	32.24	84.37	-0.70
H1415	32.31	84.22	-0.46	H1421	32.01	83.87	-0.70

Table A.1 – continued from previous page

Station	LAT °	LON °	t^* (s)	Station	LAT °	LON °	t^* (s)
H1422	32.06	83.90	-0.42	H1440	32.45	84.24	-0.26
H1460	32.60	84.22	-0.59	H1490	32.82	84.27	-0.29
H1500	32.89	84.29	-0.19	H1520	33.03	84.31	-0.58
H1530	33.12	84.22	-0.57	H1540	33.19	84.23	-0.19
H1550	33.26	84.25	-0.01	H1560	33.31	84.25	-0.33
H1580	33.53	84.29	-0.10	H1610	33.86	84.26	-0.01
H1620	33.97	84.22	0.04	HARA	40.17	76.84	0.85
HAWA	46.39	-119.53	0.20	HDC	10.00	-84.11	0.06
HGN	50.76	5.93	0.45	HIA	49.27	119.74	0.28
HIAW	41.01	-108.73	0.48	HILE	27.05	87.32	-1.14
HINS	39.35	41.70	0.37	HKT	29.96	-95.84	0.77
HLID	43.56	-114.41	0.53	HLQI	40.84	77.96	1.01
HNB	49.27	-122.58	0.14	HNR	-9.44	159.95	0.32
HOOD	45.32	-121.65	-0.16	HOPB	49.39	-121.42	-0.41
HRPT	38.70	39.25	0.34	HRSN	39.95	42.29	0.65
HRV	42.51	-71.56	0.34	HURN	63.00	-149.61	0.01
HWB	33.03	-116.96	0.55	HWUT	41.61	-111.57	-0.02
HYB	17.42	78.55	0.30	IBBN	52.31	7.76	-0.15
ICAN	37.50	-121.33	-0.12	IDI	35.29	24.89	-0.60
IL31	64.77	-146.89	0.44	ILIC	39.45	38.57	-0.05
IMRL	39.88	38.12	0.44	INCN	37.48	126.62	0.30
INK	68.31	-133.52	-0.05	INU	35.35	137.03	-0.20
INZA	-5.12	30.40	0.80	ISA	35.66	-118.47	0.15
ISCO	39.80	-105.61	0.23	ISDE	-80.00	-134.99	-3.03
ISP	37.84	30.51	0.41	JCS	33.09	-116.60	0.37

Table A.1 – continued from previous page

Station	LAT °	LON °	t^* (s)	Station	LAT °	LON °	t^* (s)
JCT	30.48	-99.80	0.08	JER	31.77	35.20	-0.01
JFWS	42.91	-90.25	-0.35	JNMT	40.46	-108.02	0.09
JTS	10.29	-84.95	0.72	JWM	40.57	-108.60	0.20
KAI	41.57	75.01	0.61	KAPI	-5.01	119.75	0.24
KAPO	49.45	-82.51	0.31	KAR	42.47	78.40	0.08
KARL	41.47	77.31	0.36	KARS	40.62	43.07	0.40
KASH	39.52	75.92	1.42	KAZ	41.38	73.94	2.45
KBK	42.66	74.95	-0.51	KBS	78.93	11.94	0.41
KDAK	57.78	-152.58	-0.23	KDJ	42.13	77.19	0.44
KEG	29.93	31.83	-0.66	KENS	42.32	79.24	0.91
KEV	69.76	27.00	0.08	KGNO	44.23	-76.49	-0.66
KHA	44.21	74.00	1.81	KIBE	-5.38	37.48	0.58
KIEV	50.70	29.22	-0.41	KINN	41.18	-108.59	-0.76
KIP	21.42	-158.01	0.02	KIV	43.96	42.69	-0.73
KKAR	43.11	70.51	0.10	KMBO	-1.13	37.25	0.57
KMI	25.12	102.74	-0.19	KMNB	24.46	118.39	0.81
KNB	37.02	-112.82	0.20	KNW	33.71	-116.71	0.39
KOG	5.21	-52.73	-0.70	KOND	-4.90	35.80	0.67
KONO	59.65	9.60	0.34	KOPG	40.50	79.04	-0.01
KOTK	40.22	43.01	-0.54	KRIS	35.18	25.50	-0.79
KRLV	39.37	40.99	0.93	KSA	41.54	77.93	0.17
KSDI	33.19	35.66	0.44	KSM	1.47	110.31	1.01
KSU1	39.10	-96.61	-0.30	KTH	63.55	-150.92	-0.32
KTLN	37.95	41.71	0.07	KUR	50.71	78.62	-0.03
KWP	49.63	22.71	-0.81	KYPR	37.56	41.17	-0.35

Table A.1 – continued from previous page

Station	LAT °	LON °	t^* (s)	Station	LAT °	LON °	t^* (s)
KZA	42.08	75.25	-0.09	LANG	40.87	-108.29	0.35
LBNH	44.24	-71.93	0.41	LBTB	-25.02	25.60	-0.25
LDS	37.24	-113.35	0.27	LEEP	35.99	-120.51	0.08
LGSN	64.33	-110.13	-0.11	LGU	34.11	-119.07	0.21
LIME	40.87	-108.79	-0.25	LKWY	44.57	-110.40	-0.11
LLLB	50.61	-121.88	-0.10	LMN	39.42	-103.62	-1.06
LMQ	47.55	-70.33	0.44	LON	46.75	-121.81	0.43
LONG	-2.73	36.70	0.48	LOOK	40.86	-108.48	-0.45
LRAL	33.03	-87.00	0.53	LSA	29.70	91.15	-0.26
LSC	40.53	-108.44	0.89	LSZ	-15.28	28.19	-0.02
LTX	29.33	-103.67	0.33	LTY	47.26	-120.67	0.44
LVA2	33.35	-116.56	0.37	LVZ	67.90	34.65	0.01
LZH	36.09	103.84	-0.29	MA2	59.58	150.77	0.22
MAGL	-76.14	162.41	0.13	MAHO	39.90	4.27	0.14
MAJO	36.55	138.20	0.08	MAK	46.81	81.98	0.02
MALT	38.31	38.43	0.21	MATB	26.15	119.95	0.27
MAUI	20.77	-156.24	-0.39	MAW	-67.60	62.87	0.06
MAYB	40.48	-108.19	-0.50	MB01	33.34	-106.03	0.27
MB05	34.66	-108.01	0.10	MBC	76.24	-119.36	-0.21
MBWE	-4.96	34.35	1.70	MC01	31.00	102.35	-0.12
MC02	30.38	103.43	-0.84	MC03	30.00	102.49	-0.66
MC04	30.06	101.48	0.01	MC05	29.99	100.22	-0.10
MC06	28.94	99.79	0.06	MC07	29.05	100.42	0.31
MC08	29.00	101.51	-0.39	MC09	28.96	102.76	-0.65
MC10	28.98	103.87	-0.50	MC13	27.74	100.76	-0.06

Table A.1 – continued from previous page

Station	LAT °	LON °	t^* (s)	Station	LAT °	LON °	t^* (s)
MC14	27.86	99.74	0.13	MCK	63.73	-148.93	-0.48
MCWV	39.66	-79.85	0.36	MDJ	44.62	129.59	0.34
MGTN	63.69	-109.59	-0.24	MHR	62.86	-149.86	-0.30
MHV	54.96	37.77	-0.90	MIAR	34.55	-93.58	-0.06
MIDW	28.22	-177.37	0.49	MILN	56.28	-3.45	0.43
MKAR	46.79	82.29	-0.34	MLAC	37.63	-118.83	-0.09
MLON	63.97	-109.90	0.13	MLR	45.49	25.95	-0.30
MNT	45.50	-73.62	-1.58	MNV	38.43	-118.15	0.45
MOBC	53.20	-131.90	0.07	MOH9	35.97	-120.57	-0.04
MONP	32.89	-116.42	0.39	MORC	6.59	-66.84	0.40
MPH	35.12	-89.93	-1.01	MPM	36.06	-117.49	0.19
MRDN	37.29	40.70	0.27	MRED	35.96	-120.48	0.12
MRNI	33.12	35.39	-1.77	MSDY	40.46	37.78	0.41
MSO	46.83	-113.94	0.12	MTAN	-7.91	33.32	0.39
MTE	40.40	-7.54	-0.90	MTOR	-5.25	35.40	0.89
MUSH	38.76	41.48	1.37	MVL	40.00	-76.35	0.34
MVU	38.50	-112.21	0.05	MWC	34.22	-118.06	0.11
MYNC	35.07	-84.13	0.16	N00	42.46	-107.70	-0.48
N01	42.28	-107.60	-0.23	N04	41.98	-107.43	-0.07
N06	41.80	-107.35	-0.04	N08	41.62	-107.28	0.15
N09	41.54	-107.24	0.09	N10	41.45	-107.21	-0.10
N15A	41.00	-107.03	0.48	N16	40.92	-106.99	0.34
N20	40.57	-106.88	0.30	N21	40.45	-106.92	0.27
N25	40.13	-106.70	0.29	NACB	24.17	121.59	0.10
NATX	31.76	-94.66	0.07	NCB	43.97	-74.22	-0.01

Table A.1 – continued from previous page

Station	LAT °	LON °	t^* (s)	Station	LAT °	LON °	t^* (s)
NE71	31.69	-115.91	0.37	NE72	30.85	-116.06	0.39
NE73	30.07	-115.35	0.66	NE75	27.29	-112.86	-0.05
NE76	26.89	-112.00	0.11	NE77	26.02	-111.36	-0.02
NE78	24.40	-111.11	0.20	NE79	23.12	-109.76	0.23
NE80	30.50	-112.32	0.14	NE81	28.92	-109.64	0.14
NE82	26.92	-109.23	0.14	NE83	24.73	-107.74	-0.41
NEE	34.82	-114.60	-0.02	NEW	48.26	-117.12	0.15
NHSC	33.11	-80.18	-0.12	NIL	33.65	73.27	-0.23
NM07	32.08	-103.84	-0.52	NM09	32.33	-104.12	0.35
NM11	32.58	-104.41	0.48	NM12	32.68	-104.51	0.59
NM14	32.91	-104.76	0.35	NM15	33.01	-104.91	0.37
NM17	33.26	-105.17	0.01	NM18	33.40	-105.34	0.04
NM19	33.49	-105.46	-0.13	NM20	33.60	-105.59	-0.10
NM21	33.73	-105.74	-0.40	NM22	33.84	-105.87	-0.05
NM23	33.95	-106.01	0.30	NM24	34.05	-106.12	0.10
NM25	34.17	-106.26	-0.16	NM26	34.26	-106.36	-0.25
NM27	34.39	-106.52	-0.03	NM29	34.65	-106.85	1.00
NM30	34.74	-106.97	1.32	NM31	34.85	-107.10	0.06
NM32	34.98	-107.26	-0.12	NM33	35.11	-107.42	0.31
NM34	35.27	-107.64	0.47	NM35	35.34	-107.71	0.21
NM36	35.45	-107.82	0.10	NM37	35.58	-108.00	0.46
NM38	35.70	-108.16	0.30	NM39	35.79	-108.27	0.34
NM40	35.95	-108.43	0.12	NM41	36.04	-108.57	0.00
NM43	36.25	-108.89	-0.18	NM44	36.42	-108.96	0.10
NNA	-11.99	-76.84	-0.84	NOUC	-22.10	166.30	0.48

Table A.1 – continued from previous page

Station	LAT °	LON °	t^* (s)	Station	LAT °	LON °	t^* (s)
NRIL	69.50	88.44	-0.02	NRN	41.42	75.98	0.60
NSS	64.53	11.97	0.07	NST	42.91	-113.98	0.45
NV32	38.33	-118.30	0.73	NV33	38.49	-118.42	0.56
NVS	54.84	83.23	0.02	NWAO	-32.93	117.24	-0.83
OBN	55.11	36.57	-0.84	OCWA	47.75	-124.18	0.12
OSI	34.61	-118.72	0.17	OT03	44.41	-122.47	0.03
OT11	42.19	-118.34	0.04	OXF	34.51	-89.41	-0.98
OZB	48.96	-125.49	0.28	PAB	39.54	-4.35	-0.20
PAF	-49.35	70.21	1.05	PAL	41.01	-73.91	0.09
PALK	7.27	80.70	1.11	PARO	27.57	89.32	-1.38
PAS	34.15	-118.17	0.20	PD31	42.77	-109.56	0.17
PDG	43.33	79.48	-0.21	PEL	-33.15	-70.68	-2.45
PET	53.02	158.65	0.16	PFO	33.61	-116.46	0.42
PGC	48.65	-123.45	0.77	PHAP	27.51	86.58	-2.69
PHC	50.71	-127.43	0.30	PHID	27.15	87.76	-2.21
PHL	35.41	-120.55	0.27	PIN	43.81	-120.87	-0.45
PINR	40.36	-108.37	0.45	PIQG	40.32	77.63	0.94
PKD	35.95	-120.54	-0.21	PLAL	34.98	-88.08	-0.10
PLCA	-40.73	-70.55	0.03	PLM	33.35	-116.86	0.21
PMB	50.52	-123.08	-0.05	PMG	-9.41	147.15	0.21
PMR	41.08	-108.82	-0.32	PMSA	-64.77	-64.05	0.34
PNL	59.67	-139.40	0.19	PNT	49.32	-119.62	-0.23
POGR	44.01	10.82	0.80	POHA	19.76	-155.53	-0.37
POLY	58.00	-5.11	0.15	POW	40.94	-108.42	-0.12
PPLA	62.90	-152.19	-0.25	PSI	2.69	98.92	-0.14

Table A.1 – continued from previous page

Station	LAT °	LON °	t^* (s)	Station	LAT °	LON °	t^* (s)
PSZ	47.92	19.89	0.19	PUGE	-4.71	33.18	0.73
PUL	59.77	30.32	-1.61	PUPE	31.34	-113.63	0.15
PVMO	36.41	-89.70	-0.63	PVW	62.53	-150.80	-0.14
QIZ	19.03	109.84	0.68	RAIO	46.04	-122.89	0.36
RANN	56.71	-4.11	0.32	RAYN	23.52	45.50	-0.05
RC01	61.09	-149.74	-0.72	RCK	64.04	-149.17	-0.54
RDM	33.63	-116.85	0.29	RES	74.69	-94.90	0.16
RGN	54.55	13.32	-0.26	RIYD	24.72	46.64	-0.15
RND	63.41	-148.86	-0.15	ROGR	58.03	-4.17	0.45
RPN	-27.13	-109.33	-1.27	RPV	33.74	-118.40	-0.04
RRE	41.17	-108.73	-0.56	RRW	41.14	-108.86	-0.18
RSSD	44.12	-104.04	0.10	RUBB	54.33	-130.25	1.38
RUE	52.48	13.78	-0.05	RUMJ	27.30	86.55	-1.98
RUNG	-6.94	33.52	0.34	S05B	36.85	-105.41	-0.08
S08	36.61	-105.32	0.34	S13	36.15	-105.26	0.21
S14	36.07	-105.23	0.21	SADO	44.77	-79.14	-0.22
SAGA	29.33	85.23	-0.84	SAN	63.72	-149.48	-1.00
SANT	36.37	25.46	0.38	SAW	61.81	-148.33	-0.90
SBA	-77.85	166.76	0.91	SBC	34.44	-119.71	-0.02
SCHQ	54.83	-66.83	-0.37	SCZ	36.60	-121.40	0.31
SDCO	37.75	-105.50	0.83	SDD	33.55	-117.66	-0.20
SDMD	39.41	-76.84	0.90	SDV	8.88	-70.63	-0.43
SEY	62.93	152.37	0.20	SFJ	67.00	-50.62	-0.45
SFUC	36.64	-6.18	0.66	SHB	49.60	-123.88	0.45
SHUM	33.63	-116.44	0.34	SILN	38.14	41.04	0.46

Table A.1 – continued from previous page

Station	LAT °	LON °	t^* (s)	Station	LAT °	LON °	t^* (s)
SIND	27.21	85.91	-1.75	SING	-4.64	34.73	0.49
SIRN	40.20	39.12	-0.32	SIUC	37.71	-89.22	-0.65
SJG	18.11	-66.15	-0.52	SKD	35.41	23.93	-0.67
SLA	35.89	-117.28	0.11	SLEB	51.17	-118.13	1.16
SLM	38.64	-90.24	-0.25	SLT	63.94	-149.12	-0.57
SMER	33.46	-117.17	0.64	SMR	40.72	-108.30	-0.43
SMTC	32.94	-115.80	0.26	SNAA	-71.67	-2.84	-0.54
SNB	48.78	-123.17	0.47	SNCC	33.25	-119.52	0.21
SND	33.55	-116.61	0.26	SNPN	63.52	-110.91	0.18
SNZO	-41.31	174.70	-0.20	SODA	18.29	42.38	0.34
SOL	32.84	-117.25	-0.20	SSB	45.28	4.54	0.91
SSE	31.10	121.19	0.43	SSLB	23.79	120.95	-0.04
SSPA	40.64	-77.89	0.13	ST09	31.42	90.00	1.26
STOR	58.24	-5.38	0.14	STU	48.77	9.19	0.32
SUKT	27.71	85.76	-2.51	SUR	-32.38	20.81	0.05
SUTT	40.58	-108.29	-0.63	SUW	54.01	23.18	-0.81
SVD	34.10	-117.10	0.17	SWB	40.65	-108.38	-0.35
SWD	60.10	-149.45	-0.17	SYO	-69.01	39.58	-0.75
TAM	22.79	5.53	-0.17	TANK	40.41	-108.74	-1.27
TARA	-3.89	36.02	0.51	TATO	24.97	121.50	0.08
TAU	-42.91	147.32	0.70	TDCB	24.25	121.16	0.21
TGMT	40.00	76.14	0.96	THAK	27.60	85.56	-1.55
THY	63.42	-145.75	-0.75	TIN	37.05	-118.23	-0.20
TIXI	71.63	128.87	0.06	TKM2	42.92	75.60	0.08
TLG	43.23	77.22	-0.01	TLKY	62.15	-150.06	-0.53

Table A.1 – continued from previous page

Station	LAT °	LON °	t^* (s)	Station	LAT °	LON °	t^* (s)
TLY	51.68	103.64	0.31	TNA	65.56	-167.92	-0.06
TNV	-74.70	164.12	0.67	TOV	34.16	-118.82	-0.04
TPH	38.08	-117.22	0.24	TPNV	36.95	-116.25	0.15
TPUB	23.30	120.63	-0.88	TRF	63.45	-150.29	1.43
TRO	33.52	-116.43	0.07	TRTE	58.38	26.72	-0.84
TSK	36.21	140.11	-0.05	TSUM	-19.20	17.58	-0.20
TTW	47.69	-121.69	-0.28	TUC	32.31	-110.78	0.42
TUE	46.47	9.35	-0.09	TUML	27.32	87.19	-1.90
TUND	-9.30	32.77	0.85	TUNL	36.20	94.82	-0.16
TWGB	22.82	121.08	1.49	TWIN	40.76	-108.38	-1.02
TWKB	21.94	120.81	-2.58	TX01	31.42	-103.11	-0.49
TX02	31.51	-103.20	-0.48	TX03	31.62	-103.32	0.08
TX06	31.97	-103.71	-0.50	UALR	34.78	-92.34	-0.27
UCH	42.23	74.51	0.12	UGM	-7.91	110.52	-2.48
ULHL	42.25	76.24	0.46	ULM	50.25	-95.87	-0.61
ULN	47.87	107.05	0.14	UNM	19.33	-99.18	0.26
UNV	53.85	-166.50	-0.54	URAM	-5.09	32.08	0.48
USC	34.02	-118.29	0.49	USIN	37.97	-87.67	-1.35
USP	43.27	74.50	0.24	UT51	37.07	-110.00	0.44
UT52	37.23	-110.13	0.32	UT53	37.35	-110.33	0.11
UTMT	36.34	-88.87	-0.26	UZML	39.71	39.72	-0.01
VCS	34.48	-118.12	0.19	VINE	35.95	-120.54	-0.07
VLC	44.16	10.39	0.15	VLDQ	48.19	-77.76	-0.44
VMSC	40.93	-108.65	0.57	VNDA	-77.52	161.85	0.51
VOS	52.72	70.98	-0.22	VSL	39.50	9.38	0.48

Table A.1 – continued from previous page

Station	LAT °	LON °	t^* (s)	Station	LAT °	LON °	t^* (s)
VSU	58.46	26.73	-0.46	VTS	42.62	23.24	0.49
VTV	34.57	-117.33	0.22	WAL	45.55	-117.47	-0.38
WALA	49.06	-113.91	0.75	WCI	38.23	-86.29	-0.09
WDC	40.58	-122.54	0.54	WDD	35.84	14.52	-0.30
WHY	60.66	-134.88	0.21	WLF	49.66	6.15	0.50
WMC	33.57	-116.67	0.17	WMOK	34.74	-98.78	0.23
WMQ	43.82	87.69	-0.27	WNDO	33.45	91.90	-0.18
WOAK	34.62	-83.05	-1.50	WON	63.46	-150.85	-0.35
WQIA	39.73	75.25	0.86	WRAB	-19.93	134.36	-0.20
WUAZ	35.52	-111.37	0.17	WUS	41.20	79.22	-0.13
WVOR	42.43	-118.64	0.17	WVT	36.13	-87.83	-0.20
XAN	34.03	108.92	-0.19	XIKR	39.82	77.37	0.60
XMAS	2.04	-157.45	0.25	Y03	43.81	-112.31	0.41
Y04	43.51	-111.90	0.25	Y05	43.19	-111.58	-1.90
Y07	42.56	-110.89	0.19	Y103	44.58	-110.81	0.17
Y105	44.97	-110.71	-0.73	Y12C	33.75	-114.52	0.13
Y13	45.27	-112.82	0.23	Y14	44.99	-112.46	-0.84
Y16	44.40	-111.60	0.05	Y17	44.10	-111.19	-0.07
Y18	43.75	-111.03	0.16	Y19	43.62	-110.60	0.61
Y20	43.17	-110.00	-0.25	Y24	45.98	-112.62	-0.89
Y25	45.71	-112.18	-0.19	Y32	43.58	-109.45	0.21
Y37	46.18	-112.03	0.32	Y40	45.35	-110.75	-0.18
Y44	44.10	-109.19	0.11	Y47	45.99	-110.04	-0.77
Y64	44.11	-107.47	0.17	YAK	62.03	129.68	-0.72
YAN	63.66	-148.77	-0.31	YAQ	33.17	-116.35	0.31

Table A.1 – continued from previous page

Station	LAT °	LON °	t^* (s)	Station	LAT °	LON °	t^* (s)
YKW1	62.48	-114.48	-0.31	YKW2	62.43	-114.60	-0.39
YKW3	62.56	-114.61	0.01	YKW4	62.49	-114.74	-0.30
YSCF	40.43	-108.43	-0.54	YSNY	42.48	-78.54	-1.41
YSS	46.96	142.76	0.11	YULB	23.39	121.30	1.50
ZENO	40.60	-108.82	-0.17	ZRN	52.95	69.00	-0.43

APPENDIX B

Effect of epicentral distance variations on spatial variations in t^*

It is estimated that t_P^* and t_S^* increase by about 0.2 s and 0.7 s, respectively, between epicentral distances of 30° and 97° (Chapter IV). While Δt^* for P- and S-waves are measured to estimate global variation in t_S^* (Chapter III), the effect of epicentral variations in t_P^* and t_S^* on spatial variations in t_S^* are investigated. When Δt^* measurements are corrected for the epicentral variations in t^*, t_S^* contrasts between regional maxima and minima become more prominent (Figure B.1). For example, t_S^* contrast between western and eastern North America increases from about 0.5 s to about 0.7 s, on average, after correction for the epicentral distance effect. Also, relatively larger t_S^* values in eastern Australia compare to western Australia become noticeable when Δt^* measurements are corrected for epicentral distance. Furthermore, t_S^* values close to ocean become generally larger while t_S^* values in continental shields become generally smaller.

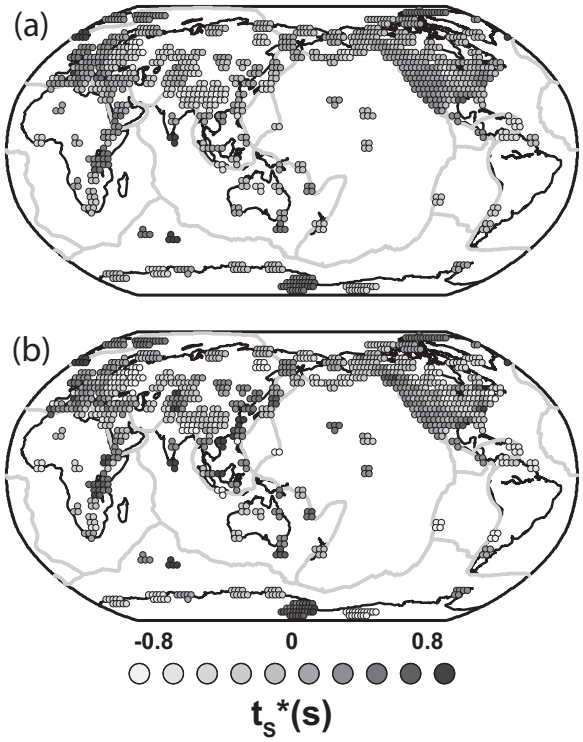

Figure B.1: Spatial variation of t_S^* in the upper mantle (a) before and (b) after correction for epicentral variation in t^*.

APPENDIX C

Effect of core-mantle reflections on Q_μ profile

For epicentral distances larger than 85°, corresponding to turning depths larger than 2470 km, P- and S-waves may interfere with CMB reflection phases (PcP and ScS) (Figure C.1) and render the measurements of spectral ratios inaccurate (Chapter IV). Therefore, it is important to investigate the significance of biases in Q_μ produced by extending data from the epicentral distance beyond 85°. Figure C.2 shows global mantle Q_μ profiles constrained using data at epicentral distances smaller than 98° (solid line), 90° (dashed line), and 85° (double-dot chain). This result shows that including data beyond 85° can render lowermost mantle Q_μ to be biased higher probably because the CMB reflections can increase the high frequency content in the signals and thus decrease the apparent attenuation while increasing Q_μ values. However, Q_μ values are perturbed little at depth shallower than about 2500 km.

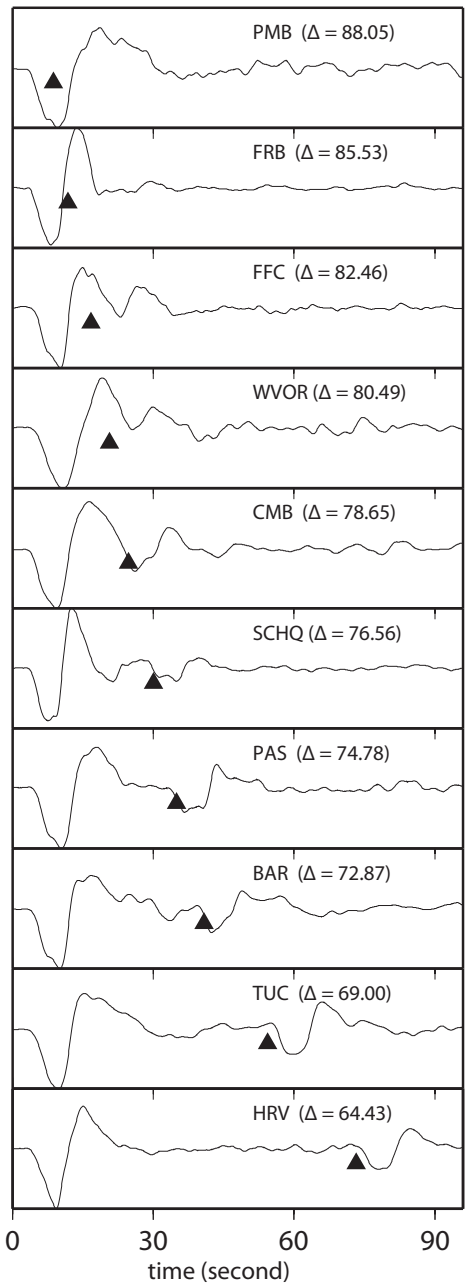

Figure C.1: Example S-wave arrivals recorded in ten teleseismic stations for the earthquake that broke on January 23rd, 1997 near the border between Bolivia and Argentina. Waveforms are presented top to bottom in accordance to increasing epicentral distance (Δ). S-wave arrivals are aligned near zero second and triangles represent theoretical arrival times for ScS phases.

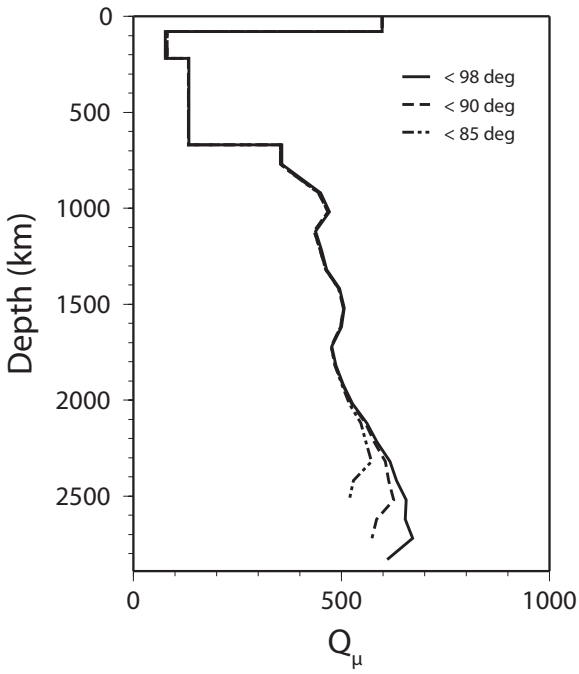

Figure C.2: Global mantle Q_μ profiles constrained using data at epicentral distances smaller than 98° (solid line), 90° (dashed line), and 85° (double-dot chain).

APPENDIX D

Effect of changes in mantle Q on simulated waveforms

While the full 3D shear-waveforms are simulated in Chapter 5.4, wave attenuation is ignored to avoid wave amplitude loss, especially at short periods. In Figure D.1, we compare the seismograms for the P0s plume velocity structure (Figure 5.3) with synthetics for two attenuation structures for the mantle. In Figure D.1b, we assume that the quality factor Q is 1000 throughout the mantle. In Figure D.1c, the quality factor Q has the same depth-dependence as in PREM. The waveforms have periods longer than 20 s. Note the similarity of the waveforms which indicates that attenuation is not responsible for the delay time variation.

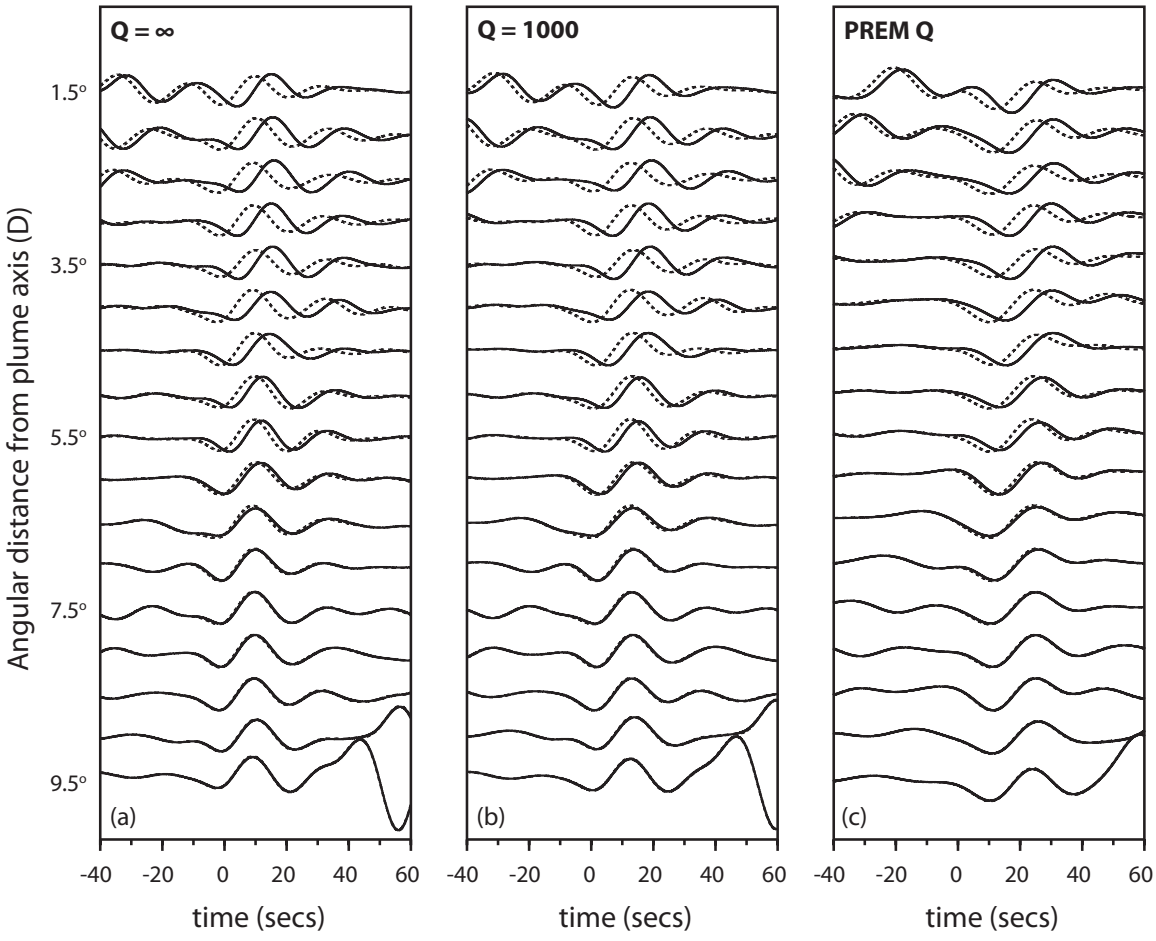

Figure D.1: Waveforms simulated by SHaxi method for periods longer than 20 s of SSS_M (aligned at time 0) between distances $D = 1.5°$ and $9.5°$ for models PREM (dashed line) and model P0s (solid line). (a) Simulated waveforms when attenuation is ignored ($Q = \infty$). (b) Waveforms when $Q = 1000$ is assumed. (c) Waveforms when the mantle Q structure of PREM is assumed.

BIBLIOGRAPHY

BIBLIOGRAPHY

Anderson, D. L. (1967), The anelasticity of the mantle, *Geophys. J. R. Astr. Soc.*, *14*, 135–164.

Anderson, D. L. (1989), *Theory of the Earth*, 366pp pp., Blackwell Scientific, Boston, Oxford.

Anderson, D. L., and J. W. Given (1982), Absorption band Q model for the Earth, *J. Geophys. Res.*, *87*, 3,893–3,904.

Artemieva, I. M., W. D. Mooney, and N. H. Sleep (2000), Plate motions and the destruction of lithospheric keels, *Eos Trans. AGU*, *81*, 1177.

Artemieva, I. M., M. Billien, J.-J. Lévêque, and W. D. Mooney (2004), Shear wave velocity, seismic attenuation, and thermal structure of the continental upper mantle, *Geophys. J. Int.*, *157*, 607–628.

Baqer, S., and B. J. Mitchell (1998), Regional variation of *Lg* coda *Q* in the continental United States and its relation to crustal structure and evolution, *Pure Appl. Geophys.*, *153*, 613–638.

Benz, H. M., A. D. Frankel, and D. M. Boore (1997), Regional *Lg* attenuation for the continental United States, *Bull. Seismol. Soc. Am.*, *87*, 606–619.

Bhattacharyya, J., G. Masters, and P. Shearer (1996), Global lateral variations of shear wave attenuation in the upper mantle, *J. Geophys. Res.*, *101*, 22,273–22,289.

Billien, M., J.-J. Lévêque, and J. Trampert (2000), Global maps of Rayleigh wave attenuation for periods between 40 and 150 seconds, *Geophys. Res. Lett.*, *27*, 3,619–3,622.

Booth, D. C., P. D. Marshall, and J. B. Young (1974), Long and short period *P*-wave amplitudes from earthquakes in the range 0°-114°, *Geophys. J. R. Astron. Soc.*, *39*, 523–537.

Burchfiel, B. C., D. S. Cowan, and G. A. Davis (1992), Tectonic overview of the Cordilleran orogen in the western United States, in *The Cordilleran Orogen: Conterminous U.S.*, vol. G-3, edited by B. C. Burchfiel, P. W. Lipman, and M. L. Zoback, pp. 407–479, Geol. Sco. Am., Boulder, Colo.

Butler, R. (1984), Azimuth, energy, Q, and temperature; Variations on P wave amplitudes in the United States, *Rev. Geophys. Space Phys.*, *22*, 1–36.

Butler, R., and L. Ruff (1980), Teleseismic short-period amplitudes, source and receiver variations, *Bull. Seismol. Soc. Am.*, *70*, 831–850.

Cammarano, F., S. Goes, P. Vacher, and D. Giardini:2003 (2003), Inferring upper-mantle temperatures from seismic velocities, *Phys. Earth Planet. Inter.*, *138*, 197–222.

Carpenter, E. W., P. D. Marshall, and A. Douglas (1967), The amplitude-distance curve for short period teleseismic P-waves, *Geophys. J. R. Astron. Soc.*, *13*, 61–70.

Chavez, D. E., and K. F. Priestley (1986), Measurement of frequency dependent Lg attenuation in the Great Basin, *Geophys. Res. Lett.*, *13*, 551–554.

Cleary, J. (1967), Analysis of the amplitudes of short-period P waves recorded by long range seismic measurements stations in the distance range 30° to 102°, *J. Geophys. Res.*, *72*, 4,705–4,712.

Cobden, L., S. Goes, F. Cammarano, and J. A. D. Connolly (2008), Thermochemical interpretation of one-dimensional seismic reference models for the upper mantle: evidence for bias due to heterogeneity, *Geophys. J. Int.*, *175*, 627–648.

Cobden, L., S. Goes, M. Ravenna, E. Styles, F. Cammarano, K. Gallagher, and J. A. D. Connolly (2009), Thermochemical interpretation of 1-D seismic data for the lower mantle: The significance of nonadiabatic thermal gradients and compositional heterogeneity, *J. Geophys. Res.*, *114* (B11309), doi:10.1029/2008JB006,262.

Connolly, J. A. D. (2005), Computation of phase equilibria by linear programming: A tool for geodynamic modeling and its application to subduction zone decarbonation, *Earth Planet. Sci. Lett.*, *236*, 524–541.

Cormier, V. F. (1982), The effect of attenuation on seismic body waves, *Bull. Seismol. Soc. Am.*, *72*, S143–S173.

Dallmeyer, R. D., J. E. Wright, D. T. S. Jr., and A. W. Snoke (1986), Character of the Alleghanian Orogeny in the Southern Appalachians: Part II. Geochronological constraints on the tectonothermal evolution of the eastern Piedmont in South Carolina, *Geol. Soc. Am. Bull.*, *97*, 1,329–1,344.

Dalton, C. A., and G. Ekström (2006), Global models of surface wave attenuation, *J. Geophys. Res.*, *111*, doi:10.1029/2005JB003,997.

Dalton, C. A., and U. H. Faul (2010), The oceanic and cratonic upper mantle; clues from joint interpretation of global velocity and attenuation models, *Lithos*, *120*, 160–172.

Dalton, C. A., G. Ekström, and A. M. Dziewonski (2008), The global attenuation structure of the upper mantle, *J. Geophys. Res.*, *113*, doi:10.1029/2007JB005,429.

Dalton, C. A., G. Ekström, and A. M. Dziewonski (2009), Global seismological shear velocity and attenuation: A comparison with experimental observations, *Earth Planet. Sci. Lett.*, *284*, 65–75.

Deen, T. J., W. L. Griffin, G. Begg, S. Y. O'Reilly, L. M. Natapov, and J. Hronsky (2006), Thermal and compositional structure of the subcontinental lithospheric mantle: derivation from shear wave seismic tomography, *Geochem. Geophys. Geosyst.*, *7*(Q07003), doi:10.1029/2005GC001,120.

Der, Z. A., and T. W. McElfresh (1976), Short-period P-wave attenuation along various paths in North America as determined from P-wave spectra of the SALMON nuclear explosion, *Bull. Seismol. Soc. Am.*, *66*, 1,609–1,622.

Der, Z. A., and T. W. McElfresh (1977), The relationship between anelastic attenuation and regional amplitude anomalies of short-period P waves in North America, *Bull. Seismol. Soc. Am.*, *67*, 1,303–1,317.

Der, Z. A., T. W. McElfresh, and A. O'Donnell (1982), An investigation of the regional variations and frequency dependence of anelastic attenuation in the mantle under the United-States in the 0.5–4 Hz band, *Geophys. J. R. Astron. Soc.*, *69*, 67–99.

Dixon, J. E., T. H. Dixon, D. R. Bell, and R. Malservisi (2004), Lateral variation in upper mantle viscosity: role of water, *Earth Planet. Sci. Lett.*, *222*, 451–467.

Durek, J. J., and G. Ekström (1996), A radial model of anelasticity consistent with long-period surface wave attenuation, *Bull. Seismol. Soc. Am.*, *86*, 144–158.

Dziewonski, A. M., and D. L. Anderson (1981), Preliminary Reference Earth Model, *Phys. Earth Planet. Inter.*, *25*, 297–356.

Dziewonski, A. M., V. Lekic, and B. Romanowicz (2010), Mantle anchor structure: an argument for bottom up tectonics, *Earth Planet. Sci. Lett.*, *299*, 69–79.

Evernden, J. F., and D. M. Clark (1970), Study of teleseismic *P* II - amplitude data, *Phys. Earth Planet. Inter.*, *4*, 24–31.

Farley, K. A., and E. Neroda (1998), Noble gases in the Earth's mantle, *Annu. Rev. Earth Planet. Sci.*, *26*, 189–218.

Farnetani, C. G., and H. Samuel (2003), Lagrangian structures and stirring in the Earth's mantle, *Earth Planet. Sci. Lett.*, *206*, 335–348.

Farnetani, C. G., and H. Samuel (2005), Beyond the thermal plume paradigm, *Geophys. Res. Lett.*, *32*(L07311), doi:10.1029/2005GL022,360.

Faul, U. H., and I. Jackson (2005), The seismological signature of temperature and grain size variations in the upper mantle, *Earth Plant. Sci. Lett.*, *234*, 119–134.

Faul, U. H., J. D. F. Gerald, and I. Jackson (2004), Shear wave attenuation and dispersion in melt-bearing olivine polycrystals: 2. Microstructural interpretation and seismological implications, *J. Geophys. Res.*, *109*, doi:10.1029/2003JB002,407.

Foulger, G. R., J. H. Natland, and D. L. Anderson (2005), A source for Icelandic magmas in remelted Iapetus crust, *J. Volcanol. Geoth. Res.*, *141*(1-2), 23–44.

Godey, S., F. Deschamps, J. Trampert, and R. Snieder (2004), Thermal and compositional anomalies beneath the North American continent, *J. Geophys. Res.*, *109*(B01308), doi:10.1029/2002JB002,263.

Goes, S., and S. van der Lee (2002), Thermal structure of the North American uppermost mantle inferred from seismic tomography, *J. Geophys. Res.*, *107*, doi:10.1029/2000JB000,049.

Goes, S., R. Govers, and P. Vacher (2000), Shallow mantle temperatures under Europe from P and S wave tomography, *J. Geophys. Res.*, *105*, 11,153–11,169.

Goes, S., F. Cammarano, and U. Hansen (2004), Synthetic seismic signature of thermal mantle plumes, *Earth Planet. Sci. Lett.*, *218*, 403–419.

Goes, S., F. J. Simons, and K. Yoshizawa (2005), Seismic constraints on temperature of the Australian uppermost mantle, *Earth Planet. Sci. Lett.*, *236*, 227–237.

Grand, S. P., and D. V. Helmberger (1984), Upper mantle shear structure of North America, *Geophys. J. R. Astron. Soc.*, *76*, 399–438.

Gung, Y., and B. Romanowicz (2004), Q tomography of the upper mantle using three-component long-period waveforms, *Geophys. J. Int.*, *157*, 813–830.

Hammond, W. C., and E. D. Humphreys (2000a), Upper mantle seismic wave velocity: Effects of realistic partial melt geometries, *J. Geophys. Res.*, *105*, 10,975–10,986.

Hammond, W. C., and E. D. Humphreys (2000b), Upper mantle seismic wave attenuation: Effects of realistic partial melt distribution, *J. Geophys. Res.*, *105*, 10,987–10,999.

Hawkesworth, C. J., S. Kelley, S. Turner, A. L. Roex, and B. Storey (1999), Mantle processes during Gondwana break-up and dispersal, *J. African Earth Sci.*, *28*, 239–261.

Helmberger, D. V., L. Wen, and X. Ding (1998), Seismic evidence that the source of the Iceland hotspot lies at the core-mantle boundary, *Nature*, *396*, 251–255.

Houston, H., and J. E. Vidale (1994), The temporal distribution of seismic radiation during deep earthquake rupture, *Science*, *265*, 771–774.

Humphreys, E. D., and D. D. Coblentz (2007), North American dynamics and western U.S. tectonics, *Rev. Geophys.*, *45*(RG3001), doi:10.1029/2005RG000,181.

Hwang, H.-J., and B. J. Mitchell (1987), Shear velocities, Q_β, and the frequency dependence of Q_β in stable and tectonically active regions from surface wave observations, *Geophys. J. R. Astron. Soc.*, *90*, 575–613.

Hwang, Y. K., and J. Ritsema (2011), Radial Q_μ structure of the lower mantle from teleseismic body-wave spectra, *Earth Planet. Sci. Lett.*, *303*, 369–375.

Hwang, Y. K., J. Ritsema, and S. Goes (2009), Spatial variations of P wave attenuation in the mantle beneath North America, *J. Geophys. Res.*, *114*(B06312), doi:10.1029/2008JB006,091.

Ito, G., and P. E. van Keken (2007), Hotspots and melting anomalies, in *Treatise on Geophysics*, vol. 7, edited by D. Bercovici, pp. 371–436, Elsevier, Amsterdam.

Jackson, I., J. D. F. Gerald, U. H. Faul, and B. H. Tan (2002), Grain-size-sensitive seismic wave attenuation in polycrystalline olivine, *J. Geophys. Res.*, *107*, doi:10.1029/2001JB001,225.

Jahnke, G., M. S. Thorne, A. Cochard, and H. Igel (2008), Global SH-wave propagation using a parallel axisymmetric spherical finite-difference scheme: application to whole mantle scattering, *Geophys. J. Int.*, *173*, 815–826.

Ji, Y., and H.-C. Nataf (1998), Detection of mantle plumes in the lower mantle by diffraction tomography: Hawaii, *Earth Planet. Sci. Lett.*, *159*, 99–115.

Kanamori, H., and D. L. Anderson (1977), Importance of physical dispersion in surface wave and free oscillation problems: Review, *Rev. Geophys. Space Phys.*, *15*, 105–112.

Kanamori, H., E. Hauksson, and T. Heaton (1997), Real-time seismology and earthquake hazard mitigation, *Nature*, *390*, 461–464.

Karato, S.-I. (1993), Importance of anelasticity in the interpretation of seismic tomography, *Geophys. Res. Lett.*, *20*, 1,623–1,626.

Karato, S.-I., and H. Jung (1998), Water, partial melting and the origin of the seismic low velocity and high attenuation zone in the uper mantle, *Earth Planet. Sci Lett.*, *157*, 193–207.

Karato, S.-I., and H. A. Spetzler (1990), Defect microdynamics in minerals and solid state mechanisms of seismic wave attenuation and velocity dispersion in the mantle, *Rev. Geophys.*, *28*(4), 399–421.

Khan, A., J. A. D. Connolly, and S. R. Taylor (2008), Inversion of seismic and geodetic data for the major element chemistry and temperature of the Earth's mantle, *J. Geophys. Res.*, *113*(B09308), doi:10.1029/2007JB005,239.

King, S. D., and J. Ritsema (2000), African hot spot volcanism: Small-scale convection in the upper mantle beneath cratons, *Science*, *290*, 1,137–1,140.

King, S. D., C. Lee, P. E. van Keken, W. Leng, S. Zhong, E. Tan, N. Tosi, and M. C. Kameyama (2010), A community benchmark for 2-D Cartesian compressible convection in the Earth's mantle, *Geophys. J. Int.*, *180*, 73–87.

Lawrence, J. F., and M. E. Wysession (2006a), QLM9; A new radial quality factor (Q_μ) model for the lower mantle, *Earth Planet. Sci. Lett.*, *241*, 962–971.

Lawrence, J. F., and M. E. Wysession (2006b), Seismic evidence for subduction-transported water in the lower mantle, in *Earth's deep water cycle*, vol. 168, edited by S. D. Jacobsen and S. van der Lee, pp. 251–261, Geophys. Monogr. AGU.

Lawrence, J. F., P. M. Shearer, and G. Masters (2006), Mapping attenuation beneath North America using waveform cross-correlation and cluster analysis, *Geophys. Res. Lett.*, *33*(L07315), doi:10.1029/2006GL025,813.

Lay, T., and D. V. Helmberger (1981), Body wave amplitude patterns and upper mantle attenuation variations across North-America, *Geophys. J. R. Astron. Soc.*, *66*, 691–726.

Lay, T., and T. C. Wallace (1988), Multiple scs attenuation and travel-times beneath Western North- America, *Bull. Seismol. Soc. Am.*, *78*, 2,041–2,061.

Lee, C.-T. A. (2003), Compositional variation of density and seismic velocities in natural peridotites at STP conditions: implications for seismic imaging of compositional heterogeneities in the upper mantle, *J. Geophys. Res.*, *108*, doi:10.1029/2003JB002,413.

Lees, J. M., and J. Park (1995), Multiple-taper spectral analysis; A stand-alone C-subroutine, *Comp. Geosci.*, *21*, 199–236.

Lekić, V., J. Matas, M. Panning, and B. Romanowicz (2009), Measurement and implications of frequency dependence of attenuation, *Earth Planet. Sci. Lett.*, *282*, 285–293.

Leng, W., and S. Zhong (2010), Surface subsidence caused by mantle plumes and volcanic loading in large igneous provinces, *Earth Planet. Sci. Lett.*, *291*, 207–214.

Lin, S. C., and P. E. van Keken (2006), Dynamics of thermochemical plumes: 1. Plume formation and entrainment of a dense layer, *Geochem. Geophys. Geosyst.*, *7*(Q02006), doi:10.1029/2005GC001,071.

Marone, F., and B. Romanowicz (2007), Non-linear crustal corrections in high-resolution regional waveform seismic tomography, *Geophys. J. Int.*, *170*, 460–467.

Melbourne, T., and D. V. Helmberger (1998), Fine structure of the 410-km discontinuity, *J. Geophys. Res.*, *103*, 10,091–10,102.

Minster, J. B., and D. L. Anderson (1981), A model of dislocation-controlled rheology for the mantle, *Phil. Trans. R. Soc. Lond.*, *299*, 319–356.

Mitchell, B. J. (1975), Regional Rayleigh wave attenuation in North America, *J. Geophys. Res.*, *80*, 4,904–4,916.

Mitchell, B. J., and L. Cong (1998), *Lg* coda Q and its relation to the structure and evolution of continents: a global perspective, *Pure Appl. Geophys.*, *153*, 655–663.

Montelli, R., G. Nolet, F. Dahlen, G. Masters, E. R. Engdahl, and S.-H. Hung (2004), Finite-frequency tomography reveals a variety of plumes in the mantle, *Science*, *303*, 338–343.

Morgan, P., and W. D. Gosnold (1989), Heat flow and thermal regimes in the continental United States, *Mem. Geol. Soc. Am.*, *172*, 493–522.

Morgan, W. J. (1971), Convection plumes in the lower mantle, *Nature*, *230*, 42–43.

Nataf, H.-C., and J. VanDecar (1993), Seismological detection of a mantle plume?, *Nature*, *364*, 115–120.

Okal, E. A., and B.-G. Jo (1990), Q measurements for phase X overtones, *Pure Appl. Geophys.*, *132*, 331–362.

Oki, S., and P. M. Shearer (2008), Mantle Q structure from S-P differential attenuation measurements, *J. Geophys. Res.*, *113*, doi:10.1029/2007JB005,567.

Perrillat, J. P., A. Ricolleau, I. Daniel, G. Fiquet, M. Mezouar, N. Guignot, and H.Cardon (2006), Phase transformations of subducted basaltic crust in the upmost lower mantle, *Phys. Earth Planet. Inter.*, *157*(1-2), 139–149.

Perry, H. K. C., A. M. Forte, and D. W. S. Eaton (2003), Upper-mantle thermochemical structure below North America from seismic-geodynamic flow models, *Geophys. J. Int.*, *154*, 279–299.

Pollack, H. P., S. J. Hurter, and J. R. Johnson (1993), Heat flow from the Earth's interior: Analysis of the global data set, *Rev. Geophys.*, *31*, 267–280.

Priestley, K., and D. McKenzie (2006), The thermal structure of the lithosphere from shear wave velocities, *Earth Planet. Sci. Lett.*, *244*, 285–301.

Reid, F. J. L., J. H. Woodhouse, and H. J. van Heijst (2001), Upper mantle attenuation and velocity structure from measurements of differential S phases, *Geophys. J. Int.*, *145*, 615–630.

Resovsky, J., J. Trampert, and R. D. van der Hilst (2005), Error bars for the global seismic Q profile, *Earth Planet. Sci. Lett.*, *230*, 413–423.

Ribe, N., A. Davaille, and U. R. Christensen (2007), Fluid dynamics of mantle plumes, in *Mantle plumes*, edited by J. Ritter and U. R. Christensen, pp. 1–48, Springer, Berlin.

Richards, M. A., R. A. Duncan, and V. Courtillot (1989), Flood basalt and hotspot tracks: Plume heads and tails, *Science*, *246*, 103–107.

Ritsema, J., and R. M. Allen (2003), The elusive mantle plume, *Earth Planet. Sci. Lett.*, *207*, 1–12.

Ritsema, J., H. J. van Heijst, and J. H. Woodhouse (1999), Complex shear velocity structure imaged beneath Africa and Iceland, *Science*, *286*, 1,925–1,928.

Romanowicz, B. (1995), A global tomographic model of shear attenuation in the upper mantle, *J. Geophys. Res.*, *100*, 12,375–12,394.

Romanowicz, B. (2008), Using seismic waves to image Earth's internal structure, *Nature*, *451*, 266–268.

Romanowicz, B., and Y. Gung (2002), Superplumes from the core-mantle boundary to the lithosphere: Implications for heat flux, *Science*, *296*, 513–516.

Romanowicz, B., D. E. Byrne, and S. K. Singh (1993), The Berkeley digital seismic network: upgrade status, *Seismol. Res. Lett.*, *64*, 42.

Roth, E. G., D. A. Wiens, L. M. Dorman, J. Hildebrand, and S. C. Webb (1999), Seismic attenuation tomography of the Tonga-Fiji region using phase pair methods, *J. Geophys. Res.*, *104*, 4,795–4,809.

Roth, E. G., D. A. Wiens, and D. Zhao (2000), An empirical relationship between seismic attenuation and velocity anomalies in the upper mantle, *Geophys. Res. Lett.*, *27*, 601–604.

Roult, G., and E. Clévédé (2000), New refinements in attenuation measurements from free-oscillation and surface-wave observations, *Phys. Earth Planet. Inter.*, *121*, 1–37.

Sato, H., I. S. Sacks, and T. Murase (1989), The use of laboratory velocity data for estimating temperature and partial melt fraction in the low velocity zone: Comparison with heat flow and electrical conductivity studies, *J. Geophys. Res.*, *94*, 5,689–5,704.

Schutt, D. L., and C. E. Lesher (2006), Effects of melt depletion on the density and seismic velocity of garnet and spinel lherzolite, *J. Geophys. Res.*, *111*, doi:10.1029/2003JB002,950.

Secor Jr., D. T., A. W. Snoke, and R. D. Dallmeyer (1986), Character of the Alleghanian Orogeny in the Southern Appalachians: Part III. Regional tectonic relations, *Geol. Soc. Am. Bull.*, *97*, 1,345–1,353.

Selby, N. D., and J. H. Woodhouse (2002), The Q structure of the upper mantle: Constraints from Rayleigh wave amplitudes, *J. Geophys. Res.*, *107*, doi:10.1029/2001JB000,257.

Shapiro, N. M., and M. H. Ritzwoller (2004), Inferring surface heat flux distributions guided by a global seismic model: particular application to Antarctica, *Earth Planet. Sci. Lett.*, *223*, 213–224.

Sheehan, A. F., and S. C. Solomon (1992), Differential shear wave attenuation and its lateral variation in the north Atlantic region, *J. Geophys. Res.*, *97*, 15,339–15,350.

Shen, Y., S. C. Solomon, I. T. Bjarnason, and C. J. Wolfe (1998), Seismic evidence for a lower-mantle origin of the Iceland Plume, *Nature*, *395*, 62–65.

Shito, A., S. Karato, and J. Park (2004), Frequency dependence of Q in Earth's upper mantle inferred from continuous spectra of body waves, *Geophys. Res. Lett.*, *31*(L12603), doi:10.1029/2004GL019,582.

Shito, A., S.-I. Karato, K. N. Matsukage, and Y. Nishihara (2006), Towards mapping the three-dimensional distribution of water in the upper mantle from velocity and attenuation tomography, pp. 225–236, Geophysical Monograph American Geophysical Union.

Smith, M. L., and F. A. Dahlen (1981), The period and Q of the Chandler wobble, *Geophys. J. R. Astron. Soc.*, *64*, 223–281.

Sobolev, S. V., H. Zeyen, G. Stoll, F. Werling, R. Altherr, and K. Fuchs (1996), Upper mantle temperatures from teleseismic tomography of French Massif Central including effects of composition, mineral reactions, anharmonicity, anelasticity and partial melt, *Earth Planet. Sci. Lett.*, *139*, 147–163.

Solomon, S. C., and M. N. Toksöz (1970), Lateral variation of attenuation of P and S waves beneath the United States, *Bull. Seismol. Soc. Am.*, *60*, 819–838.

Stein, S., and M. E. Wysession (2003), *An introduction to seismology, earthquakes, and Earth structure*, 498 pp., Blackwell Publishing, Malden, Mass.

Steinberger, B., and R. J. O'Connell (1998), Advection of plumes in mantle flow: implications for hot spot motion, mantle viscosity and plume distribution, *Geophys. J. Int.*, *132*, 412–434.

Stixrude, L., and C. Lithgow-Bertelloni (2005), Thermodynamics of mantle minerals I. Physical properties, *Geophys. J. Int.*, *162*, 610–632.

Sun, S.-S. (1982), Chemical composition and origin of the Earth's primitive mantle, *Geochimica et Cosmochimica Acta*, *46*, 179–192.

Teng, T.-L. (1968), Attenuation of body waves and the Q structure of the mantle, *J. Geophys. Res.*, *73*, 2,195–2,208.

Trampert, J., H. Paulssen, A. van Wettum, J. Ritsema, R. Clayton, R. Castro, C. Rebollar, and A. Perez-Vertti (2003), New array monitors seismic activity near the Gulf of California in Mexico, *Eos Trans. AGU*, *84*, 29,32.

van der Lee, S. (2002), High-resolution estimates of lithospheric thickness from Missouri to Massachusetts, USA, *Earth Planet. Sci. Lett.*, *203*, 15–23.

van der Lee, S., and G. Nolet (1997), Upper mantle S velocity structure of North America, *J. Geophys. Res.*, *102*, 22,815–22,838.

van Keken, P. E. (1997), Evolution of starting mantle plumes: a comparison between numerical and laboratory models, *Earth Planet. Sci. Lett.*, *148*, 1–11.

van Keken, P. E. (2001), Cylindrical scaling for dynamical cooling models of the Earth, *Phys. Earth Planet. Inter.*, *124*, 119–130.

van Keken, P. E., and C. W. Gable (1995), The interaction of a plume with a rheological boundary: a comparison between two- and three-dimensional models, *J. Geophys. Res.*, *100*, 20,291–20,302.

Warren, L. M., and P. M. Shearer (2000), Investigating the frequency dependence of mantle Q by stacking P and PP spectra, *J. Geophys. Res.*, *105*, 25,391–25,402.

Warren, L. M., and P. M. Shearer (2002), Mapping lateral variations in upper mantle attenuation by stacking P and PP spectra, *J. Geophys. Res.*, *107*, doi:10.1029/2001JB001,195.

Wessel, P., and W. H. F. Smith (1995), New Version of the Generic Mapping Tools Released, *Eos Trans. AGU*, *76*, 329.

Widmer, R., G. Masters, and F. Gilbert (1991), Spherically symmetrical attenuation within the earth from normal mode data, *Geophys. J. Int.*, *104*, 541–553.

Wielandt, E. (1987), On the validity of the ray approximation for interpreting delay times, in *Seismic Tomography*, edited by G. Nolet, pp. 85–98, Reidel Publ. Co., Dordrecht.

Wolfe, C. J., I. T. Bjarnason, J. C. VanDecar, and S. C. Solomon (1997), Seismic structure of the Iceland mantle plume, *Nature*, *385*, 245–247.

Wolfe, C. J., S. C. Solomon, G. Laske, J. A. Collins, R. S. Detrick, J. A. Orcutt, D. Bercovici, and E. H. Hauri (2009), Mantle shear-wave velocity structure beneath the Hawaiian Hot Spot, *Science*, *326*, 1,388–1,390.

Yamazaki, D., and S.-I. Karato (2001), Some mineral physics constraints on the rheology and geothermal structure of Earth's lower mantle, *Am. Mineral.*, *86*, 385–391.

Yang, Y., D. W. Forsyth, and D. S. Weeraratne (2007), Seismic attenuation near the East Pacific Rise and the origin of the low-velocity zone, *Earth Planet. Sci. Lett.*, *258*, 260–268.